FAST AND EFFICIENT LOCOMOTION USING OSCILLATING FLEXIBLE PLATES

A Dissertation
Presented to
The Academic Faculty

by

Peter Derek Yeh

In Partial Fulfillment
of the Requirements for the Degree
Doctor of Philosophy in the
George W. Woodruff School of Mechanical Engineering

Georgia Institute of Technology
December 2016

FAST AND EFFICIENT LOCOMOTION USING OSCILLATING FLEXIBLE PLATES

Approved by:

Dr. Alexander Alexeev, Advisor
George W. Woodruff School of
Mechanical Engineering
Georgia Institute of Technology

Dr. Alper Erturk
George W. Woodruff School of
Mechanical Engineering
Georgia Institute of Technology

Dr. David Hu
George W. Woodruff School of
Mechanical Engineering
Georgia Institute of Technology

Dr. Michael Leamy
George W. Woodruff School of
Mechanical Engineering
Georgia Institute of Technology

Dr. Ramiro Godoy-Diana
Physique et Mécanique des Milieux
Hétérogènes
ESPCI

Date Approved: December 2016

To my better half, Angela, my parents Mimi and Stanley, and my sister Jessica.

Without all of your love, patience, and support, this work would not be possible.

ACKNOWLEDGEMENTS

First, I would like to express my sincere gratitude to my thesis advisor, Dr. Alexander Alexeev, for his continuous support of my Ph.D. research, and for his endless enthusiasm, patience, motivation, and expertise. In addition, I would like to thank Dr. Alexeev for fostering a collaborative research environment in which scientific ideas can be shared and discussed freely, and for continuously keeping the best interests of his students as a top priority.

I would also like to thank the rest of my thesis committee, Dr. Alper Erturk, Dr. David Hu, Dr. Michael Leamy, and Dr. Ramiro Godoy-Diana for their encouragement and insightful comments, as well as challenging me to widen my research perspective.

In addition, I would like to thank the Georgia Tech professors from whom I have had the privilege to learn in their classes. I am also grateful to Dr. Itzhak Green, who supervised my teaching practicum and provided valuable teaching advice.

I would like to thank my fellow labmates, Hassan, Wenbin, Zach, Matt, Nick, Yaro, Sam as well as my undergraduate research assistants, Ethan, Yuanda, Camila, and Michael for all of their help along the way, for creative scientific and nonscientific lab discussions, and for a great time the past 5 years.

I would also like to thank my fellow graduate students, Phil, Patrick, Matt, Richard, Tommy, Bernie, Jon, and Rob for all of their help, lunchtime discussions, and fun we have shared in graduate school together.

Finally, I would like to thank my family to whom this thesis is dedicated: my parents and my sister for their continuous love and support along the way. A special thank you goes to my wife Angela, for her unwavering sacrifice, love, and encouragement during my Ph.D. studies.

TABLE OF CONTENTS

DEDICATION . . . . . **iii**

ACKNOWLEDGEMENTS . . . . . **iv**

LIST OF TABLES . . . . . **viii**

LIST OF FIGURES . . . . . **ix**

SUMMARY . . . . . **xvi**

I INTRODUCTION **1**

1.1 Overview 1

1.2 Background and Literature Review 2

1.2.1 Designing Mechanical Fish-like Propulsive Systems 2

1.2.2 Previous Work on Physics of Fish-like Propulsion 5

1.2.3 Current Research Challenges 7

1.3 Research Objectives and Scope 9

II COMPUTATIONAL MODEL **11**

2.1 Fluid-Structure Interaction (FSI) Methodology 11

2.1.1 Lattice Boltzmann Method (LBM) 11

2.1.2 Lattice Spring Method (LSM) 14

2.1.3 Computational Domain 18

2.1.4 Boundary Conditions and FSI Coupling 19

2.2 Swimmer LSM Models 20

2.2.1 Uniform Rectangular Plate with LE Actuation 21

2.2.2 Trapezoidal Plate 22

2.2.3 Tapered Thickness 24

2.2.4 Plate with Internal Actuation 25

2.3 Model Validation 27

2.3.1 Lift and Drag on Plate Undergoing Insect-like Hovering Stroke 27

2.3.2 Tapered Plate Deflection 29

2.3.3 Internally Actuated Plate Deflection 30
2.3.4 Trapezoidal Plate Deflection 32
2.4 System Parameters 34
III FREE SWIMMING OF PLUNGING FLEXIBLE PLATE . 37
3.1 Introduction and Computational Setup 37
3.2 Results and Discussion 38
3.2.1 Performance Characterization 38
3.2.2 Vortex Structures and Bending Patterns 43
3.2.3 Comparison to Stationary Swimmer 46
3.2.4 Relationship between Economy and Driving Force 48
3.2.5 Relationship between Velocity and Kinematics 50
3.2.6 Strouhal Number Dependence 52
3.3 Summary 54
IV SHAPE EFFECTS OF PLUNGING FLEXIBLE PLATES IN FREE SWIMMING 55
4.1 Introduction and Computational Setup 55
4.2 Results and Discussion 57
4.2.1 Rectangular Swimmer: Performance Characterization 57
4.2.2 Rectangular Swimmer: Bending Patterns and Vortex Structures 61
4.2.3 Vortex-Induced Drag 62
4.2.4 Trapezoidal Swimmer: Performance Characterization 64
4.3 Summary 66
V FREE SWIMMING OF FLEXIBLE PLUNGING PLATES WITH TAPERED THICKNESS 69
5.1 Introduction and Computational Setup 69
5.2 Results and Discussion 71
5.2.1 Performance Characterization of Tapered Rectangular Swimmer 71
5.2.2 Tapered Rectangular Swimmer Bending Patterns 74
5.2.3 Characteristics of Tapered Euler-Bernoulli Beam 75

5.2.4 Curvature and Moment of Tapered Rectangular Swimmer . . 77
5.2.5 Performance Characterization of Tapered Trapezoidal Swimmer 81
5.3 Summary 84
VI FREE SWIMMING OF INTERNALLY ACTUATED OSCILLATING PLATES 85
6.1 Introduction and Computational Setup 85
6.2 Results and Discussion 88
6.2.1 Swimming Velocity 88
6.2.2 Bending Patterns 91
6.2.3 Power and Swimming Economy 94
6.3 Summary 97
VII TURNING STRATEGIES FOR OSCILLATING FLEXIBLE PLATE SWIMMERS 99
7.1 Introduction and Computational Setup 99
7.2 Results and Discussion 102
7.2.1 Asymmetric Plunging 102
7.2.2 Combined Plunging and Rotation 105
7.3 Summary 112
VIII CONCLUDING REMARKS AND OUTLOOK 113
APPENDIX A — MODE SHAPES OF TAPERED EULER-BERNOULLI CANTILEVER BEAM 117
REFERENCES 119
VITA 131

LIST OF TABLES

1 Grid sizes for various studies in this dissertation. Length of domain is related to number of grid points as $L_{c,i} = \Delta_c(N_{c,i} - 1)$ and $L_{f,i} = \Delta_f(N_{f,i} - 1)$. 19

LIST OF FIGURES

1 Fin structure of generic fish. Most fish use caudal fins for propulsion with pectoral and pelvin fins for stabilization. Adapted from [9]. ©1999 IEEE. 3

2 Schematic of LBM distribution functions in the D3Q19 model. Arrows represent the discrete velocities $\mathbf{c}_i$. 14

3 Representation of single unit cell (bordered by dashed lines) in LSM model. Mass node i (center) is connected by springs (solid lines). Stretching springs with stiffness k_s are defined for every ij pair. Torsional springs with stiffness k_b placed at node i are defined for every collinear jik triple (3 in total for this unit cell). 15

4 Schematic of computational domain. The outer box bordered by solid lines represents the coarse LBM grid, while the fine LBM grid is bordered by the dotted line. The swimmer lies within the fine LBM grid. 18

5 Lattice spring model of rectangular swimmer with aspect ratio $AR = 2.5$. Open squares indicate prescribed nodes at the leading edge, while the circles represent passive mass nodes. 21

6 LSM model of trapezoidal shaped swimmer. Here, the width ratio is $w_R = w_l/w_t = 0.25$. Open squares indicate prescribed nodes, while filled circles represent passive mass nodes. 23

7 (a) Lattice spring model (LSM) triangular lattice of flexible plate. Open squares indicate nodes at the boundary that are restricted in the vertical direction. Darker and lighter circles indicate mass nodes in the active and passive portions, respectively. (b) Distribution of external forces on single bending unit to model a local couple at the center node. 26

8 Drag and lift coefficients for plate undergoing insect-like hovering stroke. Present results show agreement to previous experimental and computational work [117]. 28

9 Static deflection of tapered swimmer. The LSM model predicts deflection that agrees well with the analytical solutions for different taper ratios even with large tip deflections. 30

10 Static deflection of an internally actuated plate with active and passive sections. Symbols represent LSM simulations, while lines represent the analytical solution. Good agreement is found between simulations and theory. 31

11 Contours of deflection of trapezoidal plate with width ratio $w_R = 0.25$ corresponding to (a) LSM model and (b) ANSYS finite element solution. Both the ANSYS and LSM contour plots show qualitatively very good agreement, and the centerline plot in (c) confirms this. 33

12 (a) Schematic of elastic swimmer. The swimmer has width w, length L, and is actuated sinusoidally at the leading edge with displacement $A(t) = A_0 \cos(\omega t)$. The trailing edge displacement amplitude is denoted by δ_t. Overlaid are instantaneous snapshots of the swimmer's bending shape while in motion. (b) Side view and (c) top view of the swimmer in motion (dark outline) with vortex structures in its wake. 38

13 (a) Steady state forward swimming velocity and (b) input power as functions of driving frequency ratio for elastic swimmers with Re = 250, $AR = 2.5$, and different values of added mass T. Swimming velocity peaks near the natural frequency at $\phi_{MV} \approx 1.1$, independent of added mass. However, swimming at this frequency requires higher input power, particularly for swimmers with smaller added mass. . . . 39

14 Swimming economy as a function of driving frequency ratio for elastic swimmers with Re = 250, $AR = 2.5$, and different values of added mass T. Economy is highest off resonance at $\phi_{ME} \approx 1.7$. Swimming near the natural frequency results in low economy, particularly for heavier swimmers. 40

15 (a) Trailing edge displacement and (b) center of mass (CM) displacement as functions of frequency ratio for elastic swimmers with Re = 250, $AR = 2.5$, and different values of added mass T. Both displacements are maximized near the natural frequency. Near ϕ_{ME}, the CM displacement has a minimum for lower T. 42

16 Flow structures generated by elastic swimmers with $T = 1$, Re = 250, $AR = 2.5$ driven at (a) the maximum velocity frequency $\phi_{MV} = 1.1$ and (b) at the maximum economy frequency $\phi_{ME} = 1.7$. The semi-transparent surfaces illustrate vorticity surfaces of constant magnitude $\psi = 4$. 43

17 Bending patterns of elastic swimmers driven at (a) $\phi_{MV} = 1.1$ and (b) $\phi_{ME} = 1.7$. Each line represents an instantaneous swimmer profile. The profiles are shown at equal time intervals during one oscillation period. The solid lines depict the upstroke, while the dotted lines depict the downstroke profiles. (c) Leading edge displacement and swimmer deflection as functions of time during one period of swimmer oscillations. Swimmer parameters are $T = 1$, Re = 250, and $AR = 2.5$. 45

18 (a) Phase difference as a function of ϕ between leading edge displacement and swimmer deflection for stationary and moving swimmers with $T = 1$. The horizontal dotted line represents a phase of $\pi/2$ corresponding to swimmer natural frequency. (b) Natural frequencies and maximum deflection frequencies for stationary and moving swimmers as a function of added mass. The dotted line shows the frequency of maximum velocity ϕ_{MV}, while the dash-dotted line shows $\phi = 1$ corresponding to the resonant frequency of a stationary swimmer predicted by linear theory [91]. 47

19 (a) Driving force and leading edge velocity as a function of time for an elastic swimmer with $T = 1$, Re $= 250$, and $AR = 2.5$. The force and leading edge velocity are normalized by $F_0 = 0.5\rho U_0^2 wL$ and U_0, respectively. (b) Magnitude of driving force as a function of frequency ratio for swimmers with different values of added mass T. Driving force is minimized at the frequency of maximum economy, ϕ_{ME}. 49

20 Free swimming velocity as a function of (a) trailing edge displacement and (b) angle ratio for elastic swimmers with Re $= 250$ and $AR = 2.5$ driven with frequency ratios in the range $0.6 < \phi < 2$. For smaller displacements, velocity and displacement have nearly a linear relationship. For larger displacements, swimming velocity saturates. The velocity saturation is more apparent when the angle ratio is greater than 1. . 51

21 Strouhal number as a function of swimming economy for elastic swimmers with Re $= 250$, $AR = 2.5$, $0.5 < T < 7.5$ driven with frequency ratios in the range $0.6 < \phi < 2$. The dimensionless number is defined using two different length scales: leading edge displacement, St_l, and trailing edge displacement, St_t. For the majority of natural flyers and swimmers, studies [73–76] have shown that $0.2 < \mathrm{St} < 0.4$. This region is bounded by the dotted lines. 53

22 Schematic of swimmers with aspect ratios (a) $AR = 5$, (b) $AR = 1$, and (c) $AR = 0.5$ (L is kept constant between the 3 cases). In all cases, the leading edge undergoes a sinusoidal plunging motion with amplitude A_0. Overlaid are transparent snapshots of the bending pattern at different instants of time during one period when the swimmers are actuated at the natural frequency. 56

23 (a) Free swimming velocity and (b) maximum trailing edge displacement as a function of frequency ratio for different aspect ratios. Both quantities are maximized near the first natural frequency. It is interesting that low aspect ratio swimmers can move fastest despite having a smaller trailing edge amplitude. 58

24 (a) Power per unit width and (b) swimming economy for swimmers with different aspect ratios. Power is maximized near the first natural frequency, while swimming economy has a maximum away from $r = 1$ which depends on aspect ratio. Low aspect ratio swimmers are found to be the most economical. 60

25 Bending patterns for different aspect ratios at the maximum velocity and the maximum economy regimes. 62

26 Vortex structures during the maximum velocity for (a) $AR = 5$ and (b) $AR = 0.5$ and during the maximum swimming economy for (c) $AR = 5$ and (d) $AR = 0.5$. Surfaces of constant vorticity magnitude plotted at the same scale. Vorticity magnitude contours within a slice in the yz–plane at the trailing edge during the instant of the fastest trailing edge movement for (e) $AR = 5$ and (f) $AR = 0.5$ at maximum velocity. Vorticity magnitude is normalized by the driving frequency $\omega/2\pi$. 63

27 (a) Free swimming velocity and (b) maximum trailing edge displacement as functions of frequency ratio for trapezoidal swimmers. Both quantities are maximized near the first natural frequency. It is interesting that $w_R = 4$ has a high trailing edge amplitude but moves nearly the same speed as the others. 65

28 (a) Power and (b) swimming economy for swimmers with different aspect ratios. The power is normalized by the same characteristic power for $AR = 1$ swimmers. The curves for different w_R behave similarly to one another. 67

29 Schematic of the rectangular tapered swimmer. (a) The swimmer is modeled as an elastic plate with length L and width w. (b) The thickness of the plate starts at b_l at the leading edge and decreases linearly to a thickness of b_t at the trailing edge. This schematic is not drawn to scale, but $b(x) \ll L$ for the entire length of the plate. (c) Snapshots of the swimmer deformation pattern while in motion. The leading edge oscillates in a sinusoidal plunging pattern with amplitude A_0. 70

30 (a) Swimming velocity and (b) input power for tapered rectangular swimmers. Tapered swimmers exhibit less swimming velocity variation with frequency than uniform swimmers. 72

31 Swimming economy as a function of frequency ratio r for tapered rectangular swimmers. Tapered swimmers exhibit high economical performance for a large range of frequency ratios above $r = 1.5$. 73

32 Trailing edge displacement as a function of frequency ratio r. At higher frequencies, tapered swimmers have larger TE displacements, while that of uniform swimmers approach the plunging amplitude. 74

33 Bending patterns for tapered and uniform swimmers with values of a and r labeled as such. Tapered and uniform swimmers have similar bending patterns at $r = 1.1$, but the tapered swimmer exhibits larger curvature near the trailing edge for $r = 3.1$, resulting in sustained forward swimming at higher frequencies. 75

34 Mass-normalized first mode shape of tapered Euler-Bernoulli beam with different values of a. The mode shapes for the tapered beam have larger curvature near the free end. 76

35 (a) Normalized curvature and (b) moment of tapered Euler-Bernoulli beam first mode. Curvature near the free end increases with increasing a, but moment curves near the free end have similar values. 77

36 (a) Curvature and (b) moment profiles for the swimmers highlighted in Figure 33. The tapered swimmers exhibit larger curvature further down the length at $x/L = 0.6$. At this same length, moment is only slightly increased. 79

37 Driving force amplitude as a function of frequency ratio. Driving force is minimized at approximately $r = 1.7$ to 1.9, corresponding to that of maximum swimming economy. This trend is consistent with results in Chapter 3. 80

38 (a) Velocity and (b) power for tapered trapezoidal swimmers with $a = 5$ and $w_R = 0.25, 1, 4$. Broken lines indicate uniformly thick trapezoidal swimmers for comparison. Both the velocity and power exhibit trends common to both a tapered rectangular swimmer and a trapezoidal uniformly thick swimmer. 82

39 Swimming economy curves for tapered trapezoidal swimmers. Tapered trapezoidal swimmers exhibit sustained high swimming economy at post-resonance frequencies compared to uniform trapezoidal swimmers. 83

40 Schematic of internally actuated flexible plate with passive attachment. (a) Geometry of plate showing the dimensions and size of the active portion (darker shade) and passive portion (lighter shade). (b) Oscillating internal moment in the active section leads to asymmetric bending patterns that generate propulsion. 87

41 Dimensionless swimming velocity as a function of frequency ratio. Velocity is maximized near the first natural frequency for all active section sizes. At higher frequencies, the plate with either $d/L = 0.4$ or 0.6 achieves the fastest swimming speeds. 89

42 (a) Trailing edge deflection as a function of frequency. Despite higher velocity at higher frequencies for $d/L \geq 0.4$, trailing edge deflection remains nearly the same for these swimmers and fully actuated swimmer with $d/L = 1$. (b) Velocity vs. trailing edge deflection, showing that in general a larger trailing edge deflection implies faster swimming. 90

43 (a) Time history of trailing edge kinematics for plates with $d/L = 1$ and $d/L = 0.6$ at $\phi = 2$. Note that the trailing edge deflection and angle are out of phase for $d/L = 1$. Snapshots of deflection curve are shown for (b) $d/L = 1$ and (c) $d/L = 0.6$. The negative slope at the trailing edge for $d/L = 1$ contributes to loss of swimming performance. 92

44 Phase between trailing edge deflection and angle as a function of frequency ratio. The passive flap causes the phase to stay nearly zero in a wide frequency range for $d/L = 0.6$ and smaller, which contributes to better swimming performance. 94

45 (a) Power and (b) swimming economy as a function of frequency ratio. With decreasing d/L, power decreases while swimming economy increases. Plates with passive flaps exhibit better swimming economy as well as faster velocity. 95

46 Swimming economy as a function of center of mass deflection of internally-actuated swimmers. Swimming economy generally decreases with increasing center of mass deflection with the exception of the poorer cases corresponding $d/L = 1$ and $d/L = 0.8$ at high frequencies. 96

47 Schematics of (a) asymmetric plunging actuation and (b) combined plunging and rotation as turning strategies for biomimetic flexible plate swimmer. (c) Plots of the leading edge displacement for different values of velocity ratio v_1/v_2 as asymmetric plunging strategy. 101

48 Thrust and lift on asymmetric plunging swimmer. Lift and therefore turning moment increases monotonically with velocity ratio. 103

49 (a) Displacement time history and (b) bending profile at times A, B, and C, corresponding to times $t/\tau = 0$, 0.16, and 0.5, respectively. The asymmetry in the bending pattern is mainly caused by the quick movement from A to B. 104

50 (a) Propulsive and (b) lateral forces for combined plunging and rotating swimmer. Propulsive forces decrease with increasing α_0, which is related to the smaller projected areas for increasing α_0. Lateral force is maximized in a range of phase values $\psi = -\pi/12$ and $\psi = 5\pi/12$. . 106

51 Turning moment for combined plunging and rotating swimmer. The moment follows similar trends to lateral force. 107

52 (a) Schematic showing rotating $(xyz)'$ axes relative to the fixed (xyz) axes. (b) Perspective of swimmer in $(xyz)'$ axes. (c) Absolute and relative deflections of the trailing edge corner points. The relative deflection of the corner points nearly coincide, showing that the swimmer has negligible twist motion. 108

53 Time histories of relative trailing edge velocity for a plunging plate with no rotation showing the time of maximum vertical force production relative to the maximum trailing edge velocity. 109

54 Time histories for multiple quantities for $\alpha_0 = \pi/4$ and $\psi = \pi/6$. Large lateral force and turning moment are produced because the time of maximum force production based on the relative TE velocity is tuned to the maximum of α. 110

55 Time histories for multiple quantities for $\alpha_0 = \pi/4$ and $\psi = 7\pi/12$. Little lateral force and moment production is due to the time of maximum force production occuring when $\alpha \approx 0$, so force is directed vertically, not laterally. 111

SUMMARY

Motivated by the incredible agility of fish and underwater aquatic mammals, scientists and engineers have sought to design biomimetic propulsion devices that can maneuver underwater with similar speed and efficiency. Robotic fish designs range from complicated models that replicate real fish to simple flexible flapping plates that represent abstractions of fish locomotion. Despite the apparent simplicity of flexible oscillating plates, the thrust and swimming performance of an oscillating fin is dictated by the three dimensional interplay between inertia, elastic forces, and forces due to fluid-structure interaction. Thus, understanding the coupled hydrodynamics and solid mechanics of even a simple oscillating fin in a viscous fluid remains a challenge. In particular, if the plate is driven near the first natural frequency, the bending response is amplified due to resonance, which may increase swimming performance.

In this work we use fully coupled, three-dimensional FSI simulations to investigate the swimming performance of a simplified biomimetic propulsor. The computational model is a lattice Boltzmann method for the fluid mechanics integrated with a lattice spring method to simulate the solid mechanics. The biomimetic swimmer is modeled as an oscillating elastic plate, and we hypothesize that resonance oscillations would contribute to increased swimming performance. We undertake a systematic study of multiple design parameters such as mass, shape, non-uniform thickness, and actuation patterns, in order to understand the physics of the swimmer in free locomotion, i.e. when it cruises forward with a balance of thrust and drag. Second, we explore strategies to control the direction of swimming by imposing asymmetric actuation patterns.

We find that resonance oscillations enhance swimming speed at the expense of increased input power. A second regime is found in which swimming economy, the ratio between velocity and power, is maximized. The different regimes are associated with specific bending patterns. In addition, low aspect ratio (wider span) plates exhibit increased swimming speed and economy. Swimmers with a tapered thickness are more economical at a wider range of frequency ratios than uniformly thick swimmers. Furthermore, we find that a passive fin attachment on an active moment-driven swimmer, akin to smart material propulsors, increases speed and efficiency. Finally, we quantify two possible methods to perform yaw and pitch turning for three-dimensional swimming strategies. While our results are primarily applicable for the design of simple biomimetic propulsors, they may shed light on some of the reasons many fish have tapered, low aspect ratio caudal fins.

CHAPTER I

INTRODUCTION

1.1 Overview

Fish and other aquatic mammals display incredible agility and speed using oscillating flexible fins. By controlling their specific bending patterns and leveraging their flexibility, fish can change direction, turn around, and accelerate forward suddenly. Indeed, the motions of individual fins have been found to be highly complex and mostly three dimensional [1–3]. The incredible performance found in nature serves to inspire the design of small scale biomimetic underwater vehicles that use oscillating fins in order to maneuver like fish. Such biomimetic vehicles have applications in underwater remote sensing, pipe inspection, and ocean sampling [4–8].

In order to control the propulsion and swimming direction of a biomimetic vehicle, the underlying physics of an oscillating fin in a viscous fluid must be understood. An oscillatory fin generates complex vortex flows in the surrounding fluid that fish use to enhance their forward propulsion. In addition, a flexible fin undergoes significant shape changes during locomotion. The thrust and swimming performance of an oscillating fin is dictated by the three dimensional interplay between inertia, elastic forces, and forces due to fluid-structure interaction. Thus, understanding the coupled hydrodynamics and solid mechanics of even a simple oscillating fin in a viscous fluid remains a challenging problem. In particular, the bending patterns that result from driving a flexible plate depend on the ratio between the natural frequencies and the driving frequency. If the plate is driven near the first natural frequency, the bending response is amplified due to resonance, which may increase swimming performance.

In this work, we seek to understand the unsteady physics behind the performance

of oscillating biomimetic flexible fins using fully-coupled three-dimensional computational simulations of a simplified model. Specifically, we model the fin as an oscillating elastic plate, and we hypothesize that resonance oscillations from the plate flexibility would contribute to increased swimming performance. To test our hypothesis, we first undertake a systematic study of multiple design parameters to understand the physics of the oscillating plate undergoing free swimming — that is, when the plate cruises forward in a single direction due to a balance between drag and thrust. A baseline understanding is first established for a uniformly thick plate with a passive plunging actuation in free swimming, and then we probe the effect of shape changes, non-uniform thickness, and internal actuation. Second, we explore strategies to control the direction of the swimming by imposing asymmetric actuation patterns. The results of our research are not only be useful for the design of biomimetic underwater vehicles but also reveal further insights into the fundamental unsteady physics governing the motion of aquatic animals swimming using their oscillating fins.

1.2 Background and Literature Review

1.2.1 Designing Mechanical Fish-like Propulsive Systems

In order to design a biomimetic robotic device, the basic swimming kinematics of real fish must be understood. Fish locomotion is characterized by two major swimming modes: body and caudal fin (BCF) and median and paired fin (MPF) [9, 10]. An illustration of the fin structure of a generic fish is shown in Figure 1. For the BCF mode, fish bend their bodies, propagating a traveling wave continuously from the middle of their bodies to their caudal fins. This mode is associated with the common perception of fish swimming. For the MPF mode, fish use their pectoral fins on both sides for propulsion and pelvic fins for stability. Most fish use BCF as their primary mode for propulsion [10], and use MPF modes for maneuvering and stabilization [11]. Some fish use pectoral and dorsal fins for secondary thrust generation at low speeds;

at high speeds, the thrust is mainly generated from the body and tail oscillations [12–14]. The combination of multiple fins used in locomotion certainly poses multiple layers of complexity for a biomimetic design. Indeed, most robotic fish designs employ a BCF mode of swimming as is it the simplest propulsion model requiring the fewest degrees of freedom [10].

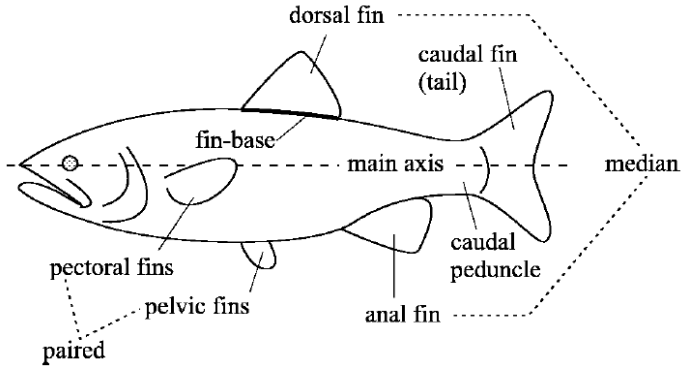

Figure 1: Fin structure of generic fish. Most fish use caudal fins for propulsion with pectoral and pelvin fins for stabilization. Adapted from [9]. ©1999 IEEE.

Motivated by the speed and agility of swimming fish, scientists and engineers have designed wide variety of mechanical fish-like robots, ranging from complicated devices that aim to accurately reproduce fish kinematics to simple mechanical devices that represent basic abstractions of fish features. Since the MIT RoboTuna [15], there have been hundreds of mechanical fish design realizations with complicated designs. One prominent example is from the work of Lauder, et al. [13, 16–19], who constructed biorobotic models of the pectoral and caudal fins on a bluegill sunfish. This particular fish has characteristics representative of a generic fish, and substantial kinematic and behavioral data exist for the sunfish. They use their biorobotic model to understand the locomotor performance of biomimetic flexible fins as well as quantitatively compare the mechanical swimming performance to that of live fish. Many of these conventional aquatic machines with complex designs employ servomotors or hydraulic actuators in conjunction with a series of linked rigid sections in order to mimic body flexibility in a single bending plane [20–24]. However, generating a large range of

three-dimensional fin strokes requires a complicated and cumbersome system of links and pulleys. Although well-studied, these motor-based actuators still cannot match the swimming performance of biological fish.

Simple mechanical models, such as oscillating plastic strips or flexible rectangular panels, represent basic abstractions of fish-like propulsion. As simplified models of the complex nature of fish swimming, these devices are often used to experimentally study the fundamental physics behind oscillating fish-like propulsion. Passive propulsive systems are constructed by attaching a rod controlled by motors to the leading edge of the panels, which are submerged in a recirculating tank [25–27]. By imposing a plunging motion on the leading edge, a continuous traveling wave moves down the panel, generating thrust in a similar way as live fish. Thrust and free swimming measurements can be performed by attaching sensors to the rod and adjusting the flow speed in the tank.

Recently, simple mechanical fish-like designs have also employed internally-actuated (active) smart materials as propulsors. Smart materials have material properties that can be controlled by external stimuli such as temperature and electromagnetic fields. These smart materials can be adapted to perform complex fish-like motions and controlled to follow different strokes without the physical complexity of motor-based designs. Typical smart materials used for biomimetic swimming devices include ionic polymer-metal composites (IPMCs) [28–34], shape memory alloys (SMAs) [35–40], magnetostrictive thin films [41–43], and others [44–46]. Among other active smart materials, piezoelectric actuators are attractive because of their geometric scalability, high efficiency, and noiseless performance [47]. Despite these advantages, the current understanding and usage of piezoelectric actuators in swimming devices is still limited [48–51].

1.2.2 Previous Work on Physics of Fish-like Propulsion

Even for the simplest oscillating flexible plate propulsors and swimmers, the locomotion physics is governed by a dynamic interplay between the fluid dynamics and elastic deformation. Because of this problem's intrinsic complexity, studies have typically considered simplified, two-dimensional models, such as a harmonically oscillating rigid plate or airfoil in an inviscid fluid allowing for a more tractable analysis. Early researchers have developed a linear theory of oscillating airfoils by studying flutter [52–54]. The theoretical models continued with the development of the slender body theory [55–58]. This culminated in the work of Lighthill, who studied the reactive forces between an oscillating slender body and its surrounding fluid [59–62]. He proposed that the mean thrust depends on the tip velocity, tip angle, and mass ratio of the swimmer in quiescent conditions. These inviscid models have been recently extended to three dimensions [63]. Inviscid models provide only a first approximation to the coupled hydrodynamics because viscosity effects can be significant in small scale oscillating fins. Thus, numerical and experimental studies are necessary to fully investigate the performance characteristics and physics of oscillating swimmers.

Such numerical and experimental studies have been recently conducted to probe the three-dimensional hydrodynamics of swimming using a variety of kinematics [64–66]. Buchholz and Smits [67, 68] used experiments to measure the wake structure and thrust performance of a rigid rectangular panel in a pitching motion. They visualized the wake and created a skeleton model of horseshoe shaped vortices that were shed. Their wake model was found to be consistent throughout a wide range of Reynolds numbers from $\mathrm{Re} = 640$ to $\mathrm{Re} = O(10^4)$. Facci and Porfiri [69, 70] used experiments and numerical simulations to study a plunging fin in a viscous fluid. They developed a theory for small deflections and investigated 3D effects. Their numerical model used a prescribed motion of the fin. Ramananarivo et al. [71] experimentally studied the free swimming of anguilliform motion and analyzed it using a coupled potential

flow model. Alben et al. [72] performed experiments and developed an inviscid theoretical model of the free swimming of a plunging elastic plate at a relatively high Reynolds number. They found the existence of resonant-like peaks in the free swimming velocity.

Many studies have also probed criteria for efficient swimming — that is, how to best translate input power into useful output. When the output is forward thrust, the Froude efficiency can used to quantify thrust efficiency [59]. The optimal thrust efficiency is usually linked to certain values of the Strouhal number, St. Studies have shown that natural fliers and swimmers, such as birds, insects, and fish, move freely with Strouhal numbers in the range $0.2 < \mathrm{St} < 0.4$ [73]. This range has been linked to efficient modes of swimming and flying [74–76].

To corroborate this statement, Dai et al. [77] used numerical simulations of pitching flexible plates and found a high efficiency regime around $\mathrm{St} = 0.4$. Dewey et al. [78] performed experiments on flexible pitching panels — at a higher Reynolds number and smaller mass ratio than Dai's study — and found that thrust efficiency (among the highest efficiencies found) is maximized at resonance in the range $0.25 < \mathrm{St} < 0.35$. Eloy has expanded this optimal range to $0.15 < \mathrm{St} < 0.8$ by minimizing the power loss based on Lighthill's reactive theory and compared this to aquatic animals of all sizes [79]. Recently, a scaling argument was used to show the dependence of Strouhal number with Reynolds number [80], suggesting that the Strouhal number decreases with increasing Reynolds number until reaching a limit. Moored et al. [78, 81, 82] has suggested that swimming with maximum efficiency is linked to the growth of the instability of the time averaged wake (termed the wake resonance theory). Other studies with flexible flapping wing flyers have indicated off-resonance efficiency peaks [83–86].

Since fish fins have non-rectangular geometry, several recent studies have explored the effect of shape on the swimming using undulating fins. Li, et al. [87] investigated

the thrust performance of rigid three-dimensional plates with a non-rectangular geometry that represented a forked tail fin and found that forked fins are more efficient than rectangular fins. Other studies sought to optimize the fin shape using both Lighthill's theory [88, 89] and viscous flow simulations with fully prescribed kinematics [90]. Each of these studies produced optimal shapes that roughly resembled a real fish — a streamlined body with a caudal fin appendage — but differ between studies. These differing outcomes and conclusions from each study likely stem from different optimization algorithms and flow parameters. For example, Tokic and Yue [89] compared their optimal shapes to real fish and found that they are similar. On the other hand, van Rees et al. [90] found optimal shapes that differ from real fish and showed that they even outperform real fish.

1.2.3 Current Research Challenges

While all of these studies provide important insights, system parameters usually differ widely from one study to next. Thus, the current literature lacks a systematic investigation of the effects of flexibility on the hydrodynamics of oscillating fins, particularly in understanding the effects of resonance and changing bending patterns. When a flexible plate is submerged in a fluid and driven by a periodic actuation pattern, the resulting bending pattern depends on the material properties based on the proximity to its natural frequency, which is different while submerged in a fluid than in air because of added mass effects [91]. Many studies have simply probed the effect of increasing driving frequency, but increasing the driving frequency changes both the bending pattern and increases the Reynolds number, which changes the thrust mechanisms [92]. For oscillating plate propulsors that have comparable density to the fluid, the effect of resonance may not be as pronounced because of very high fluid damping. However, for comparably heavier oscillating fin designs, we expect resonance effects to be fundamentally important to the swimming performance, and we hypothesize that

resonance oscillations can be used to enhance the speed and efficiency of biomimetic fin propulsors.

Many studies have also focused on the one-dimensional forward thrust of a flexible plunging plate, whereas free swimming in three dimensions has not been investigated. Therefore, it is unclear how thrust performance predicts actual swimming performance. Under free swimming, the swimmer experiences different bending patterns than under constrained plunging. In this coupled system, the different deformation patterns affect the produced hydrodynamic forces, which in turn affect the deformation. Furthermore, swimming efficiency is not well understood despite many studies that quantify and theorize different mechanisms for efficient thrust generation. The definition of efficiency itself under free swimming is not well established because thrust and drag cannot be decoupled.

Furthermore, most of the previous studies have only considered flexible rectangular plates with uniform thickness under unidirectional thrust generation or swimming. Studies that probe the effects of shape change, such as using trapezoidal-shaped fins (similar to fish) are limited. Plates with non-uniform thickness have not been systematically addressed in the literature to the best of our knowledge. Moreover, strategies to direct the thrust in different directions in three-dimensional space also have not been investigated in detail using numerical simulations.

Systematic experimental investigations are typically limited by equipment and a finite number of flexible panels of which to test. For this reason, numerical simulations provide an attractive option for a systematic understanding of the physics of oscillating swimmers. Past numerical investigations have been limited by computational power and as such, usually studied two-dimensional flows with a rigid fin attached to a hinge or a fin with prescribed kinematics. Thus, a systematic investigation on the hydrodynamics of oscillating flexible fins using fully coupled numerical simulations does not exist in the literature to the best of our knowledge.

1.3 Research Objectives and Scope

The objective of this dissertation is to study the fluid-structure interaction physics and quantify the performance of a simple flexible plate propulsor driven near resonance. Our work answers the following questions: (1) how resonance oscillations and bending patterns influence unidirectional free swimming speed and efficiency; (2) how mass, shape, and non-uniform thickness affect bending response and swimming performance; (3) how a combination of internal actuation (akin to smart material propulsors) and passive actuation changes the swimming dynamics; (4) how the direction of thrust can be altered by asymmetric actuation patterns in order to examine strategies to turn and change direction. In analyzing the free swimming performance, we quantify the proximity to the first natural frequency using parameters (discussed in Chapter 2) that represent the ratio between the driving and natural frequencies. Because the resulting bending pattern is a function of this frequency ratio, varying the frequency ratio allows us to systematically vary the bending pattern. We actuate near the first natural frequency at which resonance oscillations are most prominent. Furthermore, we keep the Reynolds number constant in the $O(100)$ regime, in which there are negligible lift effects from an asymmetrically deflected flow field (as in airfoils) or turbulence effects, and the primary form of thrust generation is due to added mass acceleration — the bending plate pushes fluid backwards, generating a reaction force [92]. This regime is relevant for the slow swimming of small fish or designs of micro-robotic fins on the order of 1 cm swimming at 1 cm/s.

In order to accomplish these research goals we use a three-dimensional fluid-structure interaction (FSI) computational model. Our fluid mechanics solver is a lattice Boltzmann method with two relaxation times, while the solid mechanics will be modeled using a lattice spring method that capable of accurately simulating relatively large deformations. The solvers are two-way coupled via boundary conditions.

This fully coupled model can capture both the swimmer deformations and the relevant hydrodynamic flow structures, allowing us to investigate precisely the effects that lead to optimal swimming performance of our biomimetic swimmer design.

The rest of this dissertation is organized as follows. Chapter 2 describes the FSI model in detail, discusses how the plate is modeled in LSM, and presents several validation studies. Chapter 3 presents the results for unidirectional free swimming of the plate actuated by a passively plunging motion and establishes a baseline understanding for a swimmer with a fixed thickness and aspect ratio. Chapters 4 and 5 present the results for swimmers with changing shapes and non-uniform thickness, respectively. Chapter 6 presents results for an internally actuated swimmer with a passive fin attachment. Chapter 7 demonstrates successful strategies for directing thrust in three-dimensional space. Finally, Chapter 8 summarizes our results and discusses the outlook for our research.

CHAPTER II

COMPUTATIONAL MODEL

2.1 Fluid-Structure Interaction (FSI) Methodology

We use fully coupled, three-dimensional simulations to capture the transient hydrodynamics and solid deformation of the flexible swimmer submerged in a viscous fluid. The fluid mechanics is solved by using the lattice Boltzmann method (LBM), while the solid mechanics is simulated using the lattice spring method (LSM). The LBM and LSM methods are fully coupled at the boundary conditions and thus fully capture the fluid-structure interaction. Compared with traditional FSI methods, the hybrid LBM/LSM method that we use is highly parallelizable, scalable, and time efficient. The LBM and LSM methods do not require slow matrix inversions as traditional finite difference and finite element codes do. The coupling method between LBM and LSM also does not require multiple iterations to achieve convergence. The disadvantage to LSM is the difficulty to model complex structures and reproduce continuum properties, but in this study we are concerned with simple geometric entities such as plates.

2.1.1 Lattice Boltzmann Method (LBM)

The lattice Boltzmann method is a recent particle-based method that simulates the hydrodynamics of an incompressible Newtonian fluid [93–96]. Instead of discretizing the Navier-Stokes equations as is traditionally done, the discrete Boltzmann equation is solved in LBM. The fluid domain is discretized into a square lattice, and fictitious fluid "particles" are constrained to move along the lattice. The fluid state is characterized by a set of velocity distribution functions, $f_i(\mathbf{r}, t)$, which represent the number density of the fluid "particles" at each node moving with discrete velocity $\mathbf{c}_i$ at lattice

node $\mathbf{r}$ during time t. The number of distribution functions depends on the number of dimensions and specific implementation of LBM. Our simulation algorithm is in three dimensions and uses 19 distribution functions (a D3Q19 method). Specifically, the discrete velocities along the lattice are indexed by the following (see Figure 2a for illustration):

$$\mathbf{c}_i = \begin{cases} (0,0,0), & i = 0 \\ (\pm 1,0,0),(0,\pm 1,0),(0,0,\pm 1), & i = 1,2,\ldots,6 \\ (\pm 1,\pm 1,0),(\pm 1,0,\pm 1),(0,\pm 1,\pm 1), & i = 7,8,\ldots,18 \end{cases} \tag{1}$$

Hydrodynamic quantities, such as fluid mass density ρ, momentum $\mathbf{j}$ and momentum flux $\mathbf{\Pi}$ are computed as moments of the velocity distribution function as such:

$$\rho = \sum_i f_i, \tag{2}$$

$$\mathbf{j} = \rho\mathbf{u} = \sum_i f_i \mathbf{c}_i, \tag{3}$$

$$\mathbf{\Pi} = p\mathbf{I} + \rho\mathbf{u}\mathbf{u} = \sum_i f_i \mathbf{c}_i \mathbf{c}_i. \tag{4}$$

The time evolution of the velocity distribution functions is given by the discrete Boltzmann equation [93]:

$$f_i(\mathbf{r} + \mathbf{c}_i \Delta t, t + \Delta t) = f_i(\mathbf{r}, t) + \Delta_i[\mathbf{f}(\mathbf{r}, t)]. \tag{5}$$

Here, Δ_i is the collision operator and represents the change due to fluid "particle" collisions at each node. We use a double relaxation time collision operator, which gives added stability and is capable of simulating a larger range of Reynolds numbers as compared to a collision operator with a single relaxation time. The post-collision distribution function is given by the following expression:

$$f_i(\mathbf{r}, t) + \Delta_i[\mathbf{f}(\mathbf{r}, t)] = a_i \left[\rho + \frac{\mathbf{j} \cdot \mathbf{c}_i}{c_s^2} + \frac{\left(\rho\mathbf{u}\mathbf{u} + \mathbf{\Pi}^*_{neq}\right) : \left(\mathbf{c}_i\mathbf{c}_i - c_s^2\mathbf{I}\right)}{2c_s^4} \right]. \tag{6}$$

Here, the non-equilibrium momentum flux $\mathbf{\Pi}^*_{neq}$ is given by the following:

$$\mathbf{\Pi}^*_{neq} = (1+\lambda)\overline{\mathbf{\Pi}}_{neq} + \frac{1}{3}(1+\lambda_\nu)(\mathbf{\Pi}_{neq} : \mathbf{I})\,\mathbf{I}. \tag{7}$$

Here, $\mathbf{\Pi}_{neq} = \mathbf{\Pi} - \mathbf{\Pi}_{eq}$ and $\overline{\mathbf{\Pi}}_{neq}$ is the traceless part of $\mathbf{\Pi}_{neq}$. The equilibrium momentum flux is computed from $\mathbf{\Pi}_{eq} = \rho c_s^2 \mathbf{I} + \rho \mathbf{u}\mathbf{u}$. Furthermore, λ and λ_v are the two relaxation parameters in this LBM model. They are related to the shear and bulk viscosities, respectively, as follows:

$$\mu = -\rho c_s^2 \Delta t \left(\frac{1}{\lambda} + \frac{1}{2} \right), \tag{8}$$

$$\kappa = -\rho c_s^2 \Delta t \left(\frac{2}{3\lambda_\nu} + \frac{1}{3} \right). \tag{9}$$

The weights a_i depend on the speed of the distribution $|\mathbf{c}_i|$ and are given by

$$a_i = \begin{cases} 1/3, & |\mathbf{c}_i| = 0 \\ 1/18, & |\mathbf{c}_i| = 1 \\ 1/36, & |\mathbf{c}_i| = \sqrt{2} \end{cases} \tag{10}$$

Finally, the speed of sound $c_s = \Delta x / \sqrt{3} \Delta t$, where Δx is the spacing between the lattice nodes. Typically in LBM simulations both Δx and Δt are set to 1. Thus, the length scales are explicitly defined by the lattice itself, and simulations using dimensional units must be scaled accordingly. Typically, $\lambda_\nu = -1$, which leads to a finite bulk viscosity, implying that the fluid is weakly compressible. The Mach number $\mathrm{Ma} = u/c_s$ must be kept small, typically under 0.15 in order to accurately model an incompressible flow.

The LBM algorithm is divided into two steps, collision and advection as described below:

1. Compute the post-collision distribution function at each lattice node:

$$f_i^* \equiv f_i(\mathbf{r}, t + \Delta t) = f_i(\mathbf{r}, t) + \Delta_i[\mathbf{f}(\mathbf{r}, t)]. \tag{11}$$

2. Propagate the distribution to the neighboring lattice node based on the respective $\mathbf{c}_i$ velocity direction:

$$f_i(\mathbf{r} + \mathbf{c}_i \Delta t, t + \Delta t) = f_i^*. \tag{12}$$

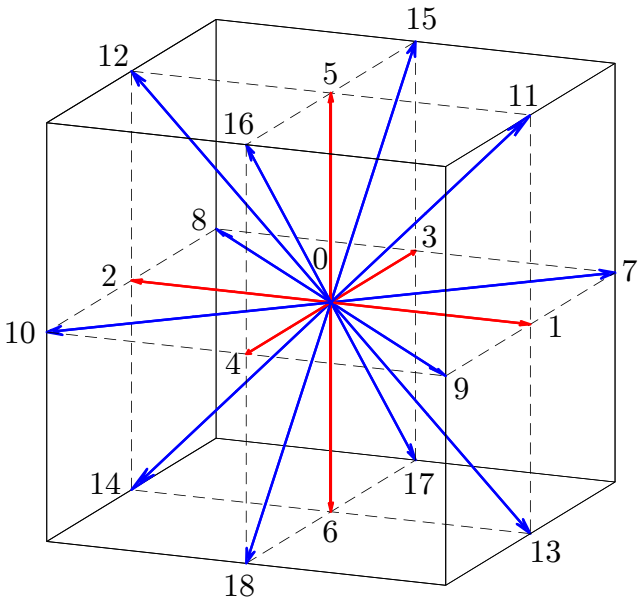

Figure 2: Schematic of LBM distribution functions in the D3Q19 model. Arrows represent the discrete velocities $\mathbf{c}_i$.

One LBM time step consists of both collision and advection steps. The LBM solver is run continuously for a specified number of time steps.

2.1.2 Lattice Spring Method (LSM)

To solve the solid mechanics in our FSI simulations, we employ the lattice spring method (LSM) [97, 98]. LSM is a simpler implementation than many popular solid mechanics solvers such as finite element methods (FEM) that can simulate large deformations and requires less computational power. LSM has also been proven to be equivalent to a special case of FEM in which the springs form element boundaries [97]. In LSM, a continuous solid is discretized as a network of point masses that are interconnected by stretching and torsional springs. The exact mapping to macroscopic elastic properties depends on the type of lattice network. Specifically, triangular and square lattices have been shown to behave like isotropic elastic solids [99]. For all of our swimmer LSM models, we adopt a triangular lattice because it facilitates

implementation of the LSM and LBM coupling, which is based on triangular surface boundary interactions [100].

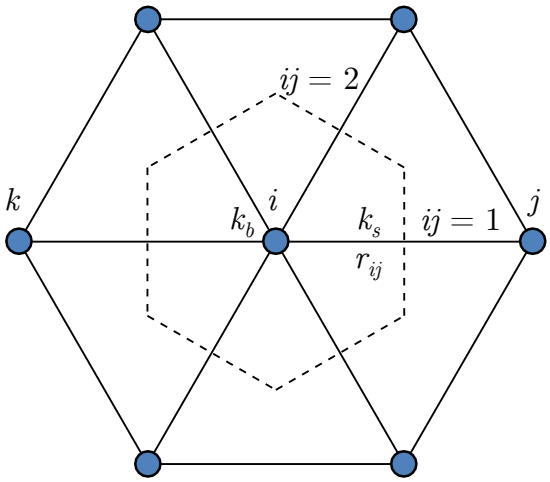

Figure 3: Representation of single unit cell (bordered by dashed lines) in LSM model. Mass node i (center) is connected by springs (solid lines). Stretching springs with stiffness k_s are defined for every ij pair. Torsional springs with stiffness k_b placed at node i are defined for every collinear jik triple (3 in total for this unit cell).

Figure 3 shows an example of a triangular lattice unit. Node i is at the center, surrounded by 6 regularly spaced neighboring nodes. The dotted hexagon represents the unit cell associated with node i. The stretching springs have spring constant k_s, leading to the spring force between neighboring nodes i and j as

$$\mathbf{F}_{s,ij}^{\text{str}} = -k_s \left(r_{ij} - r_0\right) \hat{\mathbf{r}}_{ij}. \tag{13}$$

Here, r_{ij} is the distance between two neighboring nodes, $\hat{\mathbf{r}}_{ij}$ is the unit vector in the direction from i to j, and r_0 is the equilibrium spacing of the LSM nodes. For an isotropic two-dimensional plate, it can be shown that the Poisson ratio is $\nu = 1/3$.

In order to model elastic plates with resistance to bending, torsional springs are added on node i. We define a bending unit as a collinear triplet jik (see Figure 3, where node k is the node directly opposite of node j. For each bending unit (3 of them per unit cell), a bending spring is placed on node i with stiffness k_b which resists

out-of-plane bending. The bending energy associated with a single bending unit is given by the following:

$$U_b = k_b(\cos\theta_{jik} - \cos\theta_0). \tag{14}$$

Here, θ_{jik} is the angle between segments ij and ik, and $\theta_0 = \pi$ is the equilibrium angle. The forces on each of the nodes in the bending unit is thus given by

$$\mathbf{F}^{\text{bend}}_{s,j} = -\frac{k_b}{r_{ij}r_{ik}}\left(\mathbf{r}_{ik} - \frac{\cos\theta_{jik}}{r^2_{ij}}\mathbf{r}_{ij}\right), \tag{15}$$

$$\mathbf{F}^{\text{bend}}_{s,k} = -\frac{k_b}{r_{ij}r_{ik}}\left(\mathbf{r}_{ij} - \frac{\cos\theta_{jik}}{r^2_{ik}}\mathbf{r}_{ik}\right), \tag{16}$$

$$\mathbf{F}^{\text{bend}}_{s,i} = -(\mathbf{F}^{\text{bend}}_{s,j} + \mathbf{F}^{\text{bend}}_{s,k}), \tag{17}$$

where $\mathbf{r}_{ij}$ is the vector from node i to node j. Note that an LSM node can be either an endpoint or a midpoint of a bending unit and thus experiences forces from all bending units with which the node is associated. It can be shown that for a triangular lattice, this bending model leads to a plate bending rigidity $D = 3\sqrt{3}k_b/4$ [101].

The multiple sources of undamped springs may lead to local high frequency oscillations that could cause instabilities in the global solution. In order to mitigate these oscillations, we add a dashpot in between each node. This dissipative force is proportional to the relative velocity between each node projected along the line connecting the nodes:

$$\mathbf{F}^{\text{dis}}_{s,ij} = -\alpha(\mathbf{v}_{ij} \cdot \hat{\mathbf{r}}_{ij})\hat{\mathbf{r}}_{ij}. \tag{18}$$

The value of α is a tuning parameter that we change in order to stabilize the coupled fluid-solid simulations. We have found that changing this value even by multiple orders of magnitude negligibly affected our simulation results (less than 1%).

We represent the total force on node i due to the springs and dashpots in the LSM model as $\mathbf{F}_{s,i}$. In addition, LSM solid nodes may experience forces due to interaction with the fluid, $\mathbf{F}_{b,i}$, and applied external forces, $\mathbf{F}_{e,i}$ that may arise from a prescribed motion or distributed forces and moments. The nature of these forces will be discussed

in the appropriate sections later in this chapter. Then the total force on node i is the sum of all contributions:

$$\mathbf{F}_i = \mathbf{F}_{s,i} + \mathbf{F}_{b,i} + \mathbf{F}_{e,i}. \tag{19}$$

The motion of the solid nodes are integrated forward by numerically solving Newton's second law:

$$\mathbf{F}_i = m_i \frac{d^2\mathbf{r}_i}{dt^2}. \tag{20}$$

We use the velocity Verlet algorithm to perform the numerical integration [102, 103]. This method is second order in accuracy and is widely used in molecular dynamics codes. The steps to compute the position, velocity, and acceleration at the next time step $t + \Delta t$ are the following:

1. Compute the half-step velocity using the known acceleration at time t:

$$\mathbf{a}_i(t) = \mathbf{F}_i(\mathbf{r}_i(t), t)/m_i, \tag{21}$$

$$\mathbf{v}_i(t + \Delta t/2) = \mathbf{v}_i(t) + \mathbf{a}_i(t)\Delta t/2. \tag{22}$$

2. Compute the new position at time $t + \Delta t$ based on the half-step velocity:

$$\mathbf{r}_i(t + \Delta t) = \mathbf{r}_i(t) + \mathbf{v}_i(t + \Delta t/2)\Delta t. \tag{23}$$

3. Derive the new acceleration based on the new position and compute the new velocity:

$$\mathbf{a}_i(t + \Delta t) = \mathbf{F}_i(\mathbf{r}_i(t + \Delta t), t + \Delta t)/m_i, \tag{24}$$

$$\mathbf{v}_i(t + \Delta t) = \mathbf{v}_i(t + \Delta t/2) + \mathbf{a}_i(t + \Delta t)\Delta t/2. \tag{25}$$

Note that in step 3, the forces that are due to dissipation are computed using the half-step velocity. Furthermore, the time step Δt is independent of the LBM time step and does not have to equal 1. In fact, the Δt must be chosen so that $\Delta t < \Delta x/V_p$, where $V_p = \sqrt{(K + 4G/3)/\rho_s}$ is the P-wave velocity [104]. Here, Δx is the lattice spacing. In our simulations we choose a fixed time step $\Delta t = 0.125$, which leads to 8 LSM integration steps for every 1 LBM step.

2.1.3 Computational Domain

We use an ordered three-dimensional grid, refined near the swimmer surface, as our fluid computational domain. Figure 4 illustrates the computational domain used in our coupled FSI solver. The outer box with the solid line represents the main boundaries of the fluid domain, and this outer domain is periodic on all sides. The inner box constructed by dotted lines represents the refined grid near the swimmer. The swimmer itself is placed within the refined grid, and the LSM nodes which compose the swimmer exist and move independently of the fluid nodes.

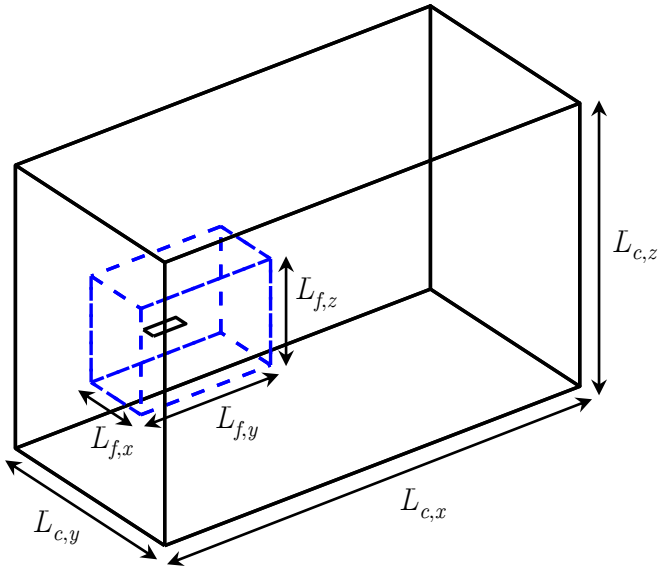

Figure 4: Schematic of computational domain. The outer box bordered by solid lines represents the coarse LBM grid, while the fine LBM grid is bordered by the dotted line. The swimmer lies within the fine LBM grid.

The space contained within the outer grid but outside of the refined grid is deemed the coarse grid. The coarse grid spacing is $\Delta_c = 2$, while the fine grid has spacing $\Delta_f = 1$. The $-x$–plane boundary of the refined grid is located 40 LBM units away from the coarse grid. In the y and z directions, the refined grid box is placed in the center of the coarse domain. The swimmer, which has length $L = 50$ LBM units, is positioned 50 LBM units away from the refined grid $-x$–plane boundary. With respect to the y and z directions, the equilibrium position of the swimmer is located

at the center of the refined grid. The left edge of the swimmer is the leading edge (LE), so the swimmer is expected to swim in the $-x$–direction. In order to study free swimming, we impose a uniform flow in the $+x$–direction and let the swimmer move freely in the horizontal direction. The uniform flow velocity is judiciously chosen so that the swimmer remains nearly in the center of the refined grid.

The coarse and fine grids have sizes that depend on the particular study which we have chosen through grid convergence tests. Table 1 gives the size details for each particular study. In particular, a large grid is required for free swimming simulations in order that the wake sufficiently dissipates before reaching the back boundary. Furthermore, the large grid ensures that the far field velocity does not change appreciably as the swimmer moves around the domain. For the study with changing aspect ratio (see Chapter 4), the swimmer width is varied and the lateral grid size direction is determined in grid convergence studies for each value of the aspect ratio, but the coarse grid is at least 3.6 times as large as the swimmer width, and the refined grid is at least 2.2 times as large as the width.

Table 1: Grid sizes for various studies in this dissertation. Length of domain is related to number of grid points as $L_{c,i} = \Delta_c(N_{c,i} - 1)$ and $L_{f,i} = \Delta_f(N_{f,i} - 1)$.

Study	$N_{c,x}$	$N_{c,y}$	$N_{c,z}$	$N_{f,x}$	$N_{f,y}$	$N_{f,z}$
$AR = 2.5$, fixed (Ch. 3,7)	200	150	200	200	100	150
$AR = 2.5$, free swimming (Ch. 3,5,6)	400	150	200	200	100	150
$AR = 2.5$, plunging & rotation (Ch. 7)	200	150	200	200	150	150
Shape variation, free swimming (Ch. 4)	400	varies	200	200	varies	150

2.1.4 Boundary Conditions and FSI Coupling

Appropriate boundary conditions are set for the coarse grid boundaries, coarse-refined grid boundaries, and the solid-fluid boundary. As stated previously, the coarse grid boundaries are periodic in every direction in order to simulate an unbounded fluid. Specifically, the distribution functions entering the boundary during the propagation

step emerge on the opposite end at the corresponding periodic node. At the coarse-refined grid boundary, a multi-step coupling procedure is employed [105]. Note that this coupling procedure requires the refined grid to be staggered in relation to the coarse grid so that the coarse grid nodes lie in between the refined grid.

We employ a fluid-solid coupling procedure that has been used and extensively tested in previous studies [84, 100, 106–115] which will be briefly discussed here. The positions of the LSM mass nodes locally define triangular surfaces adjacent to fluid nodes. In the LBM model, we employ no-slip and no penetration boundary conditions on these solid surfaces using a linear interpolated bounce-back condition [116]. Specifically, the distribution functions that propagate into the solid surface are reflected back in the opposite direction and modified based on the position and velocity of the intersection point at the solid surface.

The momentum associated with the reflection of the distribution function is transferred to the solid surface. An equivalent force representing this momentum transfer is exerted on the surface at the point where the distribution function bounces back. This force is redistributed to the surrounding three LSM nodes using a weighted average based on distances while conserving normal and tangential forces on the interface. The details of our fluid-solid coupling procedure can be found elsewhere [100].

2.2 Swimmer LSM Models

In this section we describe the specific swimmer LSM models used in the studies within this dissertation. As stated previously in section 2.1.2, the swimmer is modeled as an elastic plate using a triangular lattice of point masses connected by bending and stretching springs. The lattice structure and properties depend on the swimmer geometry as well as the modes of actuation. We detail our LSM models for both rectangular and trapezoidal shapes, uniform and tapered thickness, and passive and internal actuation.

2.2.1 Uniform Rectangular Plate with LE Actuation

Figure 5 shows the triangular LSM lattice for a rectangular plate with length L and width w. As shown, the plate has aspect ratio $AR = L/w = 2.5$. The nodes indicate the point masses, and the straight lines connecting them depict the stretching springs. Bending springs are introduced for all straight-line triplets. The open squares indicate the nodes with prescribed kinematics at the leading edge, while the filled circles represent passive mass nodes. The mass nodes have spacing $\Delta_s = 2.325$. Using this LSM spacing for $AR = 2.5$ as shown in Figure 5, $L = 21.5\Delta_s \approx 50$ and each row has spacing $\Delta_s\sqrt{3}/2 \approx 2$. In order to model a rectangular plate with a different aspect ratio, we keep L constant and change the width by increasing the number of rows while keeping the lattice pattern the same.

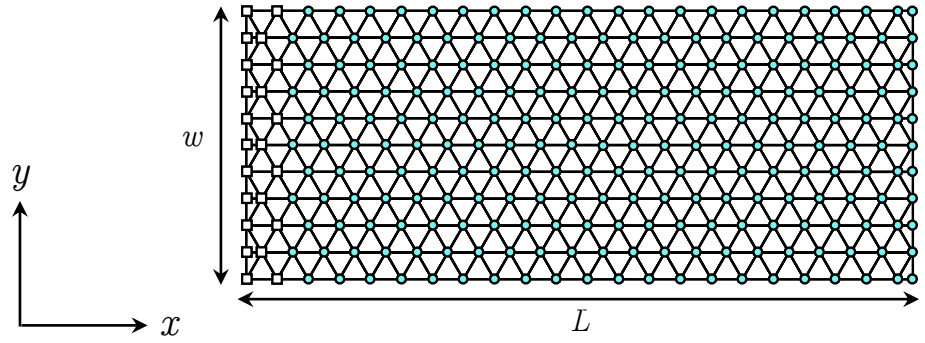

Figure 5: Lattice spring model of rectangular swimmer with aspect ratio $AR = 2.5$. Open squares indicate prescribed nodes at the leading edge, while the circles represent passive mass nodes.

For this isotropic plate model, the nodes have identical masses $m_i = m$ and spring stiffnesses $k_{s,i} = k_s$ and $k_{b,i} = k_b$ except for the ones along the edges, where the local properties are scaled based on the smaller unit cell area surrounding the edge node. These edge effects do not appreciably affect the bending behavior. The identical masses lead to a constant mass per area $\sigma = \rho_s b$. The stretching spring stiffness k_s is set to a relatively high value in order that the plate be nearly inextensible. In these studies we primarily focus on plate bending in the direction normal to the

surface, so k_s is not relevant to the problem physics. For larger aspect ratio plates, of which $AR = 2.5$ is sufficient, the one-dimensional bending rigidity EI characterizes the bending behavior, so the plate behaves like an Euler-Bernoulli beam with large deformation. Using the relation $D = 3\sqrt{3}k_b/4$ and $\nu = 1/3$ from section 2.1.2, we can relate k_b to EI by the following:

$$EI = \frac{3\sqrt{3}}{4} k_b w (1 - \nu^2). \tag{26}$$

We denote the kinematics of the leading edge by $\mathbf{R}_{LE,i}$, where i in this case represents the LE prescribed nodes. In order to prescribe the kinematics, we apply an external force $\mathbf{F}_{e,i}$ that exactly balances the inertia, spring, and fluid forces so that when the nodes are integrated in time, the desired kinematics are reproduced. Mathematically, this is given by

$$\mathbf{F}_{e,i} = m_i \frac{d^2 \mathbf{R}_{LE,i}}{dt^2} - \mathbf{F}_{s,i} - \mathbf{F}_{b,i}. \tag{27}$$

For passing plunging actuation, $\mathbf{R}_{LE,i} = \mathbf{R}_{LE,i}(0) + A(t)\hat{\mathbf{z}}$, where $\mathbf{R}_{LE,i}(0)$ are the initial positions of the LE nodes, and $A(t)$ is sinusoidal for uni-directional thrust or free swimming studies. In free swimming studies, we set $\mathbf{F}_{e,i} \cdot \hat{\mathbf{x}} = 0$ in order to allow the swimmer to move horizontally. For turning strategies using passive LE actuation (see Chapter 7), $\mathbf{R}_{LE,i}$ is a more complicated function and will be discussed in the relevant chapter. Note also that the first two rows of LSM nodes have prescribed actuation (Figure 5), which creates a zero-slope condition at the LE. This models a clamped boundary condition for the plate, which is representative of a fin attached to a larger mass as part of a robotic vehicle design.

2.2.2 Trapezoidal Plate

The trapezoidal plate LSM model is shown in Figure 6, and is used in Chapter 4 to study effects of shape on swimming performance. The leading edge and trailing edge have dimensions w_l and w_t, respectively. In the figure, the width ratio $w_R = w_l/w_t =$

0.25. Similar to the LSM model in section 2.2.1, the filled circles represent passive mass nodes, and the open squares are the LE prescribed nodes. The major difference between the trapezoidal and rectangular plate LSM models is the importance of edge effects. The sloped edges of the trapezoid does not conform well with a triangular lattice, and the unit cells along the edges are irregular and may have high aspect ratios. The edge effects, though small, are appreciable, and may affect the deflection by approximately 5%. In order to correct for the edge effects, the bending stiffness for the torsional springs along the sloped edges are scaled in order that the behavior, as tested by static deflection of an end load, reproduces the continuum properties.

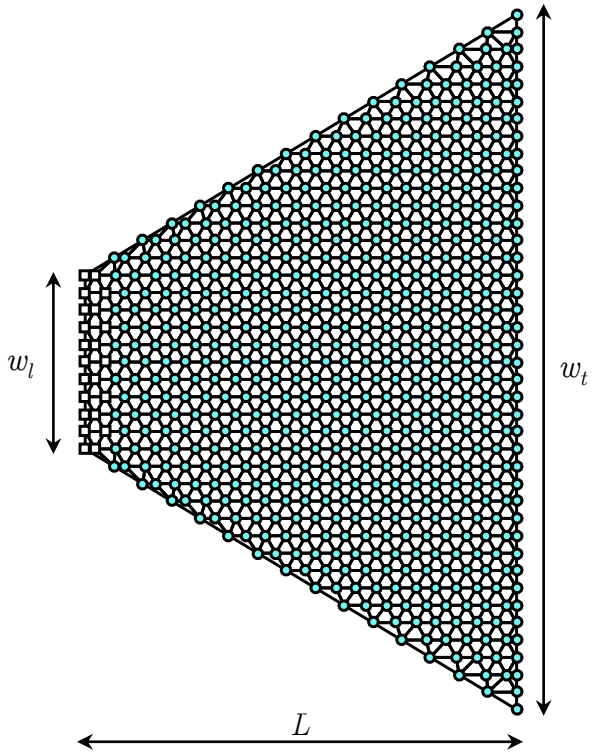

Figure 6: LSM model of trapezoidal shaped swimmer. Here, the width ratio is $w_R = w_l/w_t = 0.25$. Open squares indicate prescribed nodes, while filled circles represent passive mass nodes.

2.2.3 Tapered Thickness

For a tapered plate, the thickness of the plate starts at b_l at the leading edge and decreases linearly to a thickness of b_t at the trailing edge. Despite the changing thickness, we assume that $b(x) \ll L$ on the entire swimmer surface so the swimmer can be modeled as a two-dimensional plate. We can represent the plate thickness $b(x)$ mathematically as it varies linearly from the thickest portion near the LE at $x = 0$ to the thinnest portion at the TE at $x = L$:

$$b(x) = \bar{b}\frac{2}{a+1}\left[a - (a-1)\,\frac{x}{L}\right]. \tag{28}$$

Here, $\bar{b}$ is the plate's average thickness and a is the taper ratio, defined as $a = b_l/b_t$, the ratio of the LE thickness to the TE thickness. The same lattice structure as a plate with uniform thickness is used to represent the tapered plate, but the softening effect of the tapering is modeled by imposing equivalent stiffness and mass gradients with $k_b = k_b(x)$ and $m = m(x)$. For a high aspect ratio plate modeled by a triangular lattice as we use, the 1D bending rigidity $EI(x)$ is proportional to the bending stiffness $k_b(x)$ as shown:

$$EI(x) = \frac{Eb(x)^3 w}{12} = \frac{3\sqrt{3}}{4}k_b(x)w(1-\nu^2). \tag{29}$$

For plates with lower aspect ratios, the plate bending rigidity $D(x)$ is given by

$$D(x) = \frac{Eb(x)^3}{12(1-\nu^2)} = \frac{3\sqrt{3}}{4}k_b(x). \tag{30}$$

In each case, $k_b(x) \sim b(x)^3$; therefore, a tapered swimmer has a cubically varying bending stiffness. The tapered thickness also leads to a linear gradient of the mass per area $\sigma = \sigma(x)$:

$$\sigma(x) = \rho_s b(x). \tag{31}$$

In our LSM model, we use equations (28)–(31) to compute the nodal values of the mass and bending stiffness based on the initial distance away from the LE. Note that k_s has little effect on bending and is again set to a high enough value that

the plate is nearly inextensible during the swimming stroke. Therefore, we mimic the bending behavior of a tapered plate by imposing equivalent mass and bending stiffness gradients.

2.2.4 Plate with Internal Actuation

Here, we describe the LSM model of a swimmer with internal actuation instead of a plunging actuation at the leading edge. The swimmer is modeled as an elastic plate and uses the same lattice structure as described in section 2.2.1 with the addition of external forces on interior nodes for actuation. Figure 7 illustrates the LSM model. The plate is segmented into two sections. First, an internally actuated section, called the active portion (depicted with darker circles), extends a distance d from the leading edge. Beyond that, a passively responding tail section (the passive portion, lighter circles) is attached. The division between active and passive sections is indicated by the dotted line. On the leading edge (left), the open squares indicate nodes that are prescribed to be fixed in the vertical direction, so $\mathbf{R}_{LE,i} = \mathbf{R}_{LE,i}(0)$ (see section 2.2.1 for description of LE prescribed nodes). Having two fixed rows leads to a zero slope boundary condition. Both sections have the same isotropic material properties, so the mass and bending stiffness at each node in both sections are the same. The active portion actuates the swimmer using an internal moment, M, uniformly distributed within the active portion.

In order to model an internal bending moment within the LSM framework, we apply forces judiciously to bending units parallel to the x–direction within the active section. Figure 7b illustrates the appropriate distribution of the forces on a single bending unit. As shown, a bending unit is composed of three nodes, i_{-1}, i_0, and i_{+1}. The distance between nodes is given by $r_{\pm1,0} = |\mathbf{r}_{\pm1,0}|$, where $\mathbf{r}_{\pm1,0} = \mathbf{r}_{\pm1} - \mathbf{r}_0$ is the difference between the nodal position vectors. We apply the bending forces to nodes i_{+1} and i_{-1} in the direction perpendicular to both $\mathbf{r}_{\pm1,0}$ and $\hat{\mathbf{y}}$, which is the direction

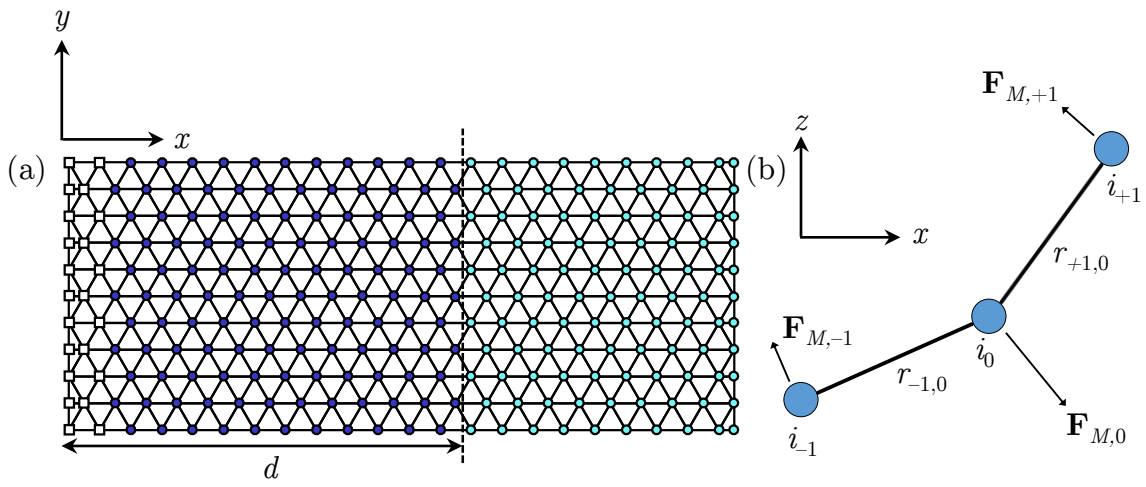

Figure 7: (a) Lattice spring model (LSM) triangular lattice of flexible plate. Open squares indicate nodes at the boundary that are restricted in the vertical direction. Darker and lighter circles indicate mass nodes in the active and passive portions, respectively. (b) Distribution of external forces on single bending unit to model a local couple at the center node.

of the imposed internal moment (into the page). We emphasize that the bending units concerned are only the ones parallel to the x–direction. The force directions can be computed by the following:

$$\mathbf{n}_{\pm1,0} = \pm\frac{\mathbf{r}_{\pm1,0}}{r_{\pm1,0}} \times \hat{\mathbf{y}}. \tag{32}$$

Using this procedure, a positive bending moment will lead to positive curvature in the xz–plane, presupposing that the entire bending unit does not rotate entirely around so that node i_{-1} and i_{+1} have switched positions. The bending nodal forces are thus given by

$$\mathbf{F}_{M,\pm1} = \frac{1}{N_r}\frac{M}{r_{\pm1,0}}\mathbf{n}_{\pm1,0}, \tag{33}$$

$$\mathbf{F}_{M,0} = -\left(\mathbf{F}_{M,-1} + \mathbf{F}_{M,+1}\right). \tag{34}$$

Here, N_r is the number of horizontal rows in the LSM lattice. The opposite force on node i_0 ensures that the total bending force on a bending unit is zero, representing a local couple at i_0. These bending forces are applied to all bending units within the active region.

2.3 Model Validation

Though the hybrid LBM and LSM model has been extensively validated and used to study a variety of phenomena [84, 100, 106–115], we show several validation cases to demonstrate that the FSI solver with the LSM models could accurately model the physics of an oscillating swimmer. We demonstrate that the coupling procedure yields the correct forcing by computing the lift and drag on a rigid plate undergoing an insect-like motion and comparing the results to previous computational and experimental work. Then we demonstrate that the LSM models as described in the previous section can accurately capture the respective bending physics.

2.3.1 Lift and Drag on Plate Undergoing Insect-like Hovering Stroke

Wang, Birch, and Dickinson [117] used numerical simulations and experiments to study the lift and drag on a simple insect wing model. Here, the insect wing, represented as a rigid bar in a 2D fluid field, undergoes an a combined rotational and translational motion about its midpoint. The kinematics correspond to a simplified approximation of live insect wing flapping. Specifically, the kinematics equations are given by

$$x(t) = \frac{A_0}{2}\cos(2\pi f t), \tag{35}$$

$$\alpha(t) = \alpha_0 + \beta \sin(2\pi f t + \phi), \tag{36}$$

where $x(t)$ is the center position and $\alpha(t)$ is the orientation with respect to the horizontal axis. In this particular validation case, we set $A_0/c = 2.8$, $\alpha_0 = \pi/2$, $\beta = \pi/4$, and $\phi = 0$, where c is the wing chord (length of the bar). Frequency f and kinematic viscosity ν are set such that the Reynolds number $Re = \pi f A_0 c/\nu = 75$. For our three-dimensional solver, we place the LSM solid in a way that the edges are slightly past the fluid boundaries, thus modeling a two-dimensional flow. We perform the simulations for 30 periods, which is long enough that the forces reach steady state.

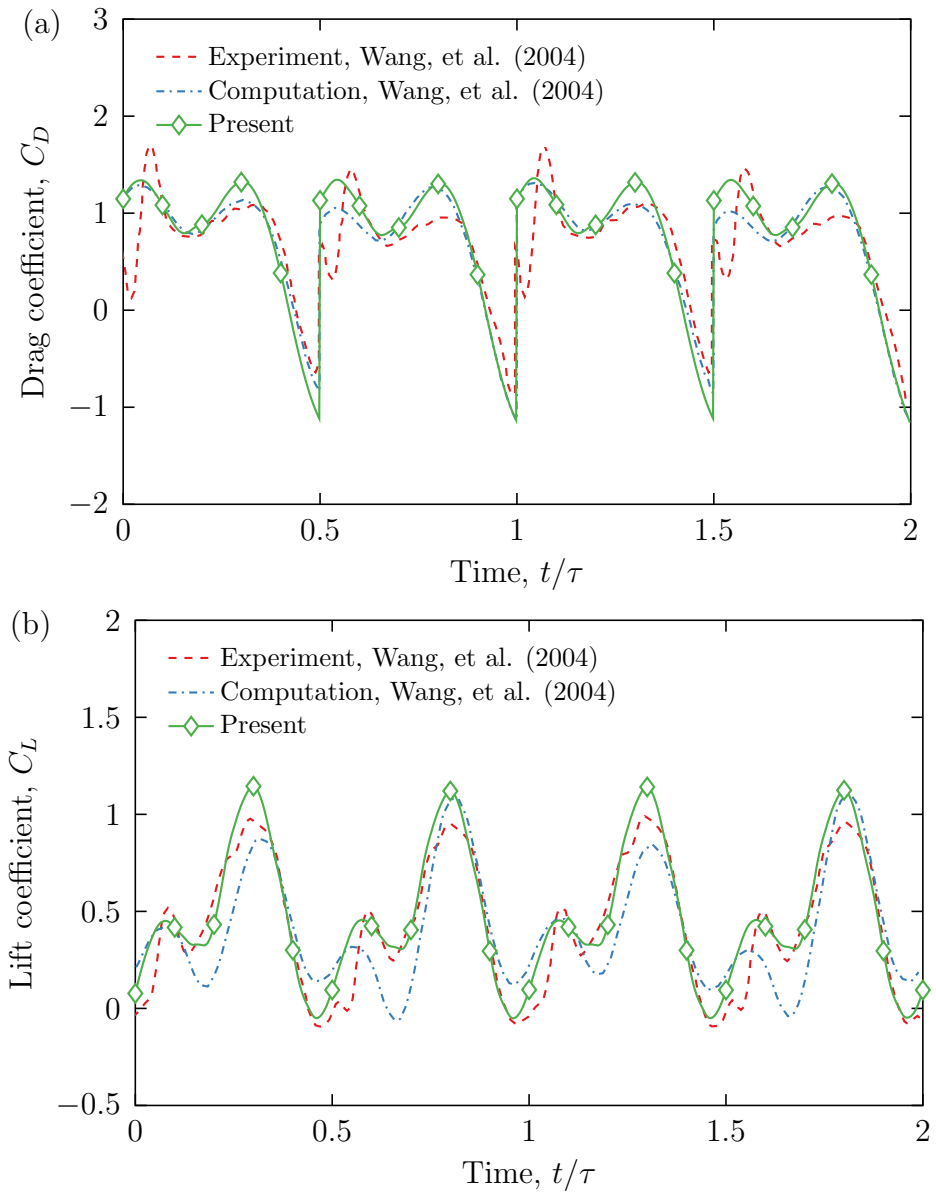

Figure 8: Drag and lift coefficients for plate undergoing insect-like hovering stroke. Present results show agreement to previous experimental and computational work [117].

Figure 8 shows the lift and drag time histories of the wing. Both the lift and drag were normalized by the maximum quasi-steady force [117]. We find good agreement to both the experimental and computational data. Discrepancies may be attributed to transient effects in the previous computational data. The previous numerical simulations were able only to calculate the first three periods of the wing starting from

the initial quiescent state, whereas our method can readily simulate the plate motion at later times after the transient effects become negligible. Furthermore, the experimental data has three-dimensional effects, which we have not captured in this 2D validation model.

2.3.2 Tapered Plate Deflection

We validate the LSM model for a tapered plate by comparing the static deflection of an end-loaded plate cantilever to the corresponding theoretical solution. We consider taper ratios $a = 1, 2, 5, 10$, thus validating the uniform plate deflection as well. Because the plate is thin, slender, and bends primarily in one plane, it behaves similarly to an Euler-Bernoulli beam. For relatively large deformations and assuming an inextensible beam, the non-dimensional governing equation may be derived from the moment-curvature relationship and is given by the following [118]:

$$\frac{d}{ds}\left[f(s)\frac{d\theta}{ds}\right] = -\alpha\cos\theta. \tag{37}$$

Here, s is the arc length coordinate normalized by beam length, θ is the local angle relative to the horizontal, $f(s) = EI(s)/\overline{EI}$ is a non-dimensional tapering factor for bending rigidity, $\overline{EI}$ is the average bending rigidity, and $\alpha = PL^2/\overline{EI}$ is the non-dimensional load at the free end (P is the force at the free end). Two other equations are necessary to determine the deflection shape:

$$\frac{dx}{ds} = \cos\theta, \quad \frac{dz}{ds} = \sin\theta, \tag{38}$$

where $x(s)$ and $z(s)$ are the horizontal and vertical non-dimensional coordinates that define the position of the beam. Boundary conditions for the cantilever beam are

$$\theta(0) = 0, \quad \theta'(1) = 0, \quad x(0) = 0, \quad z(0) = 0. \tag{39}$$

The boundary value problem posed by equations (37)–(39) is solved using the fourth-order accurate `bvp4c` function in MATLAB [119]. The beam solution is compared to the solution from LSM as shown in Figure 9 for $\alpha = 1$.

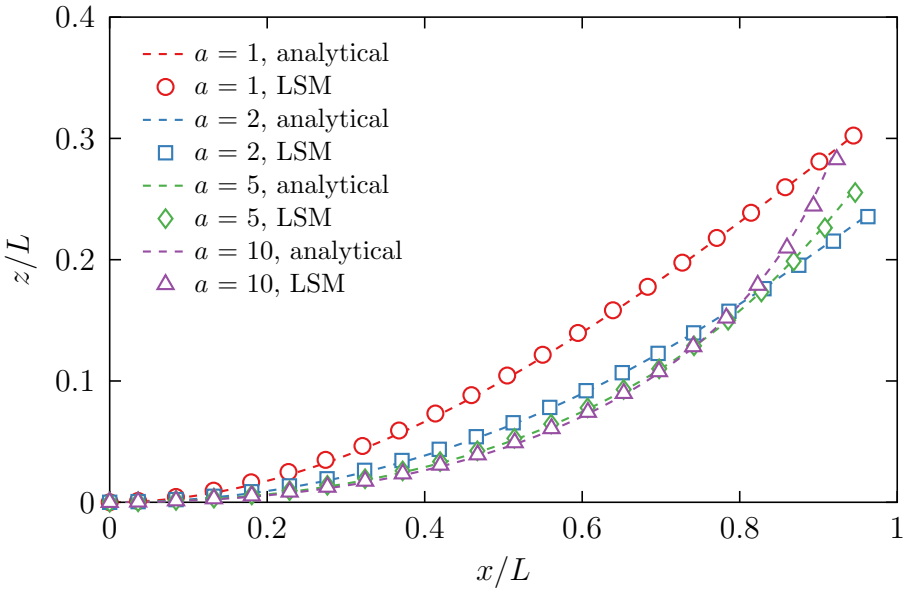

Figure 9: Static deflection of tapered swimmer. The LSM model predicts deflection that agrees well with the analytical solutions for different taper ratios even with large tip deflections.

We find good agreement between the LSM solution and the analytical model even with large tip deflections exceeding 30%. With increasing taper ratio a, we observe a larger curvature in the static deflection shape, although the tip deflection for the uniformly thick plate has the largest deflection for this specific end loading. Thus, we have confidence that the LSM model would accurately simulate the physical behavior of both uniform and tapered plates undergoing large deformations.

2.3.3 Internally Actuated Plate Deflection

In order to validate our LSM model with moment actuation, we calculate the static deflection of the internally actuated plate under the application of a constant moment. We consider a cantilevered plate with active and passive sections. In this case the plate bending deformation is in one dimension and can be modeled by the moment-curvature relationship for beam bending. Mathematically, the curvature $\kappa(s)$ along

the plate length in terms of the arc length coordinate s is expressed as

$$\begin{cases} \kappa(s) = M/EI, & 0 \leq s < d \\ \kappa(s) = 0, & d \leq s \leq L \end{cases} \tag{40}$$

In these expressions, M is a constant moment that is applied on the active section for a length d, and EI is the 1D bending rigidity. The equation states that the curvature is constant within the active section, while it is zero in the passive section — the deformation extends in a straight line. The plate deformation curve $z(x)$ can be expressed parametrically as follows:

$$z(s) = \begin{cases} R - R\cos(s/R) = M/EI, & 0 \leq s \leq d \\ z(d) + \sin(d/R)(s-d), & d < s \leq L \end{cases} \tag{41}$$

$$x(s) = \begin{cases} R - R\sin(s/R) = M/EI, & 0 \leq s \leq d \\ x(d) + \cos(d/R)(s-d), & d < s \leq L \end{cases} \tag{42}$$

Here, $R = EI/M$ is the radius of curvature.

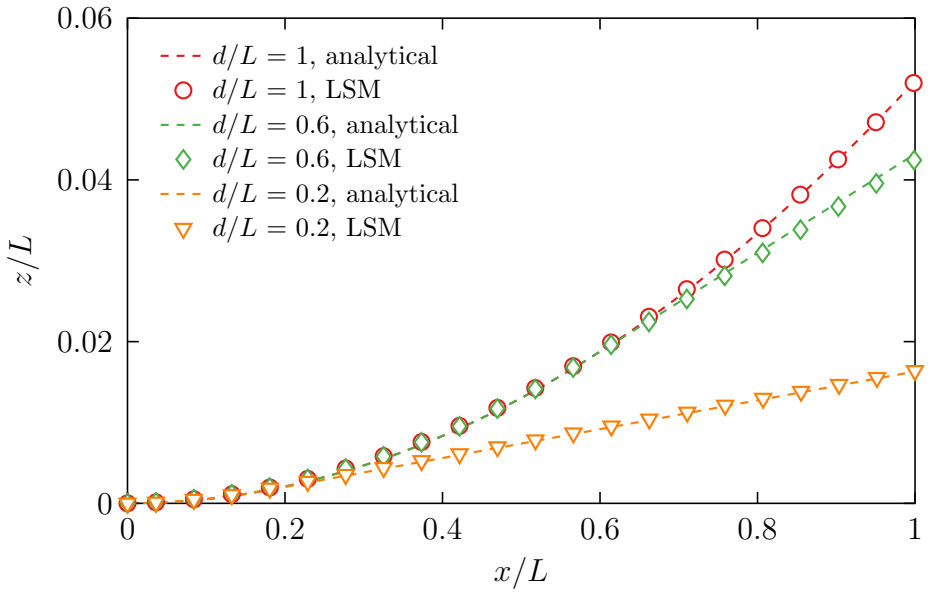

Figure 10: Static deflection of an internally actuated plate with active and passive sections. Symbols represent LSM simulations, while lines represent the analytical solution. Good agreement is found between simulations and theory.

We use our LSM with internal actuation model as described in section 1.2.4 to compute the deformation for $R/L = 9.6$ and d/L values of 0.2, 0.6, and 1. These bending curves are shown in Figure 10 with symbols. As shown, the plate maintains constant curvature with its slope increasing until the active-passive boundary at $x = x(d) \approx d$. In the passive section, the plate deformation continues in a straight line until its free end. Consequently, the plate with the largest active section exhibits the largest deflection.

Our results are compared to the analytical solution, depicted using the straight and dotted lines as shown in Figure 10. We find good agreement between the LSM results and the analytical solution, differing by no more than 2%, which is related to the grid resolution of our LSM model. Therefore, the LSM moment actuation model accurately captures the beam bending behavior.

2.3.4 Trapezoidal Plate Deflection

Finally, we validate our trapezoidal plate LSM model by computing the static deflection field of a cantilevered plate and comparing the LSM solution to a finite element solution using ANSYS Mechanical. For this case, we consider cantilever plate which is clamped at one end, undergoing a distributed vertical load q at the free end. The plate has bending rigidity D, length ratio $w_l/w_t = 0.25$, and aspect ratio $L/w_l = 2.5$. In our ANSYS simulation, we use a quadrilateral mesh of 201×201 `SHELL181` elements and compute the solution using linear theory.

In Figures 11a and 11b, we plot contours of the non-dimensional deflection zD/qL^4 for the LSM solution and the ANSYS solution. Qualitatively, we find good agreement, as the LSM simulation also captures the larger deflection at the corners compared to the center-line deflection as predicted by the ANSYS solution. Figure 11c depicts the centerline deflection for both the LSM and ANSYS solution. This graph confirms the good agreement, with the solutions differing by less than 2%. Despite the linear

theory used here, we have shown in the previous validation studies that the LSM model can accurately capture large deformations, so we have confidence in our LSM model for trapezoidal swimmers.

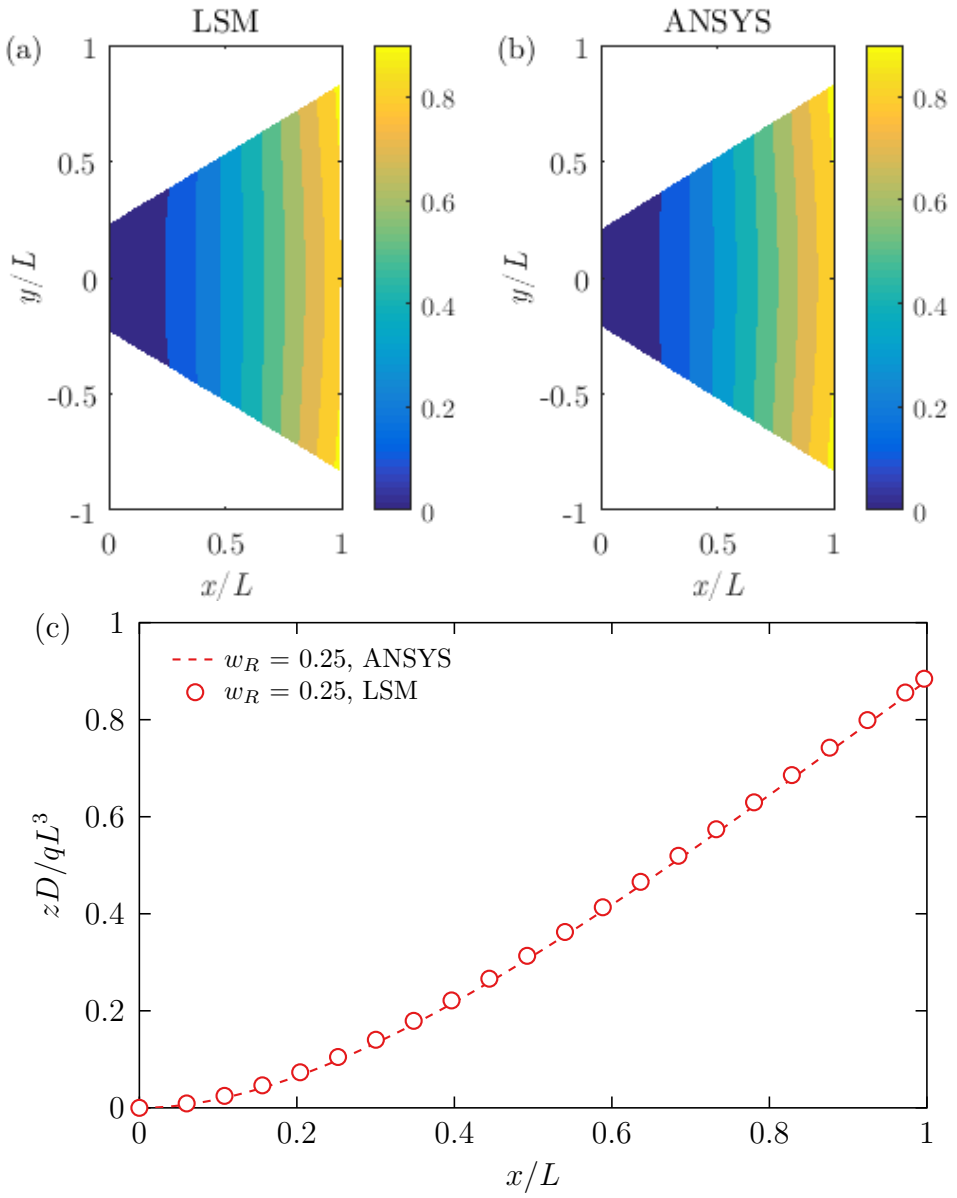

Figure 11: Contours of deflection of trapezoidal plate with width ratio $w_R = 0.25$ corresponding to (a) LSM model and (b) ANSYS finite element solution. Both the ANSYS and LSM contour plots show qualitatively very good agreement, and the centerline plot in (c) confirms this.

2.4 System Parameters

In this section we specify the computational parameters that characterize the system and discuss the appropriate quantities that define the swimming performance. In all of our studies, we actuate the swimmer with a constant stroke period $\tau = 2000$ LBM units, so the constant driving frequency is $\omega = \tau/2\pi$. For free swimming studies we run the simulation for 50 periods so that the swimmer reaches a periodic steady-state velocity. For studies in which the plate leading edge is constrained, simulations were performed for 30 periods. The swimmer is submerged entirely in an incompressible Newtonian fluid with dynamic viscosity $\mu = \pi/1000$ and density $\rho = 1$. For leading edge sinusoidal actuation with constant amplitude $A_0 = 5$, this leads to a definition of the Reynolds number $\mathrm{Re} = \rho\omega A_0 L/\mu = 250$. In addition, the swimmer bending dynamics depends on the mass ratio between the solid and fluid, $T = \rho L/\rho_s b$, where ρ_s is the density of the solid swimmer. For wider swimmers with low AR, T characterizes the added mass of the fluid displaced by the swimmer, however for narrow swimmers the added mass can be estimated as T/AR.

Swimmer deformation is strongly affected by the swimmer bending rigidity EI (D for wider plates). In a structural vibration system, the deformation is dictated by the system's proximity to its natural frequencies. The first natural frequency ω_1 occurs when the phase between the swimmer relative deflection — absolute trailing edge displacement minus the leading edge displacement — and leading edge displacement is 90 degrees. When damping is sufficiently small, oscillations are amplified the most when $\omega \approx \omega_1$; i.e. the system is driven near its first natural frequency. Note that for damped systems this frequency is close to, but does not coincide with the practical resonant frequency, at which the swimmer relative deflection is maximized [120]. Since we apply a constant driving frequency in our simulations, we vary the bending rigidity to probe the swimming performance near the first natural frequency. Note that the first natural frequency of the swimmer submerged in the fluid is substantially different

from that in vacuum [91]. Moreover, the natural frequency in fluid depends on the plate geometry and mass ratio.

In our studies we use two different ways to quantify the proximity to the first natural frequency in fluid, $\omega_{1,f}$. For high aspect ratio, isotropic swimmers, such as the ones considered in Chapters 3, 6, and 7 with $AR = 2.5$, $\omega_{1,f}$ can be estimated based on a solution from linear theory [91]:

$$\omega_{1,f} = \frac{\lambda_1^2}{L^2}\sqrt{\frac{EI}{\rho_s b w}}\left(1 + \frac{\pi\rho w}{4\rho_s b}\Gamma\right). \tag{43}$$

Here, $\lambda_1 \approx 1.875$ is the smallest root satisfying $1 + \cos\lambda\cosh\lambda = 0$ and Γ is the hydrodynamic function, whose values depend on aspect ratio and recursively on $\omega_{1,f}$. The values of Γ can be found in the work detailing this linear theory [91]. We define the frequency ratio $\phi = \omega/\omega_{1,f}$ to quantify the bending response based on proximity to the first natural frequency. In order to vary ϕ and keep ω constant, we vary $\omega_{1,f}$ by changing bending rigidity EI.

For our studies in which the linear theory cannot be applied, such as wider swimmers and swimmers with tapered thickness, we use simulations to directly compute the bending rigidity, EI_0, that leads to the first natural frequency for the constant value of ω used in this study. We define a quantity $r = (EI/EI_0)^{-0.5}$ to characterize the swimmer's vibration response proximity to its first natural frequency. To first order, this quantity approximates the frequency ratio, i.e. $r \approx \omega/\omega_{1,f}$ and exactly represents the first natural frequency when $r = 1$. Therefore, we refer to r as the frequency ratio for the cases in which ϕ does not apply.

We characterize the performance of our elastic plunging swimmer by its dimensionless period-averaged steady state swimming velocity, U/U_0, and power consumption, P/P_0. Here, U is the dimensional velocity, and P is the dimensional period-averaged input power required to maintain the swimming. The characteristic velocity is $U_0 = L/\tau$, in which case the dimensionless velocity U/U_0 represents the number of body lengths traveled per period. The input power is defined to be the average

external work done per period to actuate the swimmer, and we normalize the input power by $P_0 = 0.5\rho U_0^3 wL$, which represents the characteristic power of the system. Note that for swimmers with different widths, P_0 is a function of width, so P/P_0 is a dimensionless power per unit width.

A typical measure of swimming efficiency in studies of propulsion is the Froude efficiency [59], given by $F_T U/P$, where F_T is the thrust. In free swimming, however, the net period-averaged hydrodynamic force is zero, and the separate contributions of thrust and drag are ill-defined. Therefore, to characterize the energy cost of motion, we introduce the swimming economy $\varepsilon = (U/U_0)/(P/P_0)$, the ratio between the dimensionless swimming velocity and dimensionless input power. The quantity ε is related to the inverse of the swimming energy cost, often used to characterize the aquatic propulsion of biological systems [121, 122]. In other words, for a constant frequency of actuation, ε characterizes the distance traveled by the swimmer per unit input work. The higher the swimming economy, the longer distance the swimmer travels using the same amount of work.

CHAPTER III

FREE SWIMMING OF PLUNGING FLEXIBLE PLATE

3.1 Introduction and Computational Setup

In this chapter, we establish a baseline understanding of the physics of an oscillating flexible plate undergoing free swimming. This oscillating flexible plate, which will be referred to as a swimmer in this chapter, represents a simplified physical model of a biomimetic flexible fin propulsor. We investigate the hydrodynamics and deformation of the swimmer when it experiences zero net time-averaged propulsion and simply cruises forward. We calculate the swimmer velocity, consumed power, and swimming economy to characterize different swimming regimes and probe how these regimes depend on swimmer bending pattern. We show that the swimming velocity is maximized when the actuation frequency is near the swimmer's first natural frequency in fluid, and that the swimming economy is maximized away from resonance. These two regimes of maximum velocity and economy are associated with specific bending patterns, and we explain the underlying physical mechanisms.

The details of the computational model are given in Chapter 2 so we briefly discuss the model parameters here. Our swimmer has length L and width w with aspect ratio $AR = L/w = 2.5$. The thickness, $b \ll L$, is small compared to the length, so we consider the swimmer to be effectively an infinitely thin plate. As shown in Figure 12, the swimmer leading edge undergoes a plunging motion with sinusoidal displacement given by $A(t) = A_0 \cos(\omega t)$, where $A_0 = 0.1L$ is the oscillation amplitude, ω is the driving angular frequency, and t is time. Additionally, we set a zero slope boundary condition at the swimmer leading edge. The Reynolds number $\mathrm{Re} = \rho\omega A_0 L/\mu = 250$, which is relevant to the swimming of relatively small swimmers ($\sim$cm) moving at low

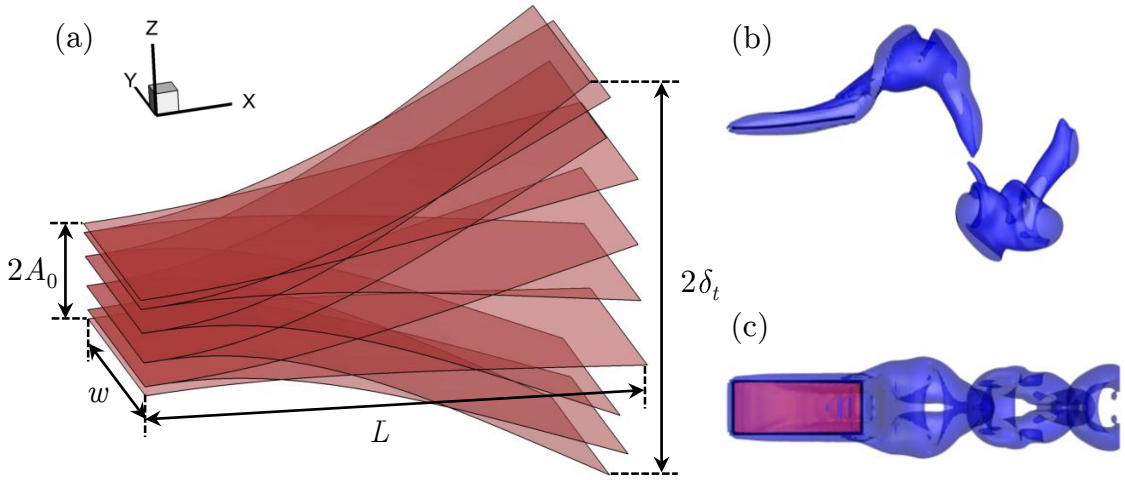

Figure 12: (a) Schematic of elastic swimmer. The swimmer has width w, length L, and is actuated sinusoidally at the leading edge with displacement $A(t) = A_0 \cos(\omega t)$. The trailing edge displacement amplitude is denoted by δ_t. Overlaid are instantaneous snapshots of the swimmer's bending shape while in motion. (b) Side view and (c) top view of the swimmer in motion (dark outline) with vortex structures in its wake.

speeds (∼cm/s). In this flow regime, both viscous and inertial effects are important.

3.2 Results and Discussion

3.2.1 Performance Characterization

First, we investigate how the swimming velocity changes as a function of bending pattern and added mass T. In Figure 13a we show the dimensionless forward swimming velocity U as a function of the frequency ratio ϕ, which quantifies the bending pattern (see Chapter 2). We find that swimming velocity is maximized at $\phi_{MV} \approx 1.1$ that is close to the natural frequency, and this optimal frequency is nearly independent of the swimmer added mass T. Away from the natural frequency, the swimming velocity is considerably lower with a speed that is several times slower than that at ϕ_{MV}. This suggests that driving at the natural frequency leads to a bending pattern that strongly influences the swimmer hydrodynamics and results in higher speeds. At ϕ_{MV}, we find that heavier swimmers characterized by a smaller added mass swim faster than lighter swimmers; i.e., the maximum velocity decreases with increasing

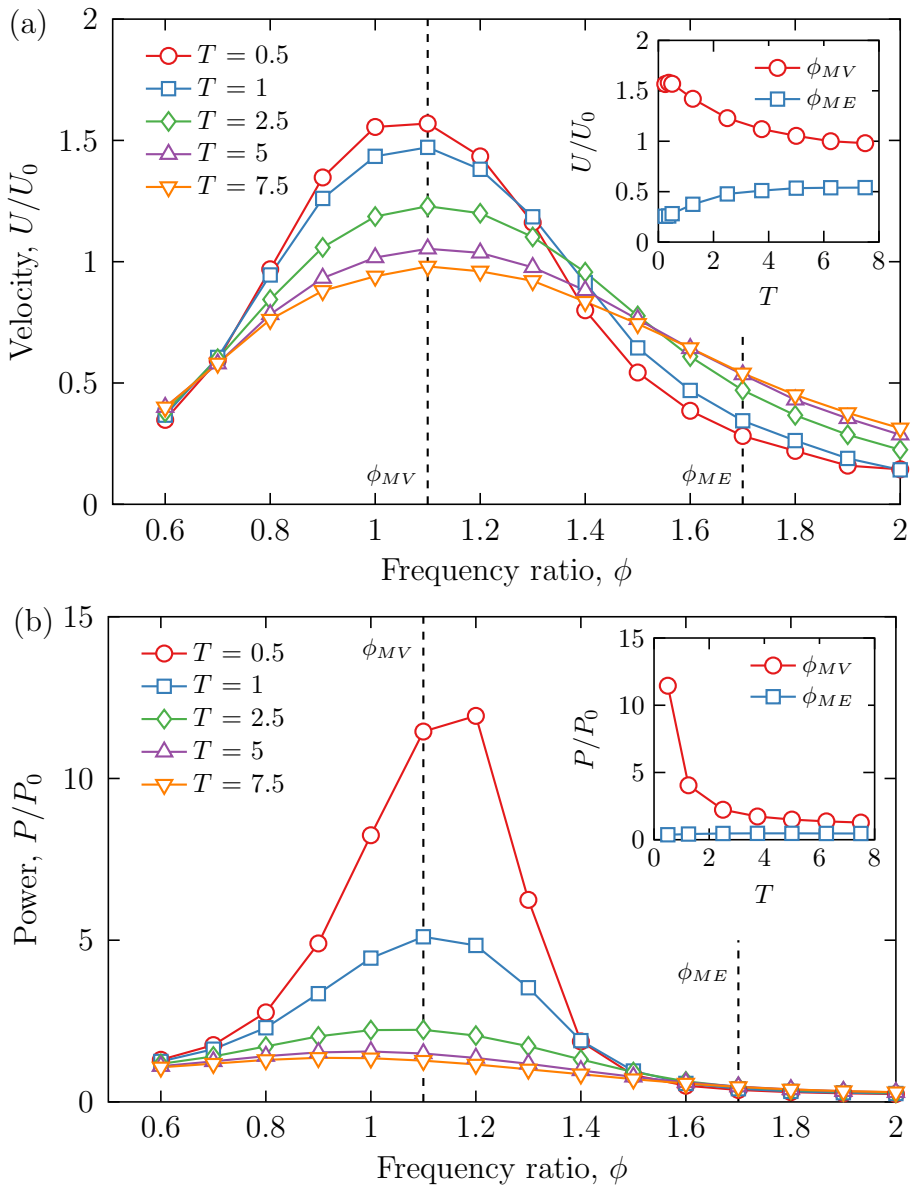

Figure 13: (a) Steady state forward swimming velocity and (b) input power as functions of driving frequency ratio for elastic swimmers with Re = 250, $AR = 2.5$, and different values of added mass T. Swimming velocity peaks near the natural frequency at $\phi_{MV} \approx 1.1$, independent of added mass. However, swimming at this frequency requires higher input power, particularly for swimmers with smaller added mass.

added mass. It is interesting that for post-resonance frequencies, this trend reverses, and for $\phi > 1.4$, lighter swimmers with larger T exhibit faster swimming speeds.

The non-dimensional input power required to sustain the swimmer motion, P/P_0, is shown in Figure 13b as a function of frequency ratio r. Similar to swimming velocity,

the input power for different added mass values is maximized at frequencies close to ϕ_{MV}. The increase in input power is most significant for the heaviest swimmers. For example, when T decreases from 1 to 0.5, the input power is increased about 2.5 times.

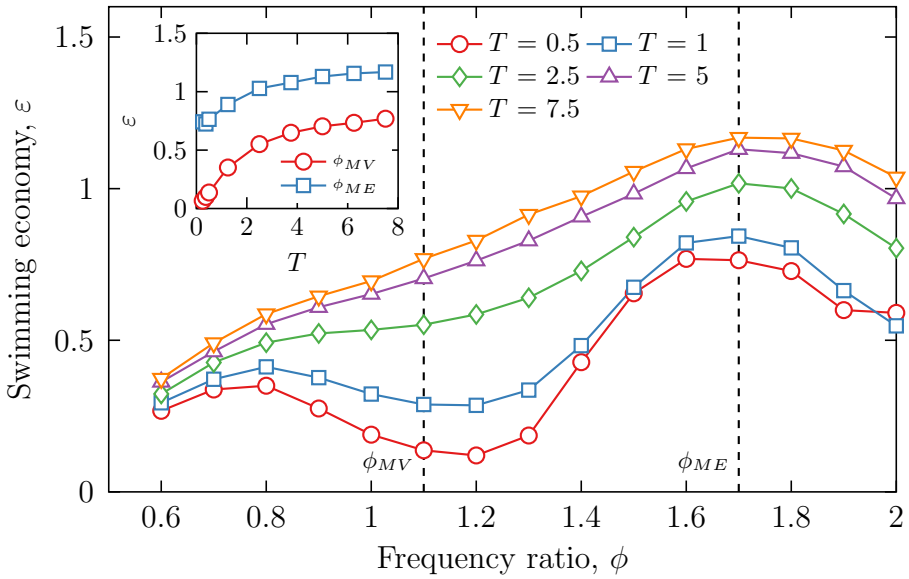

Figure 14: Swimming economy as a function of driving frequency ratio for elastic swimmers with Re = 250, $AR = 2.5$, and different values of added mass T. Economy is highest off resonance at $\phi_{ME} \approx 1.7$. Swimming near the natural frequency results in low economy, particularly for heavier swimmers.

To quantify how efficiently the swimmers translate the input power into the forward swimming velocity, we calculate the swimming economy ε (Figure 14). This parameter characterizes the ratio between the dimensionless swimming velocity and input power. Higher values of ε mean that the swimmer can move more quickly with the same amount of input power. We find that for any oscillation frequency, heavier swimmers exhibit lower swimming economy compared to lighter swimmers. Near the first natural frequency, the swimmer economy is suboptimal and furthermore, heavier swimmers with $T \leq 1$ exhibit a local minimum. This minimum is related to the large increase in input power required to drive heavier swimmers at the natural frequency (Figure 13b). Furthermore, we find that the swimming economy is maximized in each

case at a frequency near $\phi_{ME} \approx 1.7$ (see Figure 14) that is nearly independent of the added mass. Note that at the frequency of the maximum economy, the swimming speed is a few times lower than the respective maxima.

We characterize the swimmer's bending response in terms of the amplitude of its vertical displacement. Figure 15 shows, respectively, the displacements of the swimmer's trailing edge, δ_t, and of the centroid (same as the center of mass), δ_c, as a function of frequency ratio. We normalize these displacements by the leading edge amplitude, A_0. At frequencies close to the natural frequency, both these characteristics follow a trend that is similar to that of forward velocity for all values of added mass. Both displacements are maximized slightly above the natural frequency.

For post-resonance frequencies, however, the trailing edge and centroid displacements exhibit distinct behavior. For frequencies $\phi > 1.5$, the trailing edge displacement curves nearly overlap and slightly decrease with ϕ, indicating that at these frequencies, the trailing edge displacement is independent of the added mass. On the other hand, the vertical displacement of swimmer's centroid decreases more rapidly for $\phi > 1.4$. The decrease is the most significant for heavier swimmers with smaller T. Furthermore, the curves for swimmers with $T \leq 1$ exhibit a minimum at $\phi = 1.7$, where the centroid displacement approaches zero. This corresponds closely to the frequency of maximum economy, ϕ_{ME}. As we will discuss in the next section, the smaller displacement of the swimmer's centroid is directly related to higher swimming economy.

Thus, we find two distinct swimming regimes characterized by high velocity and high economy. We denote these two regimes by MV (maximum velocity) and ME (maximum economy), respectively. To swim fast, the swimmer should be actuated at ϕ_{MV} found near the natural frequency. To swim with high economy, the actuation should be performed away from the resonance at a frequency about ϕ_{ME}. In addition, we find that the trailing edge displacement is maximized near the frequency of the

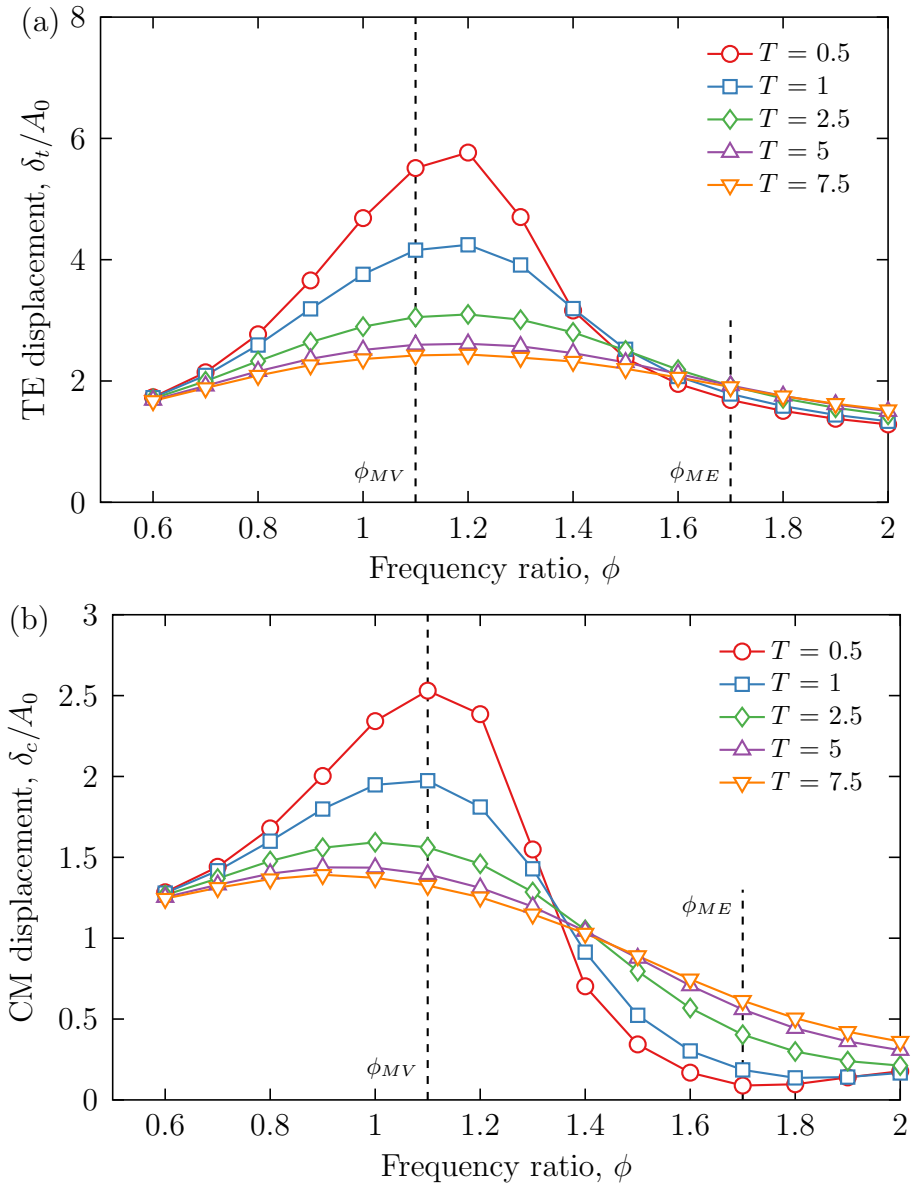

Figure 15: (a) Trailing edge displacement and (b) center of mass (CM) displacement as functions of frequency ratio for elastic swimmers with Re = 250, $AR = 2.5$, and different values of added mass T. Both displacements are maximized near the natural frequency. Near ϕ_{ME}, the CM displacement has a minimum for lower T.

high velocity regime, and the centroid displacement is minimized near the frequency of the high economy regime. To gain insight in these two regimes, we examine the vortex structures, forces, and bending patterns.

3.2.2 Vortex Structures and Bending Patterns

Figure 16 illustrates vortex structures generated by swimmers with $T = 1$ oscillating at the MV and ME regimes, respectively. In these figures, the semitransparent surfaces represent the vorticity of a constant magnitude. Figure 16a shows that the swimmer at MV generates both trailing edge vortices (TEV) and side edge vortices (SEV). As seen in the figure, the SEV extend along the side edges of the swimmer. The vortices periodically detach from the swimmer trailing edge, and the combination of the TEV and SEV forms a horseshoe-shaped topology of the shed vortices in the wake. This vortex structure is consistent with previous experimental and numerical observations [67, 68, 77].

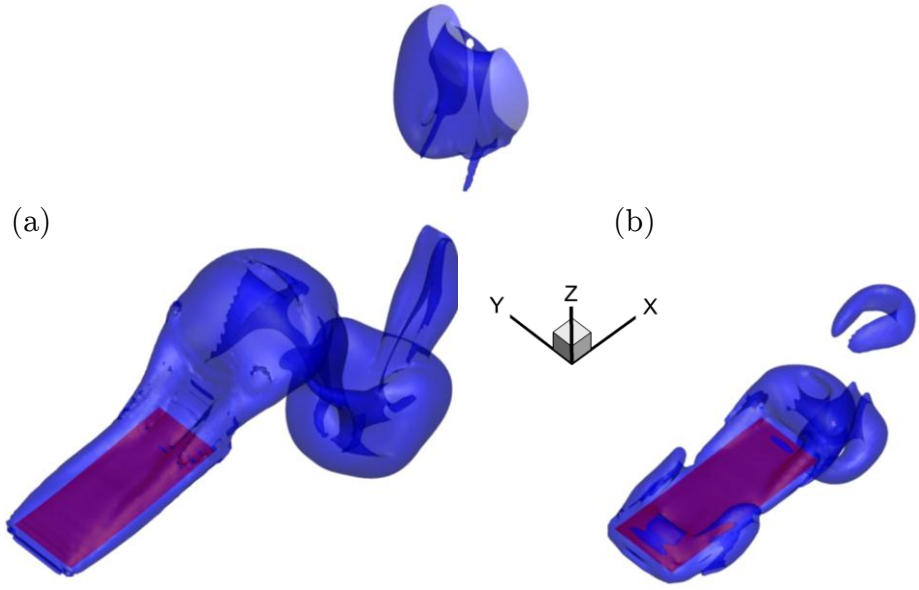

Figure 16: Flow structures generated by elastic swimmers with $T = 1$, Re $= 250$, $AR = 2.5$ driven at (a) the maximum velocity frequency $\phi_{MV} = 1.1$ and (b) at the maximum economy frequency $\phi_{ME} = 1.7$. The semi-transparent surfaces illustrate vorticity surfaces of constant magnitude $\psi = 4$.

In Figure 16b, we show the vorticity magnitude surfaces for the case of ME. These surfaces are plotted at the same scale as the one in Figure 16a. Similar to the MV regime, a swimmer at the ME regime generates both TEV and SEV, which are shed to

form horseshoe shaped structures in the wake. We find that compared to MV, vortices generated in the ME regime have a lower magnitude. More importantly, however, is that the swimmer at ME produces SEV that are disconnected approximately at the middle of the swimmer, whereas MV swimmers generate continuous SEV that extend along the entire swimmer length. In other words, at the ME regime there are two separate vortices along each of the swimmer sides, one at the front of the swimmer between the leading edge and the middle, and one at the back from the middle to the trailing edge.

Vorticity is generated by a relative motion between the swimmer and the fluid. Therefore, we examine the bending pattern of the swimmer in the two characteristic regimes of swimming. Figure 17 shows MV and ME swimmer profiles (in the xz–plane) at equally spaced points in time. The dotted lines represent the downstroke and the solid lines represent the upstroke. The swimmer profiles are plotted relative to the horizontal position of the leading edge. In MV, the envelope of the maximum displacement of the swimmer in the z–direction increases monotonically from the leading to the trailing edge. In contrast, in ME, we find that near the center of the swimmer its displacement is minimum.

The larger displacement of the swimmer at MV leads to a larger amount of fluid displaced normally relative to the swimmer surface. This fluid that is displaced from one side of the swimmer to another side during each stroke flows around the swimmer, thereby producing SEV that grow from the swimmer leading to trailing edge. In the ME regime the swimmer's bending pattern relative to the leading edge is characterized by a rotational motion about its centroid. This bending motion acts to reduce the amount of fluid that is transported around the side edges of the plunging swimmer. As the front section of the swimmer moves in the positive z–direction, the back section of the swimmer moves in the negative z–direction and *vice versa*. The opposite directions of the motion of the front and back ends allow the fluid to move

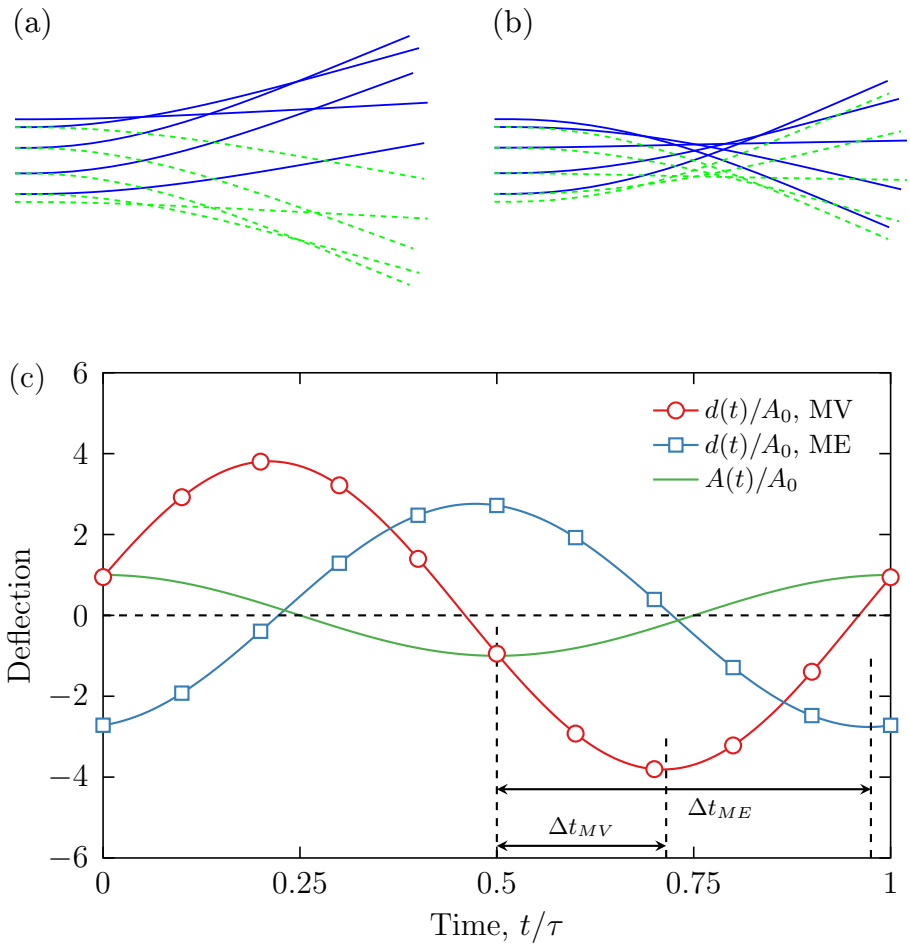

Figure 17: Bending patterns of elastic swimmers driven at (a) $\phi_{MV} = 1.1$ and (b) $\phi_{ME} = 1.7$. Each line represents an instantaneous swimmer profile. The profiles are shown at equal time intervals during one oscillation period. The solid lines depict the upstroke, while the dotted lines depict the downstroke profiles. (c) Leading edge displacement and swimmer deflection as functions of time during one period of swimmer oscillations. Swimmer parameters are $T = 1$, Re $= 250$, and $AR = 2.5$.

along the swimmer instead of being forced to flow around the side edges, which takes place in the MV case. This reduced amount of fluid transported around swimmer sides results in weaker side edge vortices disconnected around the non-oscillating swimmer center, thereby reducing the viscous dissipation associated with swimmer motion.

To further characterize the swimmer bending pattern, we examine the time dependence of the leading edge displacement and swimmer deflection shown in Figure 17c. The swimmer deflection is given by the difference between the trailing edge

and leading edge displacements, $d(t) = \delta_t(t) - A(t)$. The dotted lines represent the relative trailing edge displacements for MV and ME, while the solid line represents the imposed displacement at the leading edge. We find that the maximum deflection is larger in MV than in ME, and the phase between the deflection and leading edge displacement differs between these two cases. For MV, the phase lag is $\Delta\theta_{MV} = \omega\Delta t_{MV} \approx 0.42\pi$, which is slightly below $\pi/2$ corresponding to the natural frequency. In ME, we find the phase lag to be $\Delta\theta_{ME} = \omega\Delta t_{ME} \approx 0.94\pi$. The ME regime is therefore unrelated to the structural resonance of the swimmer. Furthermore, this large phase lag implies that the leading and trailing edges are moving nearly in antiphase. Thus, the leading and trailing edges displace vertically in opposite directions during most of the oscillation period, generating two different sets of side vortices that spin in opposite directions (see Figure 16b).

3.2.3 Comparison to Stationary Swimmer

In Figure 18a, we show the dependence of the phase difference $\Delta\theta$ between the leading edge displacement and deflection on the frequency ratio for a swimmer with $T = 1$. The curves show the data for a stationary swimmer, i.e. one whose leading edge is constrained horizontally, and a free-moving swimmer. We find that for the stationary swimmer the actual natural frequency $\phi_{1,\text{stat}}$ at which $\Delta\theta = \pi/2$ is within 5% from the value predicted by the Sader's theory [91]. For a free-moving swimmer, however, the natural frequency $\phi_{1,\text{swim}}$ is about 15% greater than the theoretical value, indicating that the natural frequency depends on the swimmer propulsion velocity. Note that the maximum deflection does not occur at the natural frequency for both stationary swimmers $\phi_{d,\text{stat}}$ and free-moving swimmers $\phi_{d,\text{swim}}$ (see the inset in Figure 18a), which is typical for oscillating systems with relatively high damping [120].

In Figure 18b, we plot frequencies corresponding to the swimmer fundamental natural frequency ϕ_1 and the maximum deflection (practical resonance) frequency ϕ_d

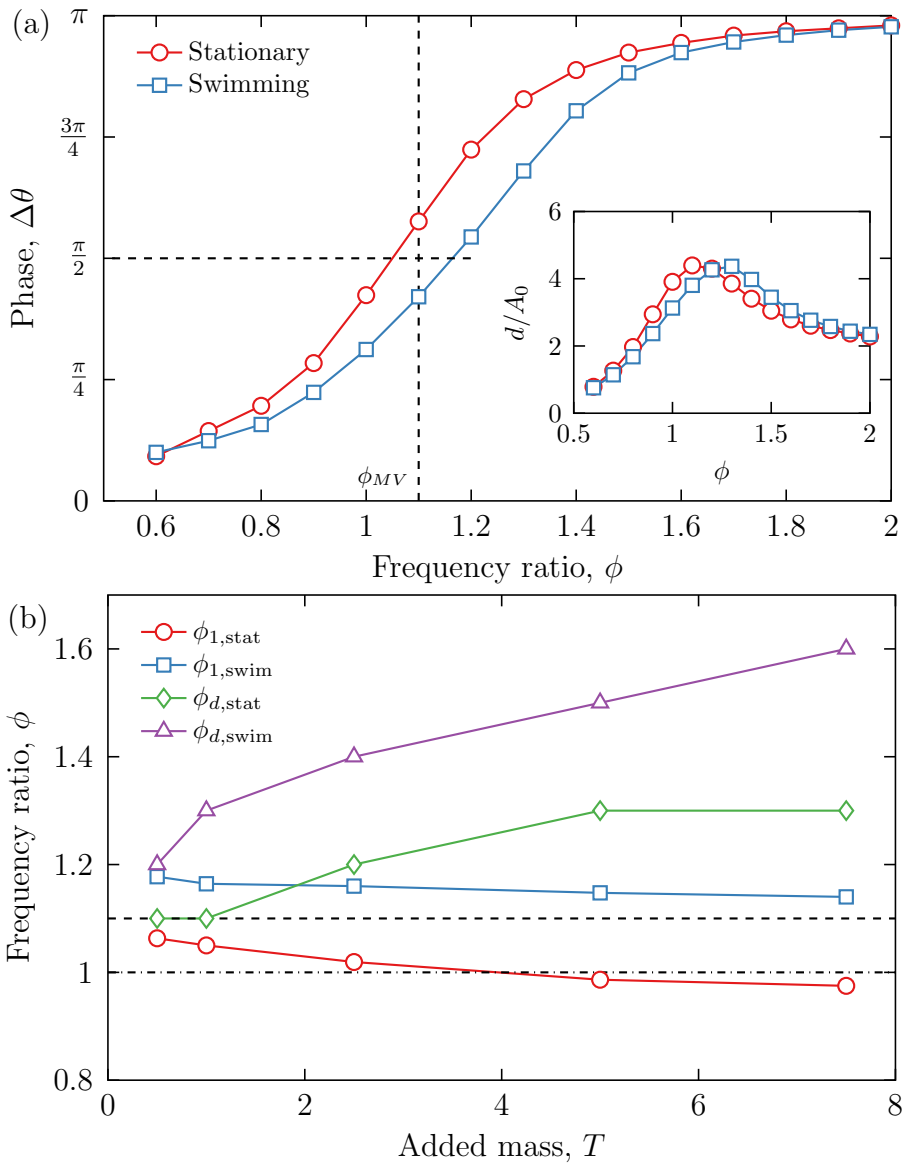

Figure 18: (a) Phase difference as a function of ϕ between leading edge displacement and swimmer deflection for stationary and moving swimmers with $T = 1$. The horizontal dotted line represents a phase of $\pi/2$ corresponding to swimmer natural frequency. (b) Natural frequencies and maximum deflection frequencies for stationary and moving swimmers as a function of added mass. The dotted line shows the frequency of maximum velocity ϕ_{MV}, while the dash-dotted line shows $\phi = 1$ corresponding to the resonant frequency of a stationary swimmer predicted by linear theory [91].

for stationary and moving swimmers as functions of added mass T. The dashed line represents the frequency of maximum velocity, $\phi_{MV} = 1.1$, while the dash-dotted line indicates the fundamental frequency $\phi = 1$ as predicted by the linear theory [91].

We find that $\phi_{1,\text{stat}}$ is within 6% from the linear theory prediction, suggesting that this difference arises due to non-linear hydrodynamic effects accounted for by our computational model. Furthermore, we find that the natural frequency for a moving swimmer $\phi_{1,\text{swim}}$ systematically exceeds that of a stationary swimmer $\phi_{1,\text{stat}}$ with identical T. It indicates that the oncoming flow imposes an increased restoring force on the swimmer, thereby increasing its effective stiffness and the natural frequency in fluid.

We also find in Figure 18b that $\phi_{1,\text{swim}}$ is between 3% and 7% greater than ϕ_{MV}. Thus, the maximum velocity takes place at a frequency which is close to that of the natural frequency in a moving fluid. On the other hand, the frequency of maximum deflection ϕ_d deviates significantly from ϕ_{MV} and ϕ_1 when T increases. The latter is related to greater damping due to fluid experienced by lighter swimmers.

3.2.4 Relationship between Economy and Driving Force

This difference in motion pattern leads to a significant difference in power consumption of the swimmer between the MV and ME regimes. The power is found by

$$P = \frac{1}{\tau} \int_{t'}^{t'+\tau} \mathbf{F}_e(t) \cdot \mathbf{v}_l(t)\, dt, \tag{44}$$

where $\mathbf{v}_l(t)$ is the velocity of the leading edge and $\mathbf{F}_e(t)$ is the external force applied at the leading edge. In our model of a free swimmer, we set the horizontal component of external force equal to zero leading to

$$P = \frac{1}{\tau} \int_{t'}^{t'+\tau} F_{e,z}(t)\, v_{l,z}(t)\, dt. \tag{45}$$

The power, therefore, only depends on the vertical components (z subscript) of external force and leading edge velocity.

Figure 19a shows the time variation of the leading edge velocity and the vertical component of external force during one period for MV and ME swimming regimes. We find that in both these regimes the external force and leading edge velocity change

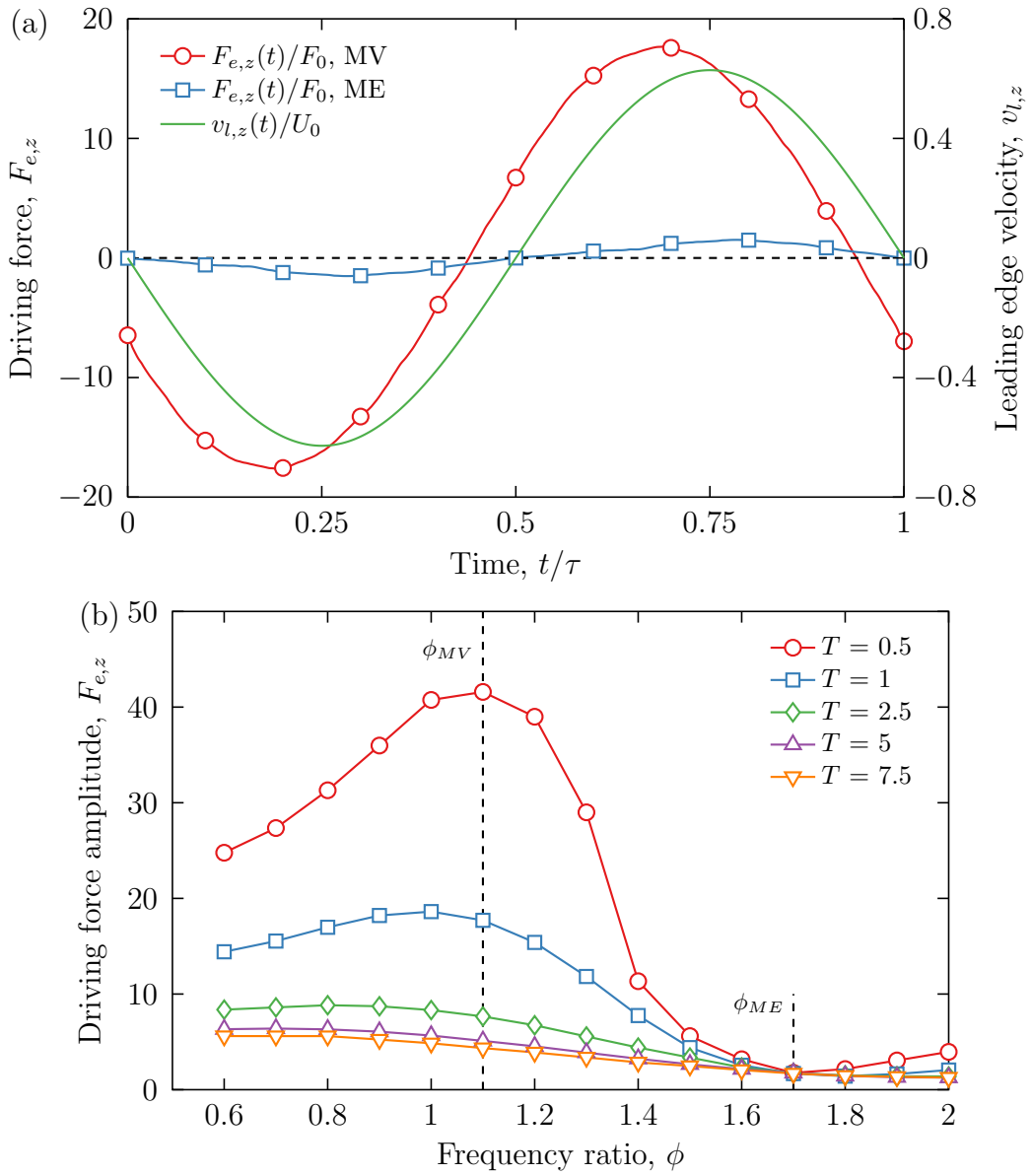

Figure 19: (a) Driving force and leading edge velocity as a function of time for an elastic swimmer with $T = 1$, Re $= 250$, and $AR = 2.5$. The force and leading edge velocity are normalized by $F_0 = 0.5\rho U_0^2 wL$ and U_0, respectively. (b) Magnitude of driving force as a function of frequency ratio for swimmers with different values of added mass T. Driving force is minimized at the frequency of maximum economy, ϕ_{ME}.

nearly in phase. We have obtained similar results in our simulations at other frequencies. Thus, the power required to drive the swimmer is linearly proportional to the amplitude of the external force applied to the swimmer leading edge. Indeed, for

$T = 1$, we find that the force amplitude in MV is almost 10 times larger than that of ME, which is similar to the 12 times change in power between these regimes (Figure 13b).

The driving force amplitude is shown in Figure 19b as a function of frequency ratio. We find that for swimmers with smaller added mass, the force maximizes near the first natural frequency and has a minimum near ϕ_{ME} where the forces due to the fluid in front of and behind the centroid nearly negate each other. The latter results in a relatively small force at the swimmer leading edge throughout the entire oscillation period. For swimmers with larger added mass, the external force has neither a minimum nor a maximum at either the ME or MV regimes. Nevertheless, the shape of the force dependence on frequency is quite similar to that of the power for swimmers with different added masses. The discrepancy points to the fact that other contributions, such as leading and trailing edge vortices, increase the overall amount of power dissipated by the plunging elastic swimmer.

3.2.5 Relationship between Velocity and Kinematics

To examine the MV regime, we plot in Figure 20a the swimmer trailing edge displacement for different ϕ and T as a function of the forward swimming velocity. We find that the swimming velocity is nearly linearly related to trailing edge displacement. This is quite remarkable because this relationship is independent of the bending patterns and weakly dependent on the added mass. Thus, the larger swimmer deflection due to resonance results in a faster swimming velocity. With higher trailing edge displacements, however, the velocity increase begins to saturate. At this point, the large swimmer deformation generates additional drag that surpasses the increase in propulsion. In other words, a larger tip displacement is beneficial for faster swimming, but only up to a certain point when an excessive swimmer deformation becomes detrimental and yields diminishing returns.

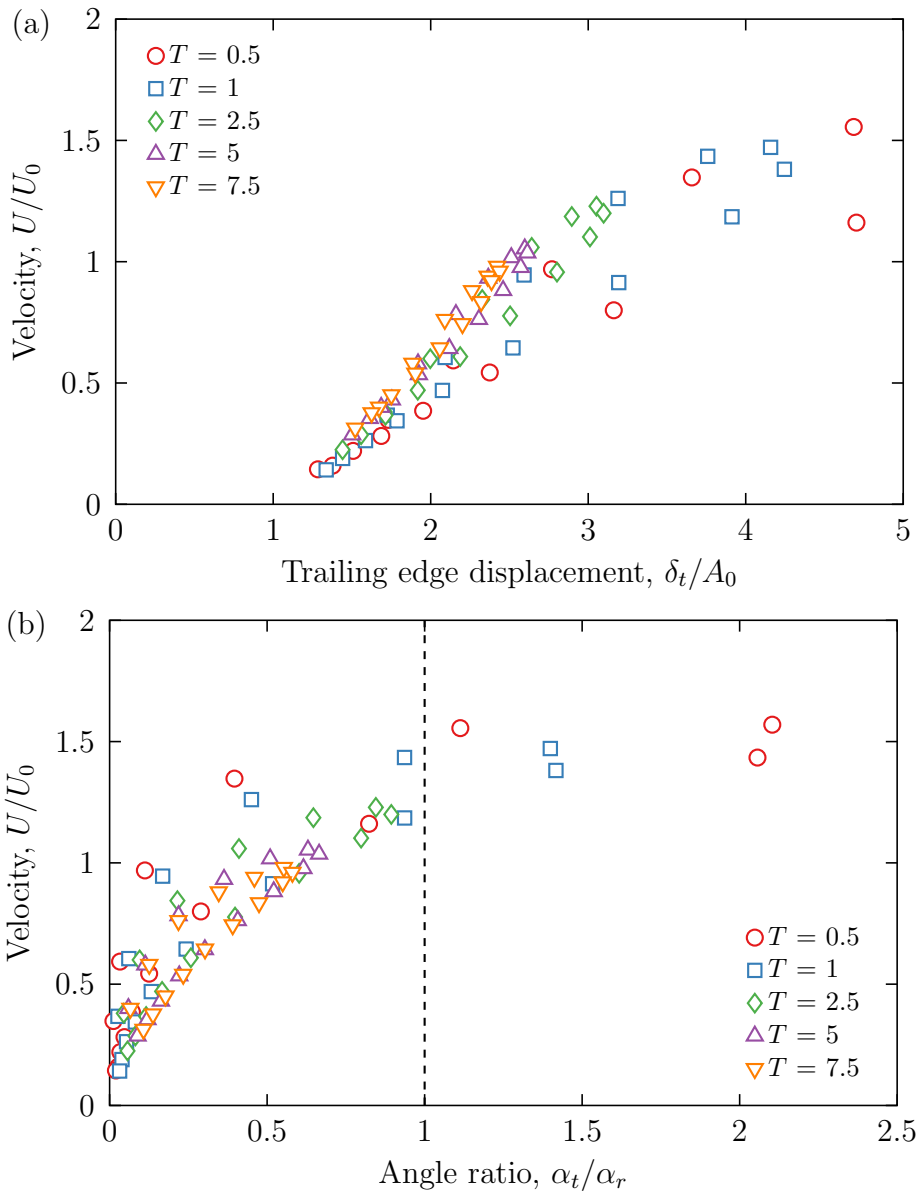

Figure 20: Free swimming velocity as a function of (a) trailing edge displacement and (b) angle ratio for elastic swimmers with Re = 250 and $AR = 2.5$ driven with frequency ratios in the range $0.6 < \phi < 2$. For smaller displacements, velocity and displacement have nearly a linear relationship. For larger displacements, swimming velocity saturates. The velocity saturation is more apparent when the angle ratio is greater than 1.

To further characterize swimmer motion, we examine how velocity depends on the angle ratio α_t/α_r, as defined by Ramananarivo, et al. [85]. Here, the angle ratio is the ratio of two characteristic angles: α_t and α_r. Consider a snapshot at the moment

when the leading edge is plunging with the maximum velocity. During this moment, α_t is the angle the trailing edge makes to the horizontal, whereas $\alpha_r = \arctan(\omega A_0/U)$ is the angle characterizing the ratio of vertical to horizontal velocity components at the leading edge and represents the instantaneous plunging direction.

As shown in Figure 20b, the swimming velocity increases with a higher angle ratio. This occurs because a higher angle ratio is associated with a higher trailing edge angle α_t, and this is related to the trailing edge displacement δ_t. A transition point of optimal thrust production was found to occur near $\alpha_t/\alpha_r \approx 1$ [85]. While we cannot directly compare our simulations to the results reported by Ramananarivo, et al. [85] due to a significant difference in Reynolds numbers, we find that $\alpha_t/\alpha_r \approx 1$ indeed corresponds to a regime yielding the maximum swimmer velocity as shown in Figure 20b. Furthermore, for $\alpha_t/\alpha_r > 1$, the velocity saturates, indicating that the swimmer deformation is becoming excessive which, in turn, impinges the swimming performance.

3.2.6 Strouhal Number Dependence

As we discussed in the introduction, swimming and flying are often analyzed in terms of the Strouhal number $\mathrm{St} = 2fl/U$, where l is a characteristic length of the swimmer geometry and $f = \omega/2\pi$. The Strouhal number represents the ratio between the time scales of vortex shedding and swimmer motion. Typically, the characteristic length in a plunging or heaving swimmer is the leading edge amplitude, A_0, while this length in a pitching swimmer is usually the trailing edge amplitude δ_t. The range of Strouhal numbers $0.2 < \mathrm{St} < 0.4$ is typically linked to efficient swimming [73–76], although a wider range was suggested based on the Lighthill's reactive theory [79].

For a freely moving elastic swimmer, the Strouhal number is inherently an output parameter since the swimming velocity is determined by the swimmer hydrodynamics. Furthermore, the displacement of the swimmer's trailing edge is a result of the

dynamic swimmer deformation and is governed by a delicate interplay between elastic and hydrodynamic forces. In Figure 21, we plot the Strouhal number as a function of swimming economy for all swimmers considered in our study that are operated at frequencies $0.6 < \phi < 0.2$. We present two values for St based on, respectively, leading and trailing edge displacements.

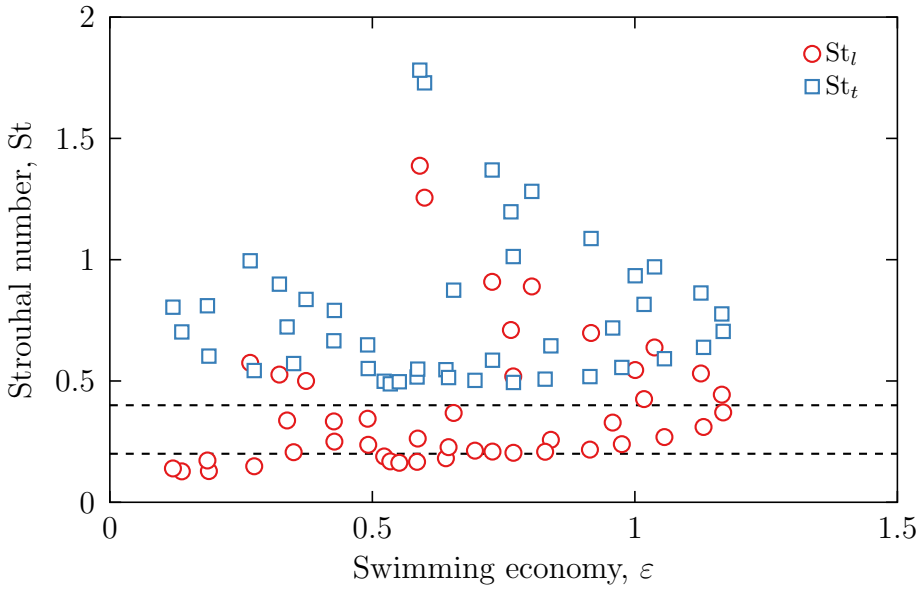

Figure 21: Strouhal number as a function of swimming economy for elastic swimmers with $\mathrm{Re} = 250$, $AR = 2.5$, $0.5 < T < 7.5$ driven with frequency ratios in the range $0.6 < \phi < 2$. The dimensionless number is defined using two different length scales: leading edge displacement, St_l, and trailing edge displacement, St_t. For the majority of natural flyers and swimmers, studies [73–76] have shown that $0.2 < \mathrm{St} < 0.4$. This region is bounded by the dotted lines.

We find that Strouhal numbers St_t based on the trailing edge displacement are higher than 0.5 for all swimmers. The values of St_l, which are calculated using the constant amplitude of the leading edge displacement, lay within the range $0.2 < \mathrm{St}_l < 0.4$ for the majority of the swimmers, including swimmers with both high and low economy. For a limited number of swimmers that operate at frequencies $\phi > 1.8$ and exhibit particularly low economy, St_l exceeds 0.5. Thus, the Strouhal number of free-swimming elastic swimmers does not appear to be an effective indicator of economy, as the majority of the swimmers exhibit similar values of St irrespective to

their actual swimming economy.

3.3 Summary

In this chapter, we have established an understanding of the physics behind the free swimming of a plunging flexible plate with $AR = 2.5$ actuated near the first natural frequency. From a design standpoint, our findings indicate that simple flexible robotic fin propulsors can be tuned to two vastly different free swimming modes leading to either fast or efficient swimming by simply altering the actuation frequency. We find that heavier fins swim faster and there is a nearly linear relationship between free swimming velocity and trailing edge displacement, indicating that swimming at higher speeds requires a larger displacement of the trailing edge.

Swimming fast, however, comes with the cost of a higher power required to drive the swimmer. In the MV regime, the increase in power is the most dramatic for heavier swimmers, leading to a significant drop in their swimming economy. Lighter swimmers consume less power and show superior economy. A regime of maximum economy (ME) was found near an off-resonance frequency $\phi_{ME} \approx 1.7$. In this regime, the elastic swimmer exhibits a bending pattern in which its center of mass has a minimum displacement normal to the swimming direction. This swimming pattern minimizes the magnitude of external force required to sustain the motion, which in turn reduces the input power and enhances swimming economy.

CHAPTER IV

SHAPE EFFECTS OF PLUNGING FLEXIBLE PLATES IN FREE SWIMMING

4.1 Introduction and Computational Setup

In Chapter 3, we studied the swimming performance of flexible oscillating plates near resonance with a fixed aspect ratio of $AR = 2.5$. We found two distinct swimming regimes, one near resonance with maximum velocity, and another away from resonance that maximizes swimming economy. Furthermore, the study established a baseline set of results for comparison. In nature, fish caudal fins are not rectangular, and understanding the effect of shape changes on swimming performance is important for biomimetic design. Inconclusive results from literature (discussed in Chapter 1) indicate that hydrodynamic effects associated with fins of different shapes are not fully understood.

In this chapter we study the effects of shape changes on free swimming performance of flexible plates. There is an infinite set of possible geometries, but we limit the study to two simple shapes, rectangles and trapezoids, in order to understand the fundamental effects of incremental geometrical changes. The trapezoidal shape is inspired by the approximate shape of many caudal fin varieties. We expect that a change in area would contribute to more thrust, but this may be balanced by an equally larger amount of drag, so the effect on free swimming is unclear. Towards this goal, we systematically study the hydrodynamics of rectangular and trapezoidal plunging flexible plates with different aspect ratios, referred to as swimmers, undergoing free locomotion. Surprisingly, we find that swimmers with smaller aspect ratios (wider swimmers) are faster and more efficient. We explain this effect by showing

that the wider swimmers have less vortex-induced drag per unit width, which is the dominant source of drag.

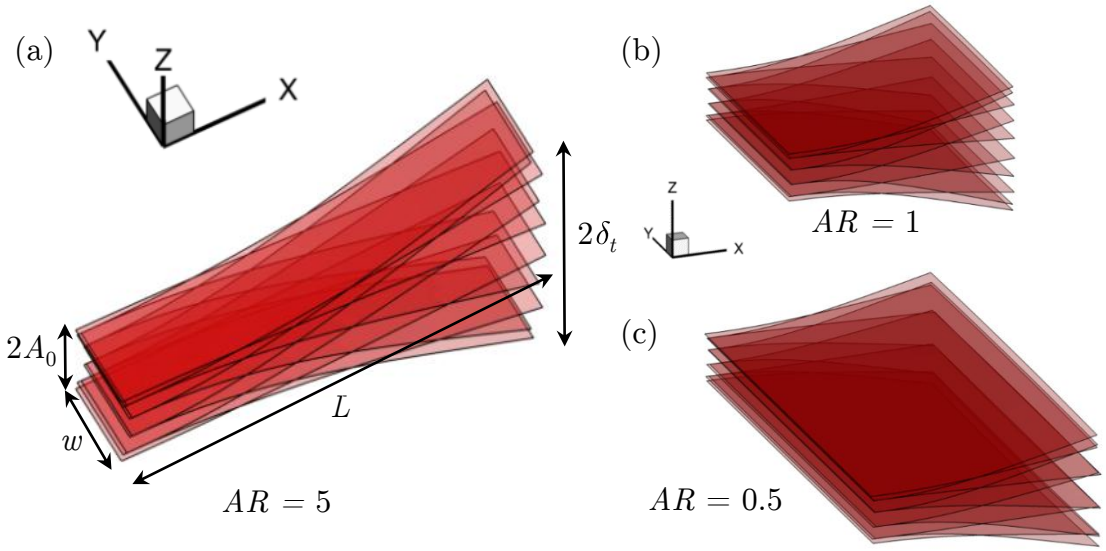

Figure 22: Schematic of swimmers with aspect ratios (a) $AR = 5$, (b) $AR = 1$, and (c) $AR = 0.5$ (L is kept constant between the 3 cases). In all cases, the leading edge undergoes a sinusoidal plunging motion with amplitude A_0. Overlaid are transparent snapshots of the bending pattern at different instants of time during one period when the swimmers are actuated at the natural frequency.

The details of the computational model are given in Chapter 2, so we briefly discuss the model parameters here. The rectangular swimmer is modeled as a thin, elastic plate with length L and width w. The plate thickness b is sufficiently small, i.e. $b \ll L$, so the plate assumed to be infinitely thin. We characterize the swimmer geometry by the aspect ratio $AR = L/w$. Figure 22 illustrates the geometry of swimmers with 3 different aspect ratios. We vary rectangular aspect ratio by keeping L constant and changing w. As Figure 22 shows, the swimmer leading edge undergoes a prescribed sinusoidal plunging motion given by $A(t) = A_0 \cos(\omega t)$. Note that in our simulations we keep ω and A_0 constant, and we consider swimmers with added mass parameter $T = \rho L/\rho_s b = 2.5$.

4.2 Results and Discussion

4.2.1 Rectangular Swimmer: Performance Characterization

We examine the free swimming of plunging elastic plates with aspect ratios ranging from $AR = 0.5$ to $AR = 5$. In Figure 23a, we graph the dimensionless swimming velocity as a function of frequency ratio, where the different curves represent different aspect ratios. Figure 23a shows that the free swimming velocity is maximized in all cases near $r = 1$, the first natural frequency of the swimmer. The fastest swimmer studied has $AR = 0.5$ and moves with a velocity equal to nearly 2 body lengths per period. Moreover, we find that the swimming velocity is faster for lower aspect ratio swimmers at all driving frequencies considered. This result indicates the significance of the three dimensional hydrodynamic effects on the swimmer propulsion. If the three dimensional effects had a negligible effect on the swimming and the flow was primarily two dimensional in the xz–plane (Figure 22), then we would expect that both the net thrust and drag be proportional to the swimmer width. Since swimming velocity occurs as a balance between these two forces, the swimming velocity should therefore not depend on the aspect ratio if the three dimensional flow effects could be neglected. The strong dependence of swimming velocity on aspect ratio therefore highlights the importance of these effects. This conclusion is in agreement with recent experiments on free swimming with high aspect ratio swimmers, although in that case the swimmers were actuated far from the first natural frequency [123].

To further characterize the swimmer motion, we examine the trailing edge displacement. In Figure 23b, we show the maximum trailing edge displacement δ_t as a function of frequency ratio for swimmers with different aspect ratios. Here, δ_t is normalized by plunging amplitude A_0. Similar to the swimming velocity, we find that δ_t is maximized near the first natural frequency. It is interesting that near $r = 1$, δ_t decreases with decreasing aspect ratio, even though low aspect ratio swimmers are faster. We attribute this higher displacement of high aspect ratio swimmers to its

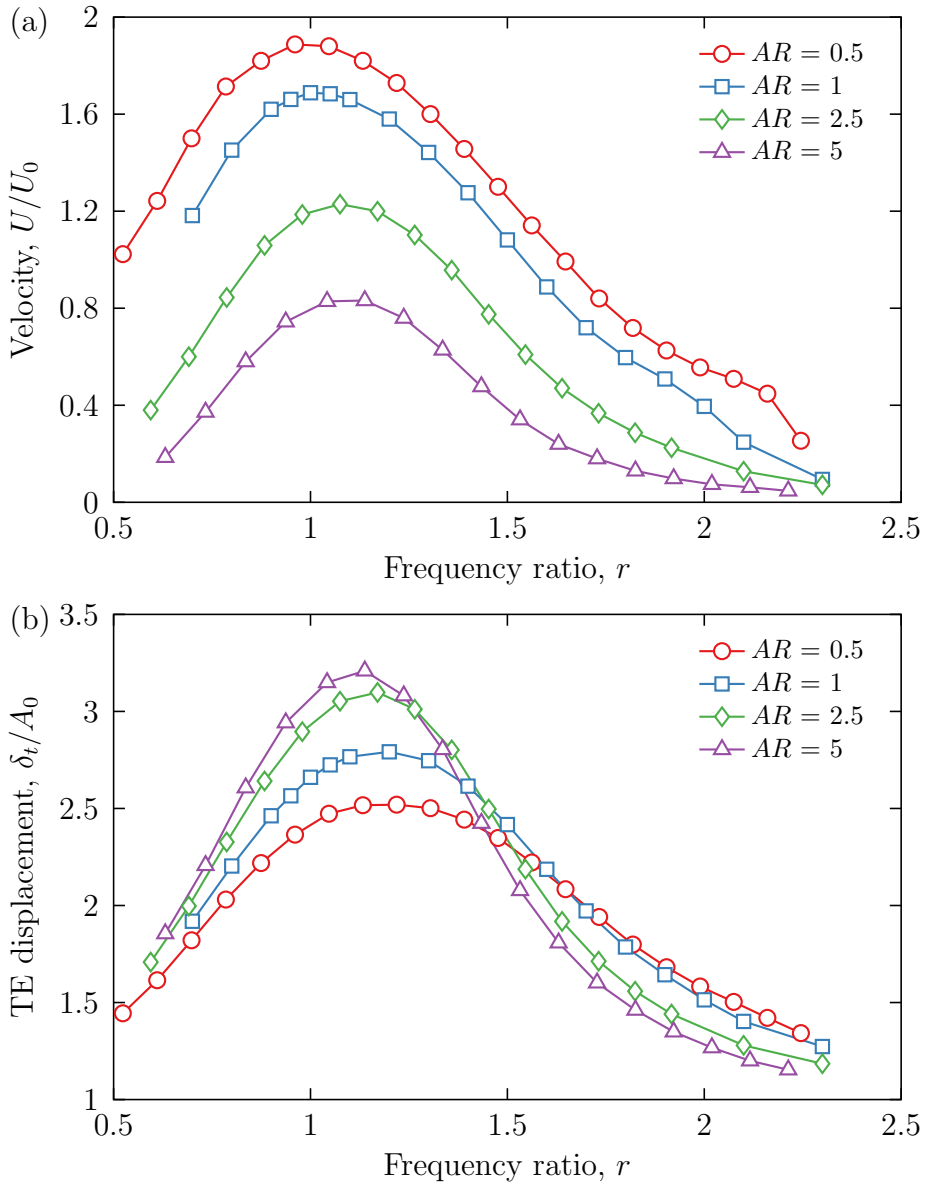

Figure 23: (a) Free swimming velocity and (b) maximum trailing edge displacement as a function of frequency ratio for different aspect ratios. Both quantities are maximized near the first natural frequency. It is interesting that low aspect ratio swimmers can move fastest despite having a smaller trailing edge amplitude.

smaller added mass. Compared to wide, low aspect ratio swimmers with the same length, the narrow swimmers displace a smaller volume of fluid (the added mass) that mostly flows in this case around the swimmer side edges. The decreased amount of added mass leads to lower dynamic resistance to bending, thereby increasing δ_t. Indeed, a larger trailing edge displacement was found for swimmers with smaller added

mass in Chapter 3.

Free swimming is characterized by a condition when period-averaged net thrust and drag are equal to each other. For the same frequency ratio and, therefore, similar bending pattern, a larger trailing edge amplitude would produce more thrust because more fluid momentum would be transferred backwards. But lower aspect ratio swimmers, which are faster, remarkably have lower trailing edge amplitudes, implying less thrust generation per unit width. Therefore, this suggests that lower aspect ratio swimmers experience lower drag per unit width than high aspect ratio swimmers that swim more slowly. Indeed, previous studies have indicated that low aspect ratio swimmers experience less drag [70, 123].

We also measure the input power consumption for the swimmers as a function of frequency ratio shown in Figure 24a. Here, the power is per unit width in order to account for the fact that swimmers with a larger area require more power. We find a trend that is similar to that of the swimming velocity — the required power per unit width is maximized near the first natural frequency. The dependence of power on aspect ratio demonstrates the contribution of the three dimensional flow effects. Specifically, low aspect ratio swimmers require the highest input power. We find this trend holds regardless of the driving frequency. For high aspect ratio swimmers, the input power per unit width saturates. Indeed, despite the factor of two difference in aspect ratio between $AR = 2.5$ and $AR = 5$, the power curves nearly overlap.

To quantify how well the input power translates into swimming speed we examine the swimming economy, given as the ratio between swimming velocity and power. We emphasize that the conclusions drawn here are by characterizing the power on a per unit width basis, not absolute power. In Figure 24b we graph the swimming economy as a function of driving frequency. We find that for each aspect ratio, the most economical swimming occurs away from the first natural frequency. In fact, for low aspect ratio swimmers, we find a local minimum of economy at the first natural

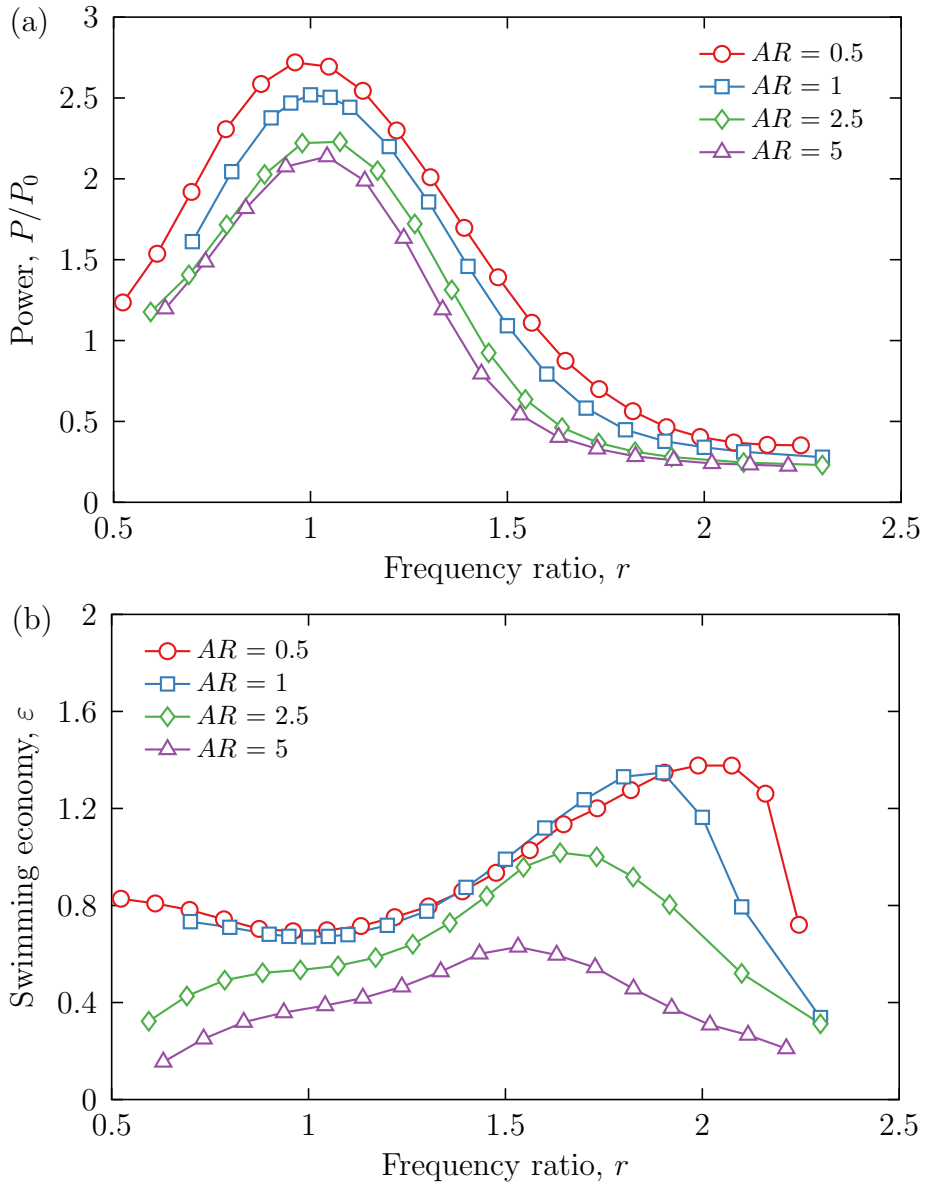

Figure 24: (a) Power per unit width and (b) swimming economy for swimmers with different aspect ratios. Power is maximized near the first natural frequency, while swimming economy has a maximum away from $r = 1$ which depends on aspect ratio. Low aspect ratio swimmers are found to be the most economical.

frequency. Therefore, driving the swimmer near the first natural frequency results in fast swimming but with poor economy. This tradeoff between velocity and swimming economy is consistent with our results from Chapter 3. We also observe that the low aspect ratio swimmers have the highest swimming economy, despite requiring more input power. This is due to a larger improvement in swimming velocity. Furthermore,

we find an optimal driving frequency for each aspect ratio that leads to maximum swimming economy. As we will show in the next section, the maximum swimming economy is associated with a specific bending pattern regardless of aspect ratio.

4.2.2 Rectangular Swimmer: Bending Patterns and Vortex Structures

In Figure 25, we plot the bending patterns of swimmers with $AR = 5$ and $AR = 0.5$ driven at maximum velocity and maximum swimming economy. The solid lines represent the downstroke of the leading edge, while the dashed lines represent the upstroke. Despite the large difference in width between the two swimmers, we find a consistent bending pattern in both swimming regimes. Specifically, during maximum velocity (Figures 25a and 25b), the envelope size monotonically increases from the leading to trailing edge. This shape is favorable for propulsion because a larger amount of fluid can be accelerated backwards. During maximum swimming economy, a different bending pattern emerges. Here, the envelope shows a minimum near the center of the swimmer. Both of these bending patterns are consistent with our Chapter 3 results for a swimmer with $AR = 2.5$. Thus, this result demonstrates that these special bending patterns are universal and lead to maximum velocity or swimming economy regardless of the aspect ratio.

The vortex structures for the swimming cases shown in Figure 25 are illustrated in Figure 26. Here, we plot iso-surfaces of constant vorticity magnitude in three dimensional space (Figures 26a–26d). All surfaces are plotted at the same scale. In all cases, we can identify horseshoe-shaped trailing edge vortices (TEV) that are shed in the wake, similar to Chapter 3 and other previous studies [68, 77, 124]. Side edge vortices (SEV) are also produced during the oscillatory motion. These SEV do not contribute to the propulsion, but rather result in increased energy dissipation. Indeed, if we compare the SEV generated by the swimmers at the maximum velocity (Figures 26a and 26b) to the SEV at the maximum swimming economy (Figures 26c and 26d),

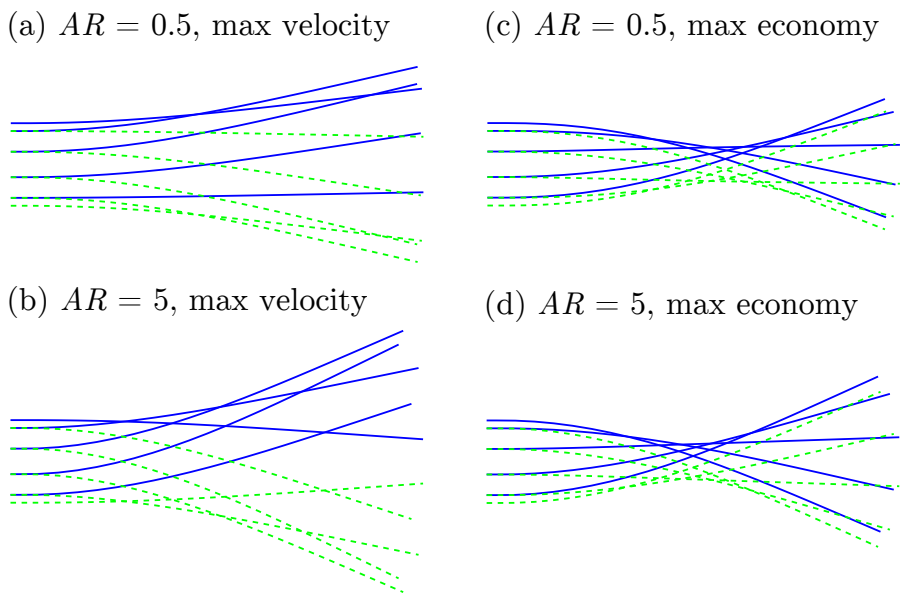

Figure 25: Bending patterns for different aspect ratios at the maximum velocity and the maximum economy regimes.

we find that the magnitude of SEV is greatly reduced in the latter case.

4.2.3 Vortex-Induced Drag

Recently, Raspa, et al. [123] proposed that the SEV leads to "vortex-induced drag." They used a scaling argument to conclude that this must be the largest contribution of drag for an oscillatory swimmer. Their scaling argument predicts that the total drag increases with the size of the SEV, and also that the size of the SEV increases with the trailing edge displacement and not the swimmer width. Thus, for a constant trailing edge displacement, the total vortex-induced drag is the same regardless of the swimmer width, so low aspect ratio swimmers experience lower drag per unit width.

To verify their theory, we plot the vorticity magnitude contours (plotted at the same scales) in the yz–plane at the trailing edge for $AR = 5$ and $AR = 0.5$ (Figures 26e and 26f, respectively). For each case, the snapshot is taken during the instant of time when the trailing edge is moving the fastest. We find that the SEV for $AR = 5$ are only slightly larger than the SEV for $AR = 0.5$, consistent with the

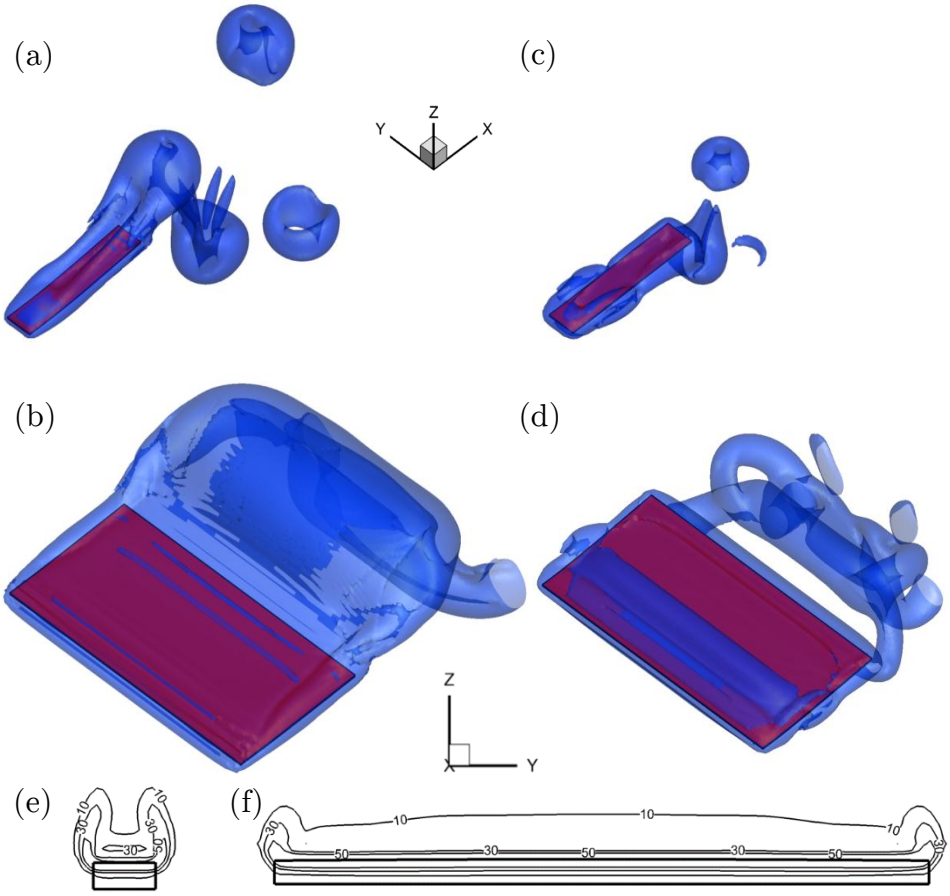

Figure 26: Vortex structures during the maximum velocity for (a) $AR = 5$ and (b) $AR = 0.5$ and during the maximum swimming economy for (c) $AR = 5$ and (d) $AR = 0.5$. Surfaces of constant vorticity magnitude plotted at the same scale. Vorticity magnitude contours within a slice in the yz–plane at the trailing edge during the instant of the fastest trailing edge movement for (e) $AR = 5$ and (f) $AR = 0.5$ at maximum velocity. Vorticity magnitude is normalized by the driving frequency $\omega/2\pi$.

approximately 1.3 times difference in the trailing edge displacement (Figure 23b), despite the 10 times difference in width. Thus, the characteristic size of the SEV for low aspect ratio swimmers are small compared to the width of the swimmer. This results in reduced average drag per unit width for the wider swimmers. As seen earlier in Figure 23b, the trailing edge displacement at all frequencies is comparable, differing by no more than 1.3 times. The thrust per unit width depends on the trailing edge displacement [61], so we expect that the thrust per unit width is comparable

between different aspect ratio swimmers holding frequency ratio constant. Therefore, for comparable thrust per unit width, the reduced drag per unit width of low aspect ratio swimmers allows them to cruise forward more quickly (Figure 23a).

4.2.4 Trapezoidal Swimmer: Performance Characterization

In this section we present the results for the swimming performance of trapezoidal plates plunging in fluid. The trapezoidal geometry is characterized by the width ratio $w_R = w_l/w_t$, the ratio between the widths of the leading and trailing edges. We consider values of $w_R = 0.25, 1, 4$, where $w_R = 0.25$ represents a widening trapezoid down the length of the swimmer, and $w_R = 4$ is a narrowing trapezoid. The $w_R = 1$ case is the same as the $AR = 1$ swimmer and serves as a case for comparison. In all 3 cases, the length L and swimmer area remain the same in order to understand the effect of shape change without increasing area (as was the case for the rectangular plates).

In Figure 27, we plot the velocity and trailing edge displacement δ_t as functions of frequency ratio r. For both velocity and δ_t, the trends in r are similar to that of rectangular swimmers. Both velocity and displacement are maximized near the first natural frequency. It interesting that the swimming velocity for trapezoidal swimmers is nearly the same when comparing each individual values of r, not differing by more than 15% of the maximum velocity. The trapezoidal shape appears to not be beneficial for swimming, and surprisingly, we find that the fastest swimmer $r = 1$ is the rectangular one, albeit with only a modest improvement over the $w_R = 0.25$ swimmer. At higher frequencies, the trapezoidal swimmers are faster, but all of them have speeds that are nearly zero.

As with rectangular swimmers, we can attribute the larger trailing edge displacement of the narrowing swimmers ($w_R = 4$) to the added mass effect. The trailing

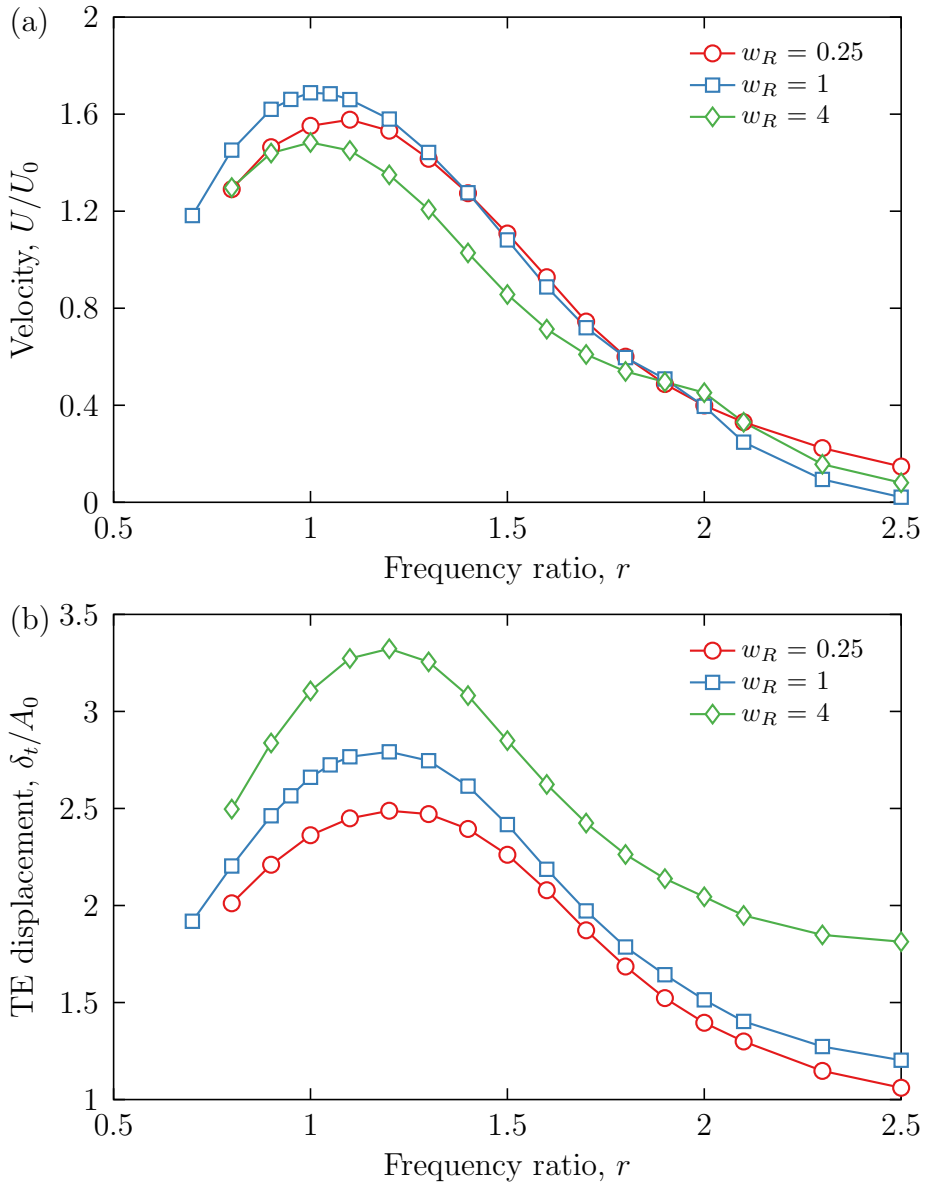

Figure 27: (a) Free swimming velocity and (b) maximum trailing edge displacement as functions of frequency ratio for trapezoidal swimmers. Both quantities are maximized near the first natural frequency. It is interesting that $w_R = 4$ has a high trailing edge amplitude but moves nearly the same speed as the others.

portion of the swimmer is displaces the most fluid, so between widening and narrowing swimmers, clearly the narrowing swimmer displaces less fluid. The less fluid displaced offers less resistance to bending, so the narrowing swimmer has a larger deformation. In a similar fashion, the thrust is generated mostly by the fluid deflection of the trailing portion of the swimmer. The thrust and velocity (keeping drag

constant) increases with both trailing edge amplitude and width as large quantities of either results in more fluid displaced backwards. The widening swimmer has a larger width but smaller deformation, while the opposite is true for the narrowing swimmer. The drag also may increase by a small amount for narrowing swimmers due to larger trailing edge displacement, but the drag is approximately the same for all cases because the area is constant. Evidently, these competing effects balance out, and the result is that the swimming speed for all trapezoidal plates differ by no more than 15% and usually are within 10% of each other over a large range of frequency ratios.

In Figure 28, we plot both the power and swimming economy for trapezoidal swimmers. The power behaves similarly as that of rectangular swimmers, with a maximum near $r = 1$. The swimming economy also behaves similarly to that of rectangular swimmers with a maximum away from resonance. The power for the widening swimmer ($w_R = 0.25$) is about 20% higher than the narrowing one at the first natural frequency, but this represents the largest difference in power when comparing the difference cases at the same frequencies. For $r < 2$, the swimming economy also maintains similar values between the 3 cases. For $r > 2$, the widening swimmer maintains a higher economy, but all 3 cases show reduced swimming economy at higher frequencies. Thus, between trapezoidal shapes with the same area, we observe only small changes in swimming performance.

4.3 Summary

In this chapter we investigated the effects of shape changes in the swimming performance of flexible plunging plates. We showed that the effects of changing bending rigidity of these swimmers are similar to the trends found in Chapter 3. Specifically, swimming speed and power consumption are highest near the first natural frequency,

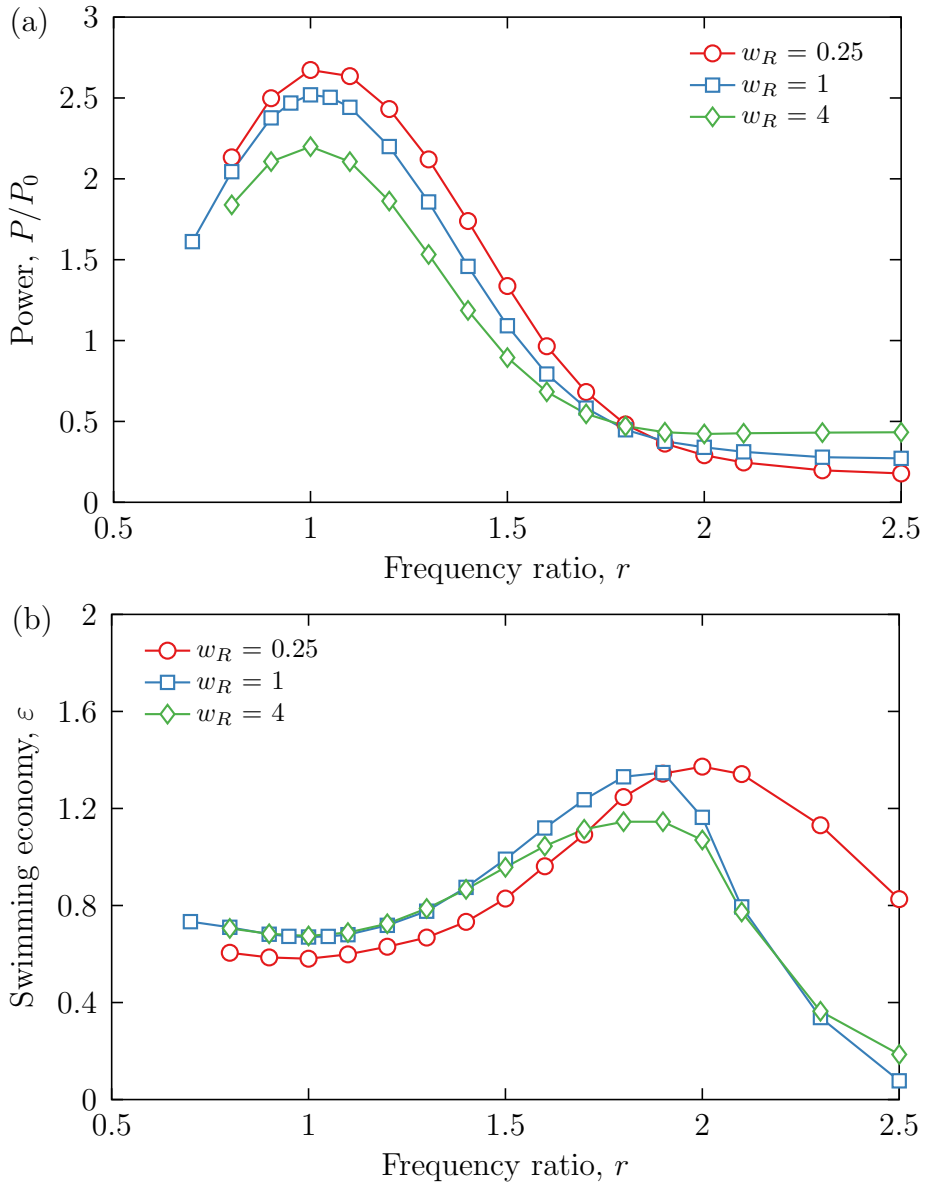

Figure 28: (a) Power and (b) swimming economy for swimmers with different aspect ratios. The power is normalized by the same characteristic power for $AR = 1$ swimmers. The curves for different w_R behave similarly to one another.

and that this result is independent of aspect ratio. The frequency of maximum swimming economy changes for different aspect ratios, but in all cases it was found to be away from the first natural frequency and associated with a specific bending pattern minimizing the energy dissipation.

Surprisingly, we found that the lowest aspect ratio swimmers move the fastest due

to a lower net drag. This drag is induced by the side edge vortices (SEV), whose size depends on the trailing edge displacement. For lower aspect ratio (wider) swimmers, the SEV size to width ratio is smaller than for higher aspect ratio swimmers. Thus, wider swimmers can swim faster. For trapezoidal swimmers with the same area, we found little performance change between the different cases. The differences in the bending responses and geometries for the different trapezoidal swimmers led to competing changes in thrust generation that ultimately balanced out, causing velocity and swimming economy to be similar. From a design standpoint of a simple flexible propulsor, our results suggest that the shape affects the swimming performance less than maintaining a larger area and low aspect ratio in order to maintain lower drag. Our results do not imply that the trapezoidal fins in aquatic mammals are suboptimal, but rather there may be additional factors that dictate how natural fins are optimized.

CHAPTER V

FREE SWIMMING OF FLEXIBLE PLUNGING PLATES WITH TAPERED THICKNESS

5.1 Introduction and Computational Setup

In the previous chapters we studied the free swimming of flexible plunging plates with uniform thickness. These results are important for the biomimetic design of simple flexible propulsors. In this chapter we consider non-uniform thickness as a design parameter, motivated by the observation that almost all fish caudal fins have tapered thicknesses. Experiments on complex models of tapered biomimetic pectoral fins showed that tapered fins exhibited more thrust and larger curvature [125, 126]. These studies, however, lacked control of bending patterns and considered a complicated geometry in order to study live fish performance. Systematic parametric studies on the effect of tapering on a simple flexible fin model do not exist in the literature to the best of our knowledge.

In this chapter we study the free locomotion of tapered flexible plates (referred to as tapered swimmers) driven near the first natural frequency. We characterize the swimming performance of the tapered swimmers and compare the performance to uniform swimmers. The results of this chapter show that near the first natural frequency, the tapered plates are slower, but modestly more economical than uniform swimmers. The interesting result is that at higher frequencies, plates with high taper ratios maintain high swimming economy and moderate swimming speed when the uniform swimmer declines considerably in both areas. We explain these results by showing that the non-uniform thickness leads to bending patterns that maintain larger deformations at higher frequencies. These results hold for plates with both

rectangular and trapezoidal geometries.

Details of the computational model are given in Chapter 2, so we briefly discuss the important model parameters here. We investigate the swimming performance of both tapered rectangular swimmers and also tapered trapezoidal swimmers. The tapered swimmer is modeled as a thin, elastic plate whose thickness varies linearly across its length from a thickness of b_l at the leading edge (LE) and b_t at the trailing edge (TE). The taper ratio $a \equiv b_l/b_t$ characterizes the degree of tapering. On the entire length, the thickness is negligible compared to the length, i.e. $b(x) \ll L$. Figure 29 shows the example schematic for a tapered rectangular swimmer. We prescribe a sinusoidal plunging motion at the leading edge, $A(t) = A_0 \cos(\omega t)$ (shown in Figure 29c).

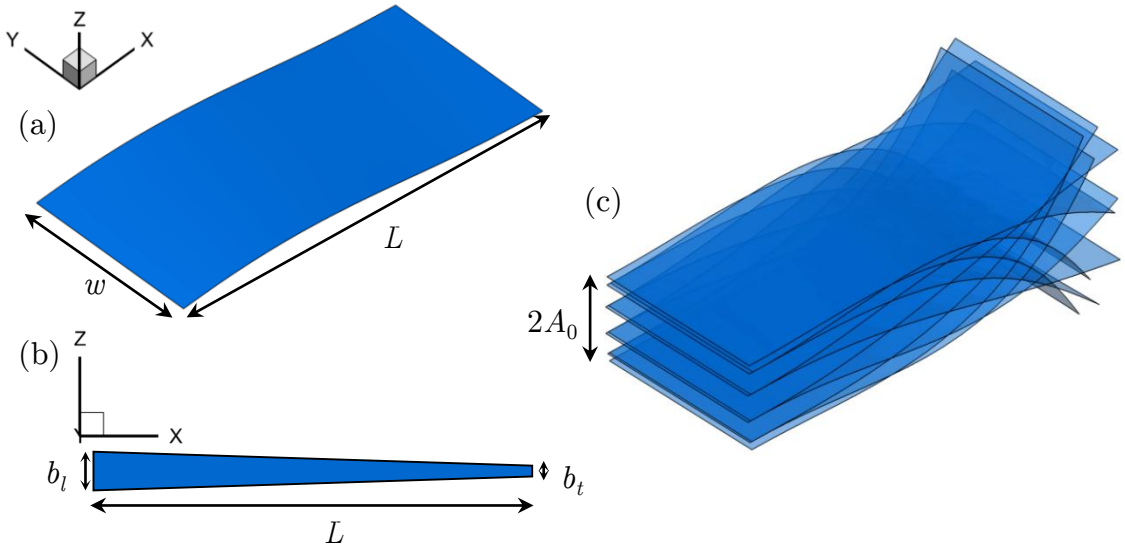

Figure 29: Schematic of the rectangular tapered swimmer. (a) The swimmer is modeled as an elastic plate with length L and width w. (b) The thickness of the plate starts at b_l at the leading edge and decreases linearly to a thickness of b_t at the trailing edge. This schematic is not drawn to scale, but $b(x) \ll L$ for the entire length of the plate. (c) Snapshots of the swimmer deformation pattern while in motion. The leading edge oscillates in a sinusoidal plunging pattern with amplitude A_0.

This swimmer is submerged within an incompressible Newtonian fluid with viscosity μ and density ρ, leading to a constant Reynolds number $\mathrm{Re} = \rho\omega A_0 L/\mu = 250$. In

addition, the swimmer dynamic bending response depends on the mass ratio between the solid and fluid, $\chi = \rho w/\rho_s \bar{b}$, where ρ_s is the density of the solid swimmer and $\bar{b}$ is the average thickness. In this study, we fix the mass ratio to be constant and equal to 1.[1] The mass ratio χ is equivalent to the added mass of the fluid periodically displaced as the swimmer plunges through the fluid.

5.2 Results and Discussion

5.2.1 Performance Characterization of Tapered Rectangular Swimmer

First, we investigate the swimming velocity of the tapered rectangular swimmer. We plot in Figure 30a the dimensionless velocity U/U_0 of the swimmer as a function of frequency ratio r. Different curves represent different values of taper ratio a, ranging from 1 to 10. We find that the maximum velocity is close to $r = 1.1$ for all values of a, suggesting that resonance oscillations enhance swimming speed. At this maximum velocity regime, the uniform swimmer actually swims with the fastest speed, which decreases slightly with increasing a. However, the trend is reversed for post-resonance frequency ratios above $r = 1.5$. At these higher frequencies, the swimming speed for the uniformly thick swimmer drops to nearly zero. For $a = 10$, the minimum velocity is more than half (about 60%) of its maximum velocity. The variation with frequency for tapered swimmers is not as extreme as with the uniformly thick $a = 1$ case. These results indicate that swimmers with large taper ratios can be actuated at a wide range of frequencies without suffering from heavily reduced swimming performance away from resonance.

The power P/P_0 associated with free swimming is shown in Figure 30b as a function of frequency ratio r. The power variation with frequency ratio is similar to that of swimming velocity. The input power is maximized near $r = 1.1$ in the resonance regime, while the power is decreased at frequencies above approximately

[1]For uniform swimmers, this is equivalent to the ones in Chapter 3 with $T = \rho L/\rho_s b = 2.5$.

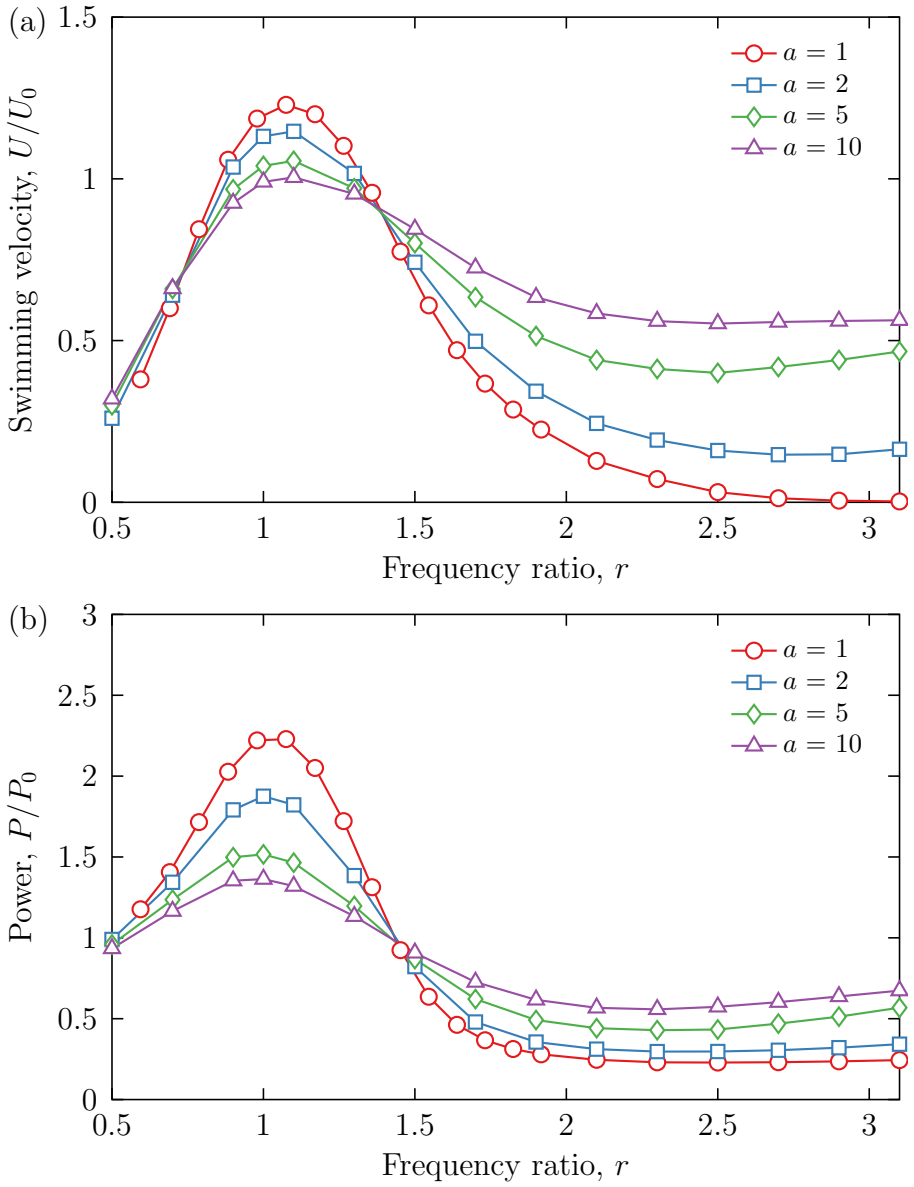

Figure 30: (a) Swimming velocity and (b) input power for tapered rectangular swimmers. Tapered swimmers exhibit less swimming velocity variation with frequency than uniform swimmers.

$r = 1.5$. For uniformly thick swimmers, this power decrease is almost 10 times, while for $a = 10$ the power decreases only about 2 times.

The swimming economy ε quantifies how the swimmer translates the input power into forward swimming velocity. In Figure 31, we plot the swimming economy as a function of frequency ratio for different taper ratios. The most interesting observation

is that the swimmer with $a = 10$, the highest taper ratio, is the most economical for all frequencies in the studied range. The higher economy is also the most pronounced at the higher frequency range past $r = 1.5$. In this range the economy of the uniform swimmer again drops to nearly zero (because the velocity goes to zero), while the swimming economy of both swimmers with $a = 5$ and $a = 10$ stay near its maximum. Our results indicate that in free swimming, tapered swimmers exhibit wide-band high economical performance.

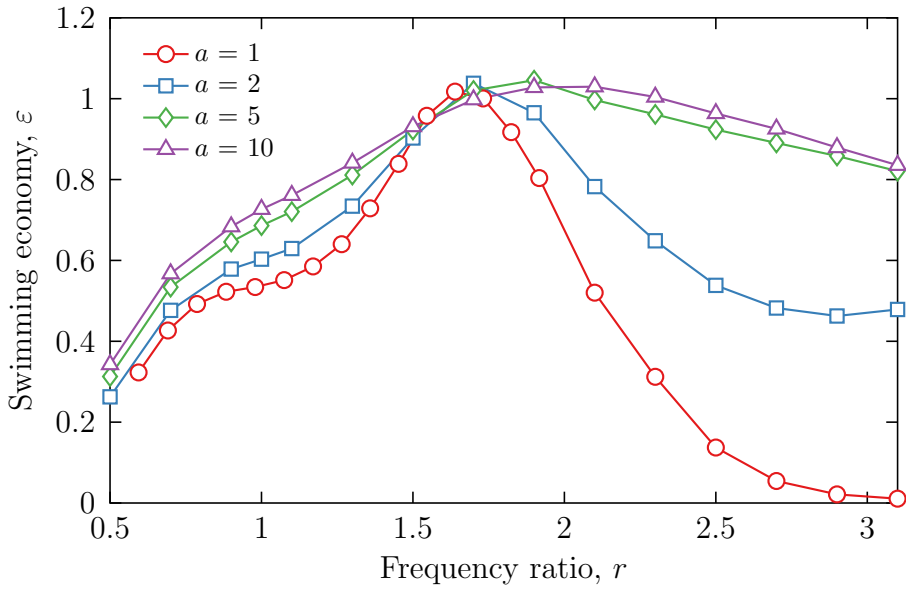

Figure 31: Swimming economy as a function of frequency ratio r for tapered rectangular swimmers. Tapered swimmers exhibit high economical performance for a large range of frequency ratios above $r = 1.5$.

In order to explain this observed wide-band economical performance of tapered swimmers, we first examine the amplitude of the TE displacement, which is shown as a function of r in Figure 32. Generally for a larger TE displacement, more fluid is displaced backwards, which creates more thrust. The graph shows that the TE displacement maximizes slightly higher than the first natural frequency which is consistent with the maximum velocity curves, and this holds for all values of a. What is interesting is that at the frequencies above $r = 1.5$, the TE displacement for swimmers with higher a remain large, while for a uniform swimmer the displacement approaches

1 (equal to the plunging amplitude).

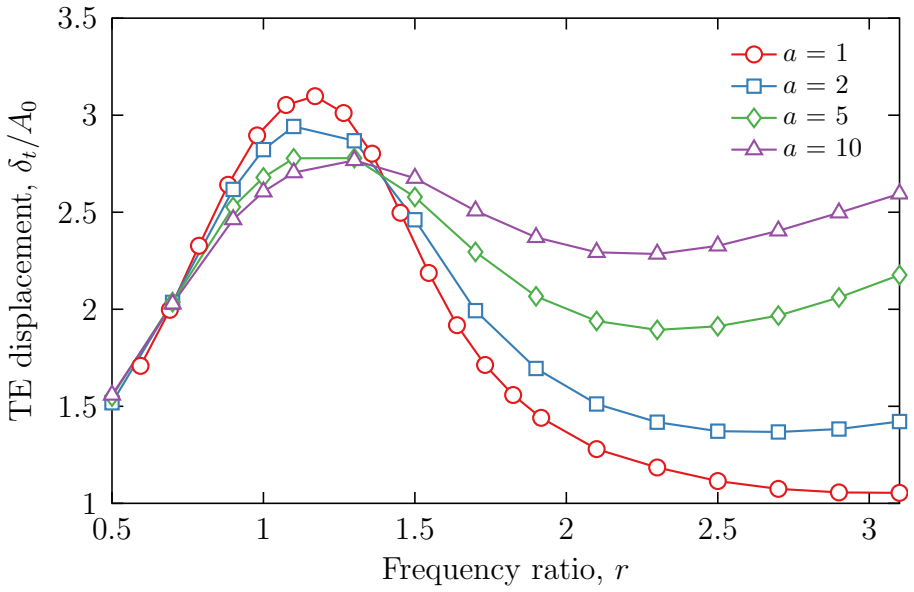

Figure 32: Trailing edge displacement as a function of frequency ratio r. At higher frequencies, tapered swimmers have larger TE displacements, while that of uniform swimmers approach the plunging amplitude.

5.2.2 Tapered Rectangular Swimmer Bending Patterns

To illustrate and compare the deformation of the swimmers at different frequency ratios and taper ratios, we plot the bending patterns for 4 different cases as shown in Figure 33. We consider taper ratios of $a = 1$ and 5 at frequency ratios $r = 1.1$ and 3.1. The bending patterns are instantaneous snapshots of the swimmer position during one stroke period. Comparing the bending patterns for the two cases at $r = 1.1$ near resonance, in Figures 33a and 33b, we observe qualitatively very similar bending patterns. Indeed, when we compare the swimming performance at $r = 1.1$ in terms of the various metrics from Figures 30 and 31, the overall behavior and performance is similar. In contrast, the bending patterns for $r = 3.1$, away from resonance (Figures 33c and 33d), are markedly different. The bending pattern for the tapered swimmer exhibits considerably larger curvature near the trailing edge, which leads to the observed larger TE displacement (Figure 32). The larger curvature also

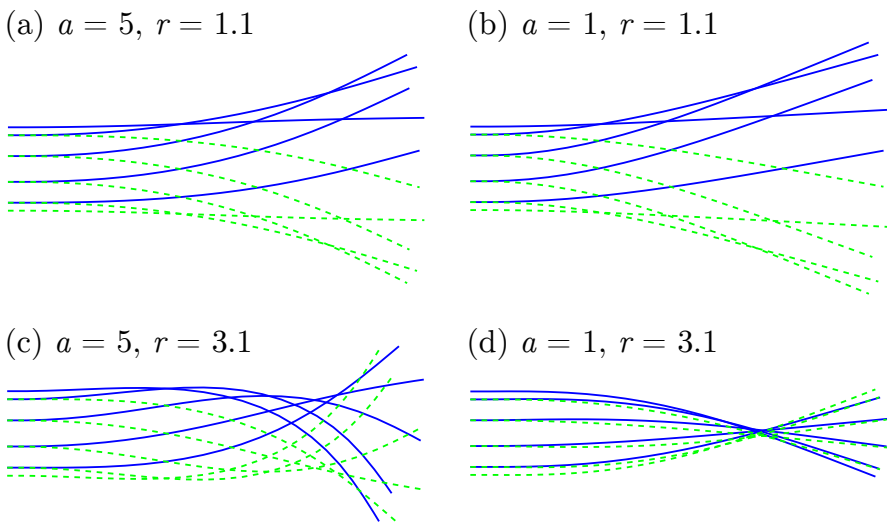

Figure 33: Bending patterns for tapered and uniform swimmers with values of a and r labeled as such. Tapered and uniform swimmers have similar bending patterns at $r = 1.1$, but the tapered swimmer exhibits larger curvature near the trailing edge for $r = 3.1$, resulting in sustained forward swimming at higher frequencies.

creates greater asymmetry in the swimming stroke which creates net thrust, allowing for forward swimming. For the uniform swimmer at $r = 3.1$, the TE displacement is nearly equal to the the LE displacement, so a similar amount of fluid is displaced to either side of the swimmer during a single stroke. Therefore, little to no net thrust is generated by the uniform swimmer at this particular frequency ratio, so the swimmer cannot move forward. As we will discuss below, the cause of the larger curvature in the tapered swimmer is directly related to the large gradients in bending rigidity that result from the tapered geometry.

5.2.3 Characteristics of Tapered Euler-Bernoulli Beam

In order to explain the observed larger curvature in the tapered swimmer, we first seek to understand the effect of tapering on an Euler-Bernoulli cantilever beam vibrating in a vacuum. We can readily derive the mode shapes, whose solutions are given in Appendix A. A mode shape is the dominant contribution to the beam deflection when actuated near the respective natural frequency and is therefore nearly proportional

to the actual deflection.

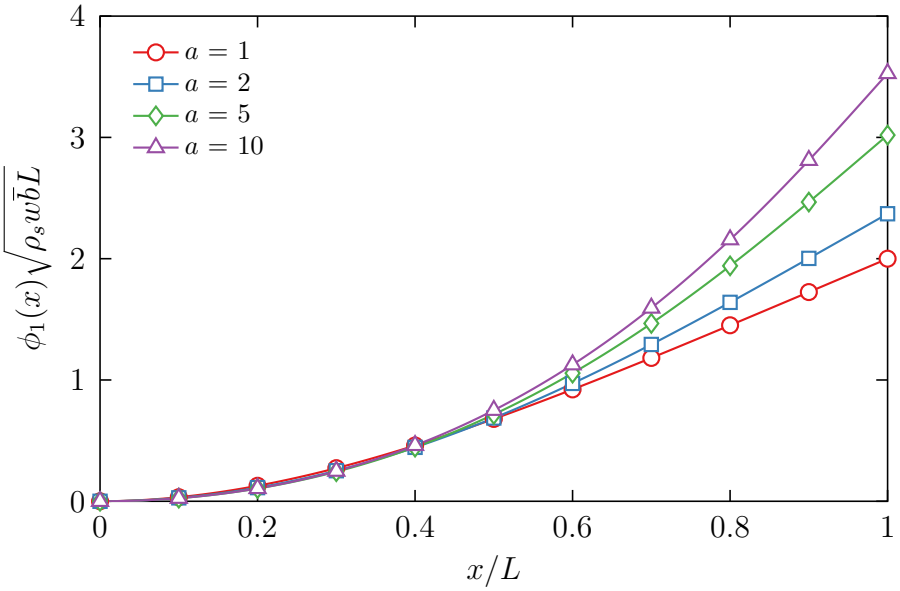

Figure 34: Mass-normalized first mode shape of tapered Euler-Bernoulli beam with different values of a. The mode shapes for the tapered beam have larger curvature near the free end.

In Figure 34, we plot the non-dimensional mass-normalized first mode shapes (see Appendix A) for taper ratios $a = 1, 2, 5, 10$. Qualitatively, the mode shapes behave similarly — all are monotonically increasing along the length until an expected maximum at the trailing edge. The tapered beam appears to have a larger curvature, which leads to a larger value at the free end. This is confirmed in Figure 35a, where we plot the normalized second derivative of the mode shape, which approximates the curvature, along the beam length. We find that as the taper ratio a increases, the maximum curvature both increases and shifts toward the end of the beam.

In Figure 35b, we plot the normalized moment along the beam length, which is the product of the curvature with the bending rigidity $EI(x)/EI_u$, normalized by the bending rigidity of the uniform beam. We find in all cases, the moment decreases along the length, despite the increasing curvature. The reason is that bending rigidity for a beam with a large taper ratio decreases cubically, so a small local moment can induce a large local curvature. In order words, the tapered beam experiences larger

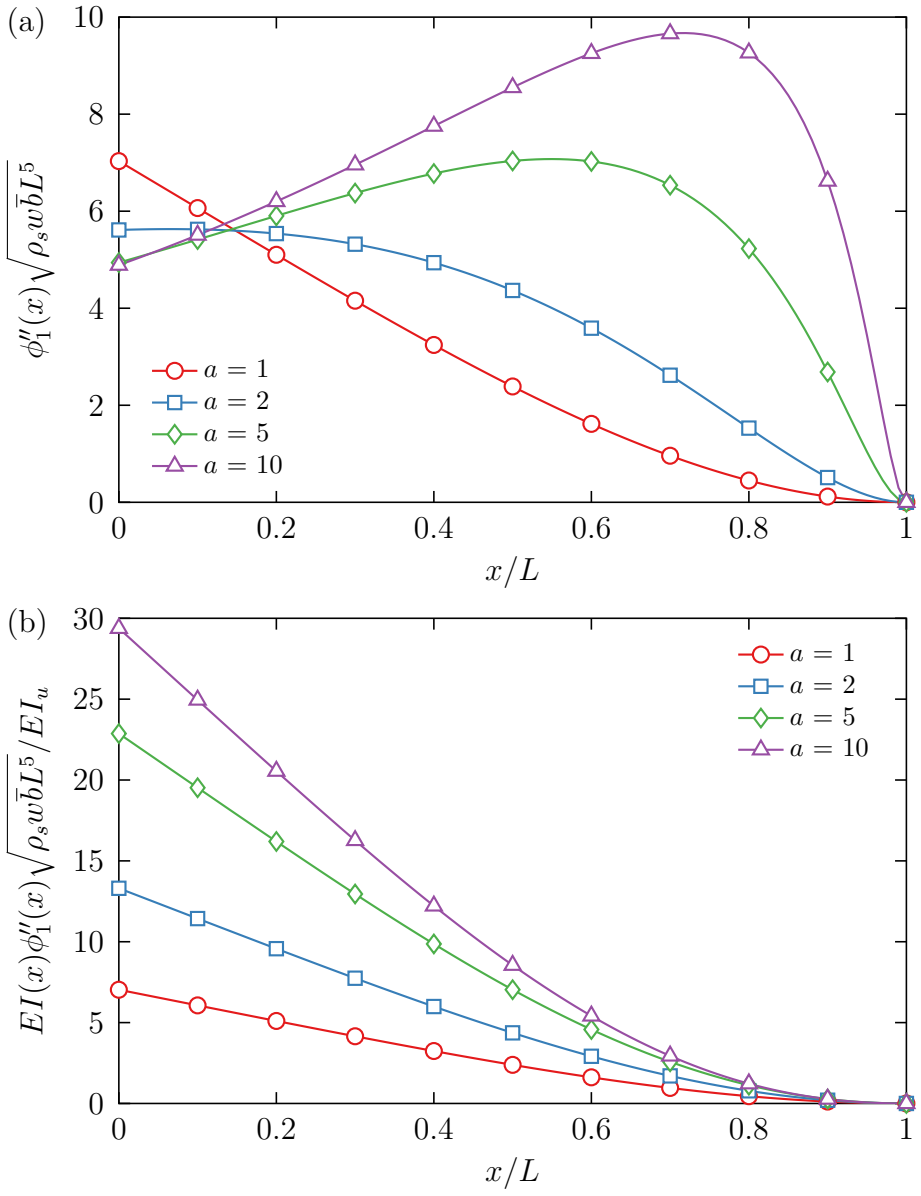

Figure 35: (a) Normalized curvature and (b) moment of tapered Euler-Bernoulli beam first mode. Curvature near the free end increases with increasing a, but moment curves near the free end have similar values.

deflections near the free end because of a locally higher curvature caused by the cubically decreasing bending rigidity.

5.2.4 Curvature and Moment of Tapered Rectangular Swimmer

The tapered swimmer deflection cannot be directly compared to the tapered beam results from Figures 34 and 35 because of the fluid coupling, geometric non-linearity,

and different LE boundary conditions, but we demonstrate that similar physics dictate the swimmer deformation and lead to observed results from Figures 30 and 31. In Figures 36a, we plot the curvatures at the instant of maximum deflection for the 4 cases shown in Figure 33. The curvatures $\kappa(x)$ were computed using a central difference approximation of $\kappa(x) = z''(x)/[1 + z'(x)^2]^{3/2}$, where $z(x)$ is the swimmer displacement at an instant of time. We find that for the tapered swimmers at both $r = 1.1$ and 3.1, the curvatures are maximized farther toward the trailing edge of the swimmer than those of the uniform swimmers. Furthermore, the tapered swimmer at $r = 3.1$ exhibits the largest maximum curvature at approximately $x/L = 0.6$, which is interesting because it is actuated far from resonance.

Figure 36b shows the local moment along the length of the swimmers. For the near-resonance cases with $r = 1.1$, we see that the moment curves are nearly overlapping, especially near the trailing edge, but the tapered beam exhibits almost 3 times more curvature at $x/L = 0.6$. However, the tapered and uniform swimmers exhibit a similar bending pattern and TE displacement because the uniform swimmer has larger curvature near the LE. For the $r = 3.1$ cases away from resonance, we also observe approximately a 3 times increase in curvature at $x/L = 0.6$ in the tapered swimmer despite a modest increase in moment. Unlike the swimmers near resonance, the larger curvature leads to considerably larger TE displacement compared to uniform swimmers at the same frequency ratio.

As we had observed in the mode shape analysis, the larger local curvature near the TE is directly related to the significantly smaller local bending rigidity resulting from the tapered geometry. Thus, for tapered swimmers, large deformations can be sustained at a wide range of frequency ratios because there is always a larger curvature (at maximum deformation) near the TE compared to uniform swimmers. The larger curvatures appear to create significant deformations at post-resonant frequencies. These larger deformations lead to sustained high swimming velocity at a wide

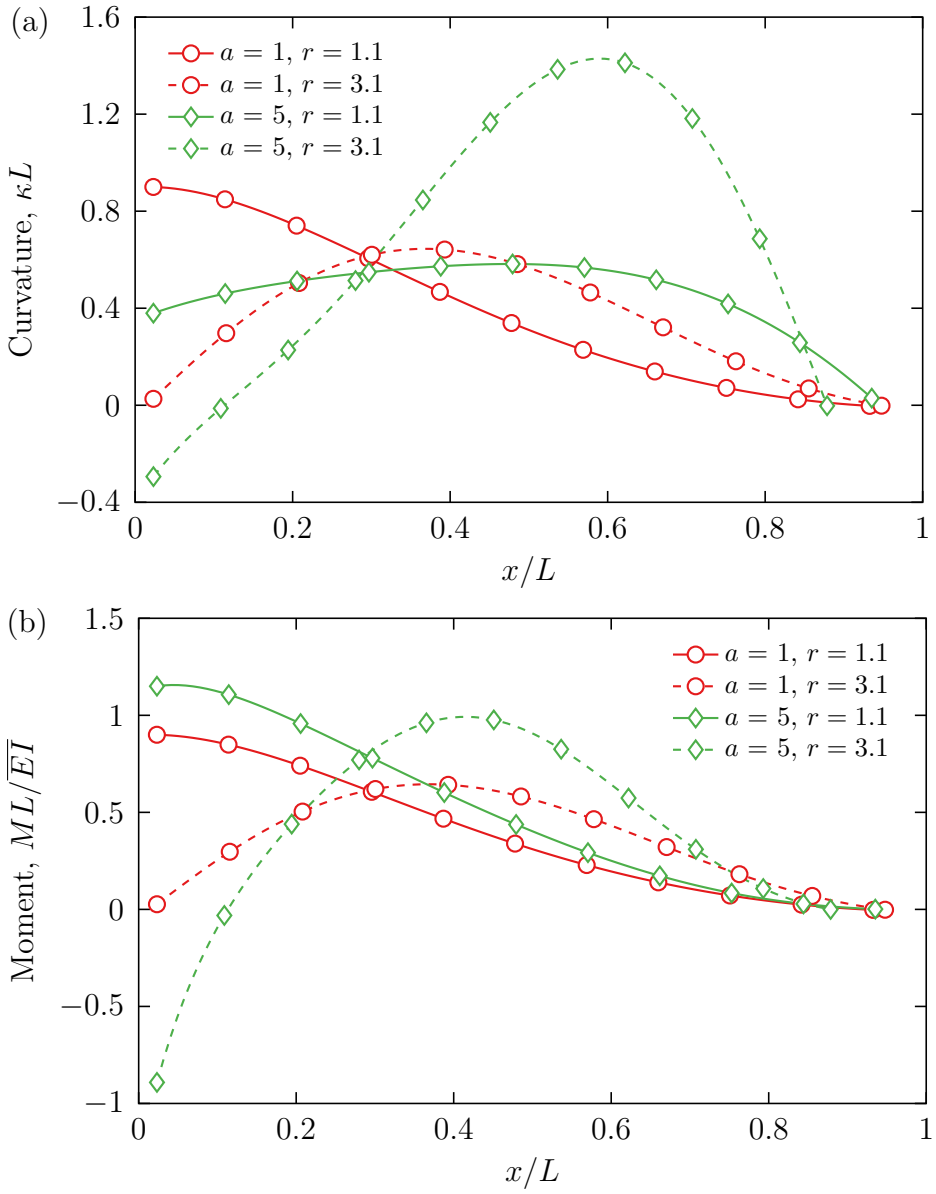

Figure 36: (a) Curvature and (b) moment profiles for the swimmers highlighted in Figure 33. The tapered swimmers exhibit larger curvature further down the length at $x/L = 0.6$. At this same length, moment is only slightly increased.

frequency range post-resonance for tapered swimmers while uniform swimmers must tune to specific frequencies or risk stalling.

We have explained the observed wide-band sustained thrust and swimming velocity curves at post-resonant frequencies for tapered swimmers. In order to explain the associated wide-band swimming economy (Figure 31), we also must examine the

cause of the lower power requirements at post-resonant frequencies. This may be explained by examining the external force amplitude at the leading edge. In Chapter 3, we had found that the external force and LE velocity time histories were nearly in phase, so the power was roughly proportional to the external force amplitude. Also, we had determined that the minimum external force amplitude led to more efficient swimming because the swimming stroke consisted of the front half and back half of the swimmer moving in opposite directions out of phase.

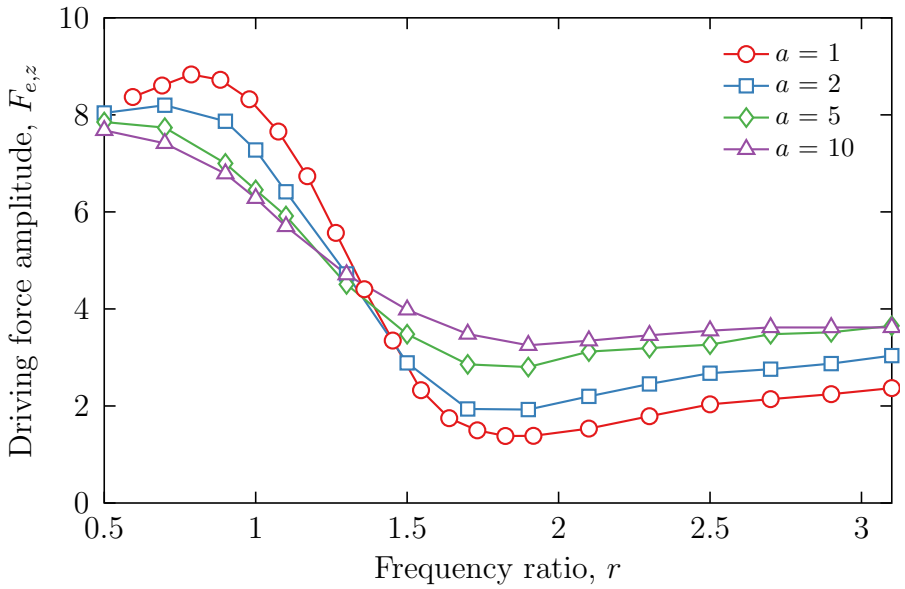

Figure 37: Driving force amplitude as a function of frequency ratio. Driving force is minimized at approximately $r = 1.7$ to 1.9, corresponding to that of maximum swimming economy. This trend is consistent with results in Chapter 3.

In Figure 37 we plot the amplitude of the external force at the LE as a function of r. We find that the force is minimized at approximately $r = 1.7$ to 1.9 for each value of a, which correspond to the maximum swimming economy (Figure 31). Furthermore, the external force stays relatively low and slowly increases with r past $r = 1.7$. This occurs because the LE and TE are moving in opposite directions for $r > 1.7$ and a similar bending pattern (Figure 33c) is maintained. We find that the power is slightly higher for tapered swimmers with higher a because the deformation is larger, creating more dissipation. Despite the larger power requirements for the tapered swimmers,

the sustained thrust generation at higher frequencies is enough to overcome the losses, so swimming economy is sustained at these higher frequencies.

5.2.5 Performance Characterization of Tapered Trapezoidal Swimmer

In addition to the rectangular tapered swimmer, we assess the performance of a trapezoidal tapered swimmer. Results from Chapter 4 showed that for uniformly thick trapezoidal swimmers, all cases showed similar speed and swimming economy, suggesting that the trapezoidal geometry does not significantly affect performance. Here, we combine the trapezoidal geometry with tapering. Because of the trapezoidal geometry, the mass and stiffness distribution per unit length are no longer linear and cubic, respectively, with length. It is unclear then how the different material properties affect swimming performance. We study the performance of tapered, trapezoidal swimmers with length ratios $w_R = 0.25, 1, 4$ with a taper ratio of $a = 5$.

The swimming velocity for tapered trapezoidal swimmers as a function of frequency ratio is shown in Figure 38a. For comparison, we also include the results for the uniformly thick trapezoidal swimmers from Chapter 4 as dashed lines. The swimming velocity shows trends that are common to both trapezoidal geometry and tapering effects. Like the $a = 1$ trapezoidal swimmers, the tapered ones have swimming velocities that are similar, deviating by less than 20% near $r = 1$. At higher frequencies, all three tapered swimmers sustain velocities higher than uniform ones, and the velocity of the narrowing swimmer is nearly double that of the widening swimmer. We attribute this to the tapering effect, similar to what was found in Figure 30a. Because one-dimensional bending (even for a plate) depends on EI, which is proportional to width, the narrowing swimmer has a softer trailing edge than the widening swimmer, so the narrowing swimmer has a larger effective taper ratio, which leads to faster swimming speeds at post-resonance frequencies. In Figure 38b, we plot the power as a function of frequency ratio. Similarly, the power curves

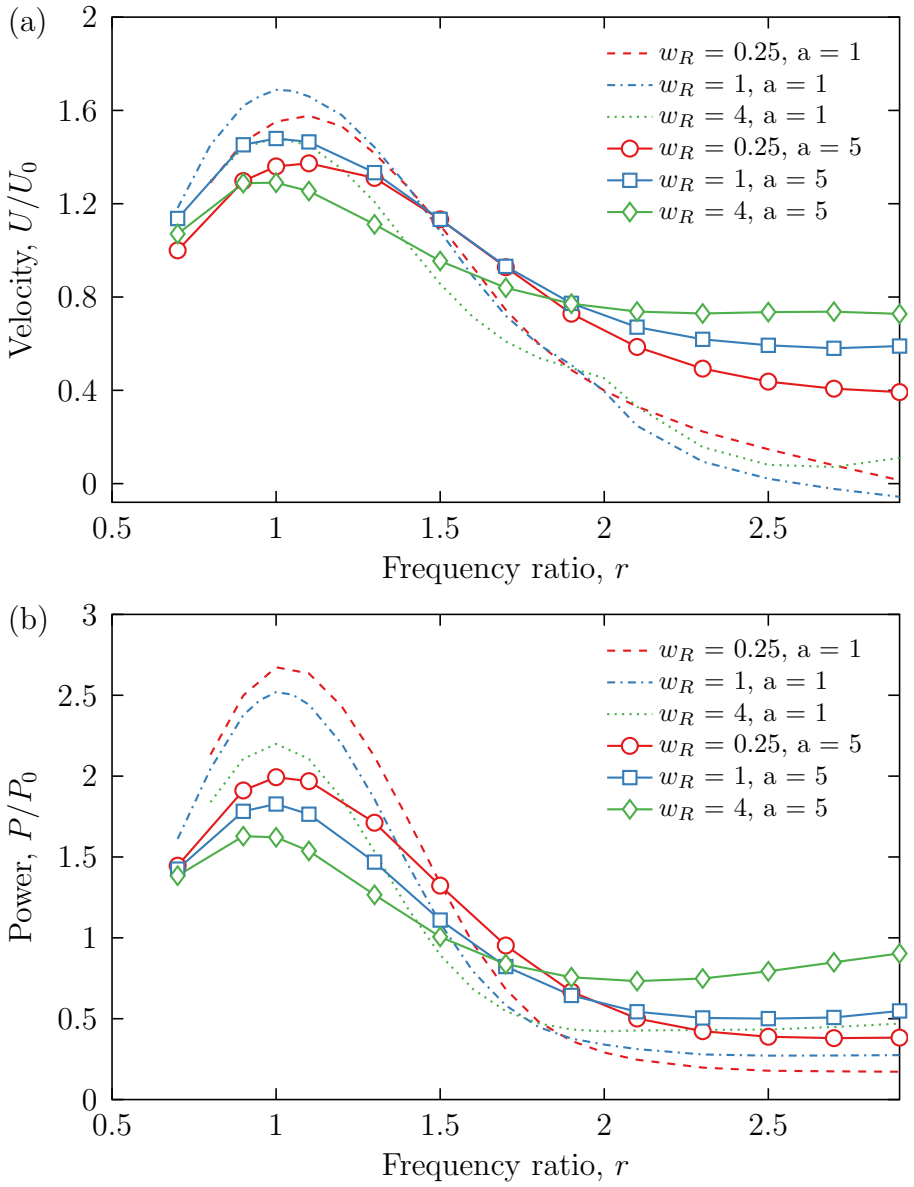

Figure 38: (a) Velocity and (b) power for tapered trapezoidal swimmers with $a = 5$ and $w_R = 0.25, 1, 4$. Broken lines indicate uniformly thick trapezoidal swimmers for comparison. Both the velocity and power exhibit trends common to both a tapered rectangular swimmer and a trapezoidal uniformly thick swimmer.

exhibit trends common to both uniformly thick trapezoidal swimmers and tapered rectangular swimmers (Figure 38b). $w_R = 0.25$ has the largest power near $r = 1$ by a small amount, but for all cases the power decreases to a steady smaller value at higher frequencies.

The swimming economy for tapered trapezoidal swimmers is shown in Figure 39.

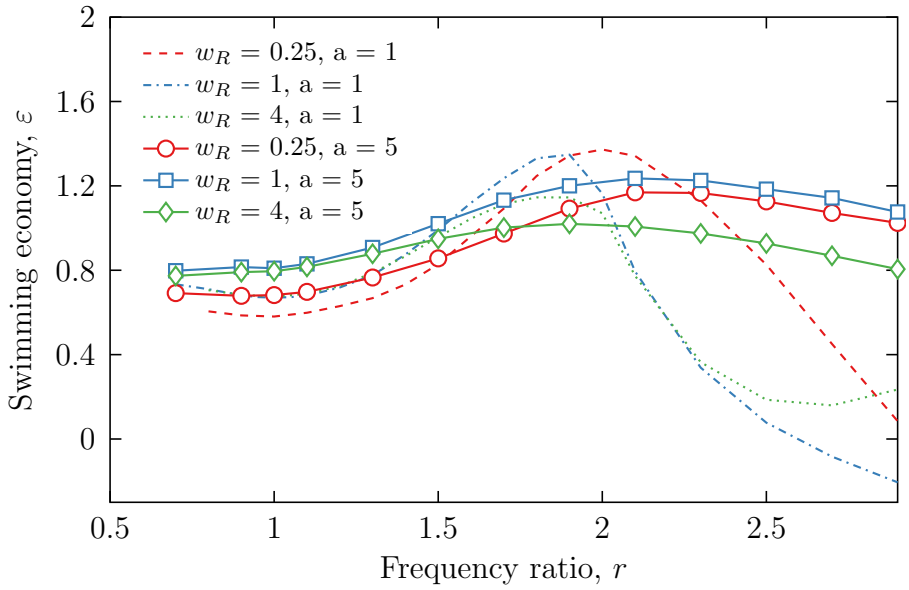

Figure 39: Swimming economy curves for tapered trapezoidal swimmers. Tapered trapezoidal swimmers exhibit sustained high swimming economy at post-resonance frequencies compared to uniform trapezoidal swimmers.

Just as for tapered rectangular swimmers (Figure 31), the swimming economy for all tapered trapezoidal swimmers remains consistent over a wide range of frequency ratios and does not deviate more than 40% of the maximum value. In contrast, the uniformly thick trapezoidal swimmers experience a large decrease in ε at higher frequencies about $r = 2.1$. It is also interesting that the rectangular tapered swimmer is most economical, but the other trapezoidal swimmers have close values for economy at all frequencies.

Evidently, the trapezoidal geometry for tapered swimmers does not affect the performance significantly. When comparing the trapezoidal tapered swimmers between different width ratios, their resulting performance is similar as we observed in Chapter 4. The tapered trapezoidal swimmers compared to their uniformly thick counterparts exhibit the same wide-band economical performance at post-resonance frequencies as found for rectangular swimmers. The swimming performance is affected more significantly by the tapering thickness than by changes in shape because the one-dimensional bending stiffness EI is proportional the cube of thickness while

only proportional to width.

5.3 Summary

In this chapter we studied the swimming performance of oscillating flexible plate swimmers with a tapered thickness inspired by tapering of real fish fins. The plate thickness varied linearly from the thickest portion at the leading edge to the thinnest at the trailing edge. We found for both rectangular and trapezoidal swimmers, the tapered swimmers achieved moderate swimming speeds approximately half of their maximum speeds even at higher frequency ratios, while the uniformly thick swimmers had velocities that dropped to nearly zero. We showed that this was a result of the larger curvature observed near the trailing edge which arises because the plate stiffness varies cubically along the plate length.

The input power is lower at higher frequencies because the driving force amplitude is lower, and combined with moderate swimming velocities, the tapered swimmer achieves a high swimming economy at a large range of frequency ratios post-resonance. Tapered swimmers have an advantage over uniform swimmers because the tapered swimmers do not need to be tuned to near-resonant frequencies in order to avoid the potential for zero thrust production at higher frequencies.

The dominant effect on tapered trapezoidal swimming performance is from the tapered thickness, not the trapezoidal geometry, and tapered trapezoidal swimmers exhibit characteristics common to both tapered rectangular swimmers and uniformly thick trapezoidal swimmers. The trapezoidal geometry leads to small differences between performance based on width ratios because a widening and narrowing swimmer have different effective taper ratios.

CHAPTER VI

FREE SWIMMING OF INTERNALLY ACTUATED OSCILLATING PLATES

6.1 Introduction and Computational Setup

Thus far, we have studied the performance of swimmers that were passively actuated at the leading edge. We established a baseline understanding for a uniformly thick plate with aspect ratio $AR = 2.5$, and studied the effects of shape change and tapered thickness. In this chapter we study the performance of an internally actuated swimmer that has both active and passive portions, which models a robotic fish-like fin driven by a smart material with a passive attachment. We show in our simulations that the addition of a passive attachment increases both swimming velocity and efficiency. Specifically, if the active and passive sections are of similar size, the overall performance is the best. We determine that this optimum is a result of two competing factors. If the passive section is too large, then the actuated portion is unable to generate substantial deflection to create sufficient thrust. On the other hand, a large actuated section leads to a bending pattern that is inefficient at generating thrust especially at higher frequencies.

As discussed in Chapter 1, internally actuated (smart) materials, such as ionic polymer-metal composites (IPMCs), shape memory alloys (SMAs), and piezoelectric actuators, can be adapted to follow fish-like motions without the complexity of motor-based designs. In particular, piezoelectric actuators are scalable, efficient, and noiseless and thus represent an attractive option for a fish-like propulsor design.

Macro fiber composites (MFCs) [127–129] are a new class of piezoelectric actuators that have been recently used and tested in small-scale aquatic propulsors [130–132].

MFCs offer large dynamic stresses in bending and high performance at low and high frequencies. The thrust performance of MFCs as piezoelectric biomimetic actuators was recently investigated by Erturk and Delporte [132]. In this study, the authors fabricated MFC bimorph actuators, which are two MFC laminates bonded together by a thin layer of epoxy. When oppositely signed electric fields are applied to the different layers, one stretches and the other contracts, creating bending. Thus, these flexible MFC bimorph actuators are driven by oscillating internal moments. The thrust generation of the MFC bimorph cantilevers was subsequently measured experimentally. Furthermore, these MFC bimorphs were also recently used to build an untethered swimming device that resembled a robotic fish [130]. The MFC bimorph acted as the fins, providing oscillating flexible propulsion. A waterproof "body" housed the electronics that powered the bimorphs, allowing for unrestricted movement within a fluid.

In addition, Erturk and Delporte probed the effect of a passive caudal fin attachment by comparing thrust with and without the passive fin [132]. It was found that the passive fin attachment introduced an additional bending mode in the same frequency range, leading to wideband thrust generation. Furthermore, the thrust amplitude was higher for the cantilever beam with a passive attachment. These results suggest that active, internally-actuated fins with and without passive attachments behave differently and that a particular combination of active and passive sections may lead to optimal swimming performance. Thus, the purpose of our study is to use computational simulations to systematically study the performance of biomimetic swimmers with active (*via* internal moment) actuation with a passive attachment and to identify the physical mechanisms that enhance the swimming performance of the composite active-passive fins.

We briefly discuss the computational model here as the details are given in Chapter 2. Our model actuator is shown in Figure 40a. The active fin is modeled as a flexible

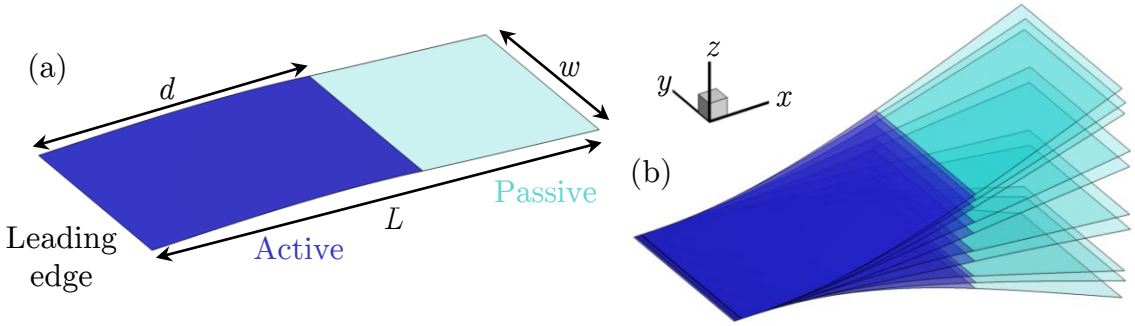

Figure 40: Schematic of internally actuated flexible plate with passive attachment. (a) Geometry of plate showing the dimensions and size of the active portion (darker shade) and passive portion (lighter shade). (b) Oscillating internal moment in the active section leads to asymmetric bending patterns that generate propulsion.

plate of uniform bending stiffness with total length L, width w, and thickness b, which is small compared to the length ($b \ll L$). The aspect ratio L/w is 2.5. The plate is segmented into two sections. First, an internally actuated section, called the active portion (shown in a darker shade), extends a distance d from the leading edge. Beyond that, a passively responding tail section (the passive portion, lighter shade) is attached. Both sections have the same isotropic material properties. The active portion actuates the swimmer using a sinusoidally oscillating internal moment, $M(t) = M_0 \sin(\omega t)$, uniformly distributed within the active portion. Here, ω is the driving frequency, and M_0 is the amplitude of the applied moment. This actuation pattern mimics that of an oscillating bimorph MFC composite [130]. We set the reduced moment $M_0' = M_0/\rho_s b U_0^2 w L = 0.176$.

The leading edge vertical displacement and slope are both kept at zero (clamped in the z–direction), but the plate is allowed to swim forward horizontally. The clamped boundary condition mimics an oscillating fin attached to a power housing with a large enough mass to prevent leading edge deflection. The goal of our study is to investigate the effects of adding the passive elastic attachment on the steady state swimming velocity. To isolate these effects, we hold constant the total length of the swimmer

and vary the size of the active portion. The plate is driven at constant frequency, but its stiffness is varied. Depending on the proximity to resonance, different bending patterns emerge that lead to faster or slower swimming velocity.

6.2 Results and Discussion

6.2.1 Swimming Velocity

The goal of the study is to understand how the swimming performance is affected by the size ratio between the active and passive sections while keeping the total length of the plate constant. In addition, we investigate the bending patterns that arise from varying its bending rigidity. We focus on the regime near the first natural frequency where resonance amplification results in the larger deflections and faster swimming.

For plates with different values of d/L, we sample the range of frequency ratio ϕ between 0.8 and 2.0 and compute the period-averaged velocity U after the swimmer reaches a steady state. We plot our results of U/U_0 vs. ϕ in Figure 41, where different lines indicate different values of d/L. We find that the swimming velocity is maximized in the vicinity of the first natural frequency for each case of d/L. Indeed, the resonance oscillations near the first natural frequency are linked to faster swimming (see Chapter 2). Furthermore, the maximum swimming velocity is found to be roughly the same for all cases, except for that of $d/L = 0.2$. This is surprising, as the fully actuated plate is not the fastest and is even slightly slower than the plate with $d/L = 0.6$ when comparing their maximum speeds. At a higher frequency ratio of $\phi = 2.0$, the discrepancy is even more pronounced with the velocity at $d/L = 0.6$ about five times that of $d/L = 1$. At higher frequency ratios, having a passive section appears to dramatically enhance the swimming performance. We conclude that at all post-resonance frequencies, the plates with passive attachments (of size ratios $d/L = 0.4$ to 0.6) achieve either equal or better performance than a fully actuated plate with the same total length.

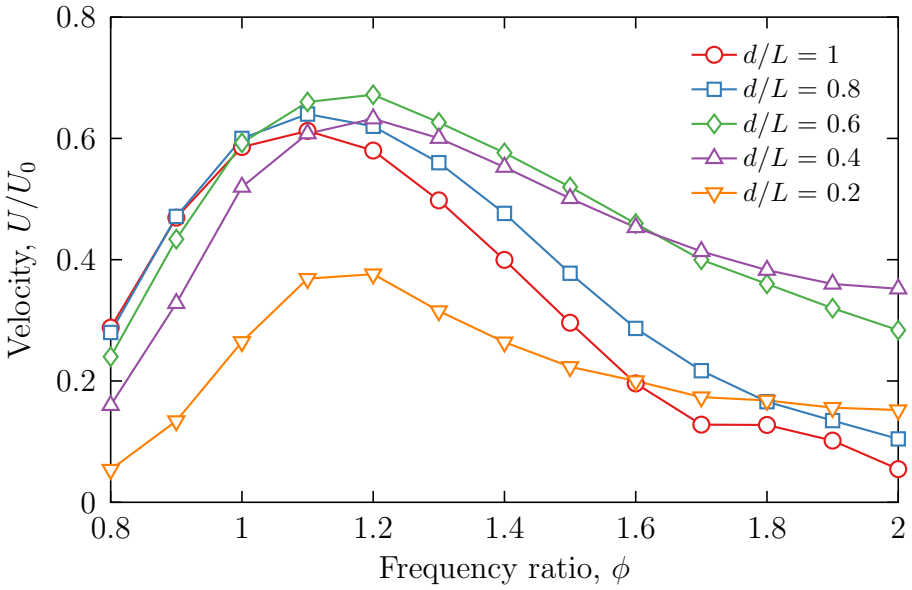

Figure 41: Dimensionless swimming velocity as a function of frequency ratio. Velocity is maximized near the first natural frequency for all active section sizes. At higher frequencies, the plate with either $d/L = 0.4$ or 0.6 achieves the fastest swimming speeds.

To identify the physical mechanism that allows the passive flap to enhance the swimming velocity, we first examine the trailing edge deflection amplitude, δ_t. A larger trailing edge deflection is usually correlated to faster swimming (see Chapters 3, 4, and 5). In Figure 42a, we plot δ_t/L as a function of frequency ratio ϕ. The data shows that, similar to swimming velocity, δ_t/L is also maximized near the first natural frequency, and the deflection amplitudes are nearly the same besides a lower amplitude for $d/L = 0.2$. The similar trends between trailing edge deflection and velocity in the resonance regime suggest that a larger deflection leads to faster swimming. This does not hold, however, at higher frequencies when the trailing edge displacement is still nearly the same, but the plates with passive attachments are significantly faster than the fully actuated one.

To explore the correlation between trailing edge deflection and swimming velocity, we graph the velocity as a function of deflection in Figure 42b. We find that in general, the larger the trailing edge deflection, the larger the swimming velocity. For plates

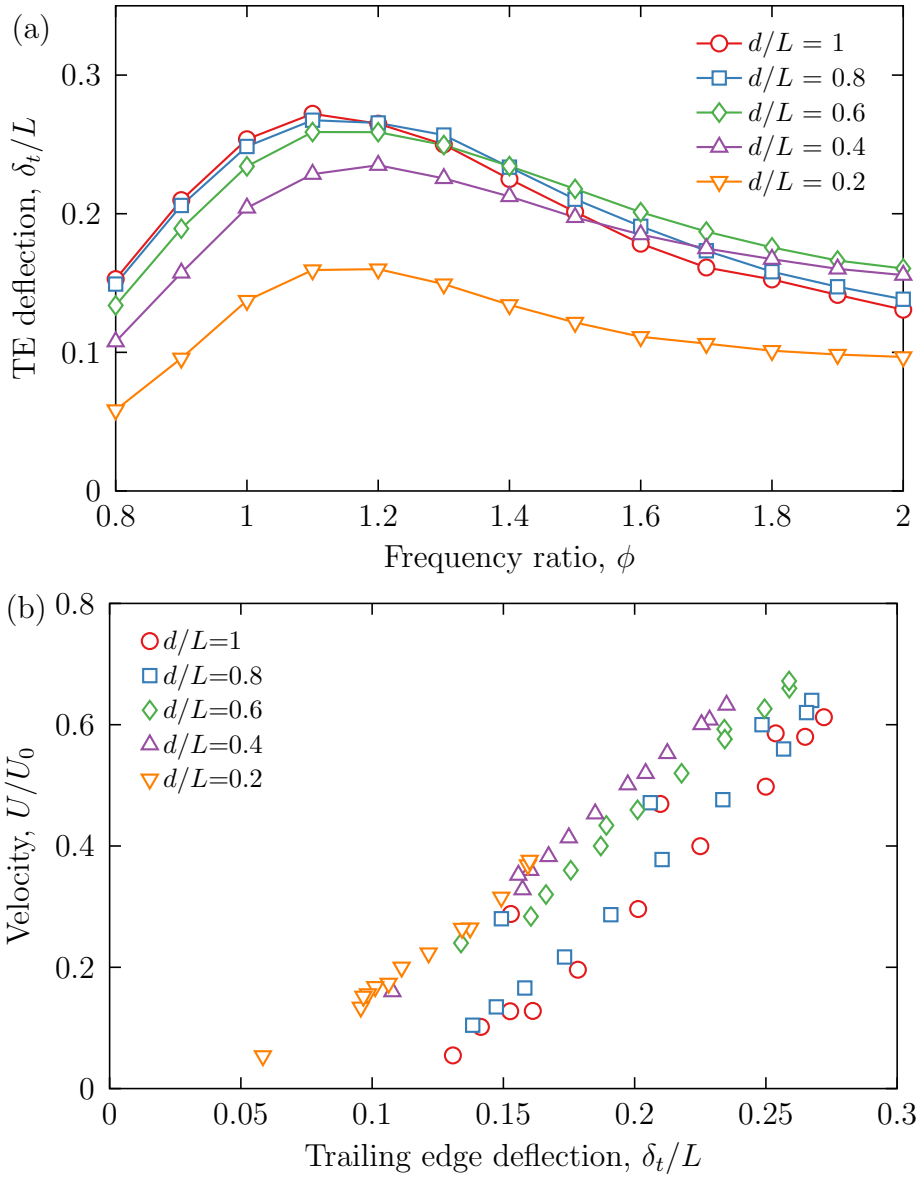

Figure 42: (a) Trailing edge deflection as a function of frequency. Despite higher velocity at higher frequencies for $d/L \geq 0.4$, trailing edge deflection remains nearly the same for these swimmers and fully actuated swimmer with $d/L = 1$. (b) Velocity vs. trailing edge deflection, showing that in general a larger trailing edge deflection implies faster swimming.

with spatially similar bending patterns, one with larger trailing edge amplitude would create a larger momentum flux behind the swimmer and, thus, generate more thrust.

This explains the poorer performance of the $d/L = 0.2$ plate. The moment is

applied near the leading edge, far away from the trailing edge, and as such is unable to oscillate the larger passive portion with sufficiently large amplitude compared to plates with larger active sections. Despite the general correlation of larger displacement with faster swimming, Figure 42b shows that for the same trailing edge amplitude, the velocity can also vary significantly and can change up to three times. The slower velocities correspond to fully active plates at higher frequency ratios. These observations suggest that the addition of a passive section affects the bending patterns of the fin which significantly alters the swimming performance.

6.2.2 Bending Patterns

In order to characterize the differences in the bending patterns, we examine two cases: $d/L = 0.6$ and $d/L = 1$ both at the frequency ratio $\phi = 2$. The maximum trailing edge displacement differs by no more than 20%, but surprisingly, the fully actuated plate is nearly 5 times slower. In Figure 43a, we plot the time evolution during one period of the non-dimensional internal moment $M'(t)$, trailing edge deflection, $\delta_t(t)/L$, and trailing edge angle, $\alpha_t(t)/L$. We find that the deflection curves (the solid lines with symbols) for both cases are in phase, which is expected because the frequency ratio is the same. The deflection amplitudes are confirmed to be about 20% apart. Also, the deflection curves are nearly out of phase with the applied moment, which again is expected because the frequency ratio is higher than the natural frequency.

The most pronounced differences between the two cases are in the trailing edge angle curves. For $d/L = 0.6$, the faster plate, the trailing edge angle (dotted line) is found to be in phase with the corresponding deflection. In contrast, the trailing edge angle for $d/L = 1$, the poorer performer, is out of phase with the deflection. The bending patterns are visualized in Figures 43b for $d/L = 1$ and 6c for $d/L = 0.6$ as snapshots of the instantaneous deflection curves during one period. In Figure 43b, the trailing edge angle and deflection are out of phase, so when the deflection is

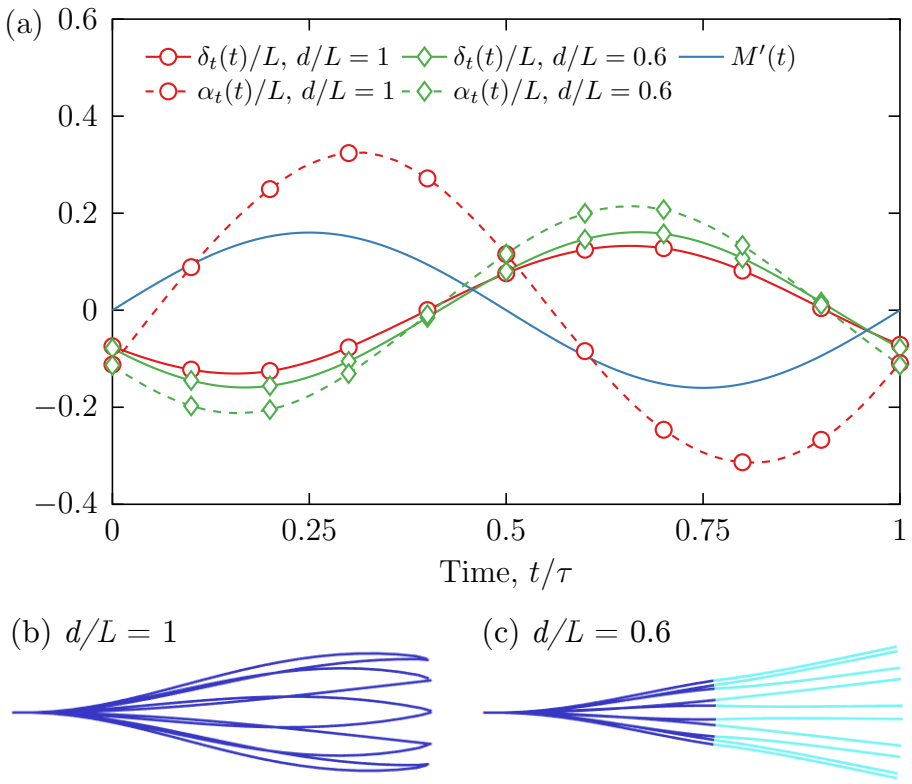

Figure 43: (a) Time history of trailing edge kinematics for plates with $d/L = 1$ and $d/L = 0.6$ at $\phi = 2$. Note that the trailing edge deflection and angle are out of phase for $d/L = 1$. Snapshots of deflection curve are shown for (b) $d/L = 1$ and (c) $d/L = 0.6$. The negative slope at the trailing edge for $d/L = 1$ contributes to loss of swimming performance.

maximized, the angle is negative. The result is a shape that "cups" the fluid, limiting the momentum flux that leads to forward thrust. In contrast, Figure 43c depicts the bending pattern for a plate with a passive attachment. Here, the angle and deflection are in phase, so at the maximum extent of the trailing edge, the angle is positive, leading to a slope that effectively pushes fluid backwards to enhance thrust.

The physical mechanism leading to these bending patterns can be explained by analyzing the actuation mechanism. An internal moment acts to change the local curvature, which in turn affects the slope of the deflection curve. When the plate is fully actuated, the trailing edge exhibits a significant local curvature change because it lies within the actuation region. Thus, we expect that the angle at the trailing edge

responds quickly to the applied moment, i.e. the angle and moment have a small phase lag. Indeed, a smaller phase lag is seen in Figure 43a between the moment and angle time histories for $d/L = 1$ compared to $d/L = 0.6$. Thus, for fully actuated plates, at the time of maximum deflection, the internal moment, which is out of phase with deflection, creates the negative trailing edge slope. In turn, this leads to a loss of swimming performance.

The aforementioned effect does not occur with the passive attachment because the internal moment is confined to the active section and does not directly affect the curvature of the passive attachment if the passive section is long enough. Furthermore, this trailing edge curving effect does not occur with lower frequency ratios closer to the natural frequency because the moment, deflection, and angle are all in phase regardless of the size of the active section. Thus, the swimming performance at low frequencies is all rather similar among all swimmers (with the exception of $d/L = 0.2$ whose poor performance is related to small deflection).

To further corroborate our analysis, we plot in Figure 44 the phase $\Delta\theta$ between the trailing edge deflection and angle for multiple simulations. For active sections sized $d/L = 0.6$ and smaller, the deflection and angle stay nearly in phase for all frequency ratios. This bending pattern is correlated with better performance. However, for $d/L = 0.8$ and $d/L = 1$, phase increases with frequency ratio. This suggests that a too small passive attachment allows the internal moment to affect the trailing edge curvature and change the trailing edge angle detrimentally.

Thus, we conclude that that the addition of the passive attachment leads to a better swimming performance at higher frequencies because it suppresses the detrimental curvature at the trailing edge. At lower frequencies, the passive attachment does not affect the swimming performance unless it is too large, in which case the reduced trailing edge deflection suppresses the generation of adequate thrust.

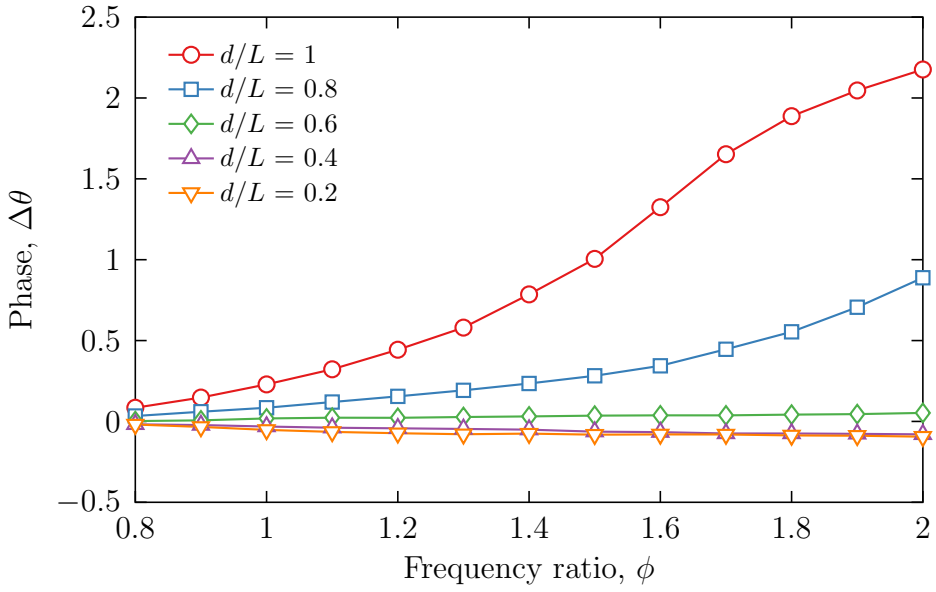

Figure 44: Phase between trailing edge deflection and angle as a function of frequency ratio. The passive flap causes the phase to stay nearly zero in a wide frequency range for $d/L = 0.6$ and smaller, which contributes to better swimming performance.

6.2.3 Power and Swimming Economy

The previous discussion was centered on the swimming speed. Another important parameter for characterizing the swimmer performance is the power consumption. The total input power is calculated in our LSM model as the dot product between the external nodal forces $\mathbf{F}_{M,i}$ and the nodal velocity $\mathbf{v}_i$, summed over all nodes:

$$P = \left\langle \sum_i \mathbf{F}_{M,i} \cdot \mathbf{v}_i \right\rangle. \tag{46}$$

Here, the brackets indicate period-averaging. The power is normalized by characteristic power $P_0 = 0.5\rho U_0^3 wL$ to yield the nondimensional power P/P_0. In Figure 45a, we plot the power as a function of frequency ratio for the different values of d/L. We find that the input power is maximized near the first natural frequency, similar to the trends found for the swimming velocity (Figure 41) and the trailing edge deflection (Figure 42a). We also find that the power increases with increasing d/L, which is expected since the deflection in the active section (and by extension $\mathbf{v}_i$) is smaller when the active section is smaller.

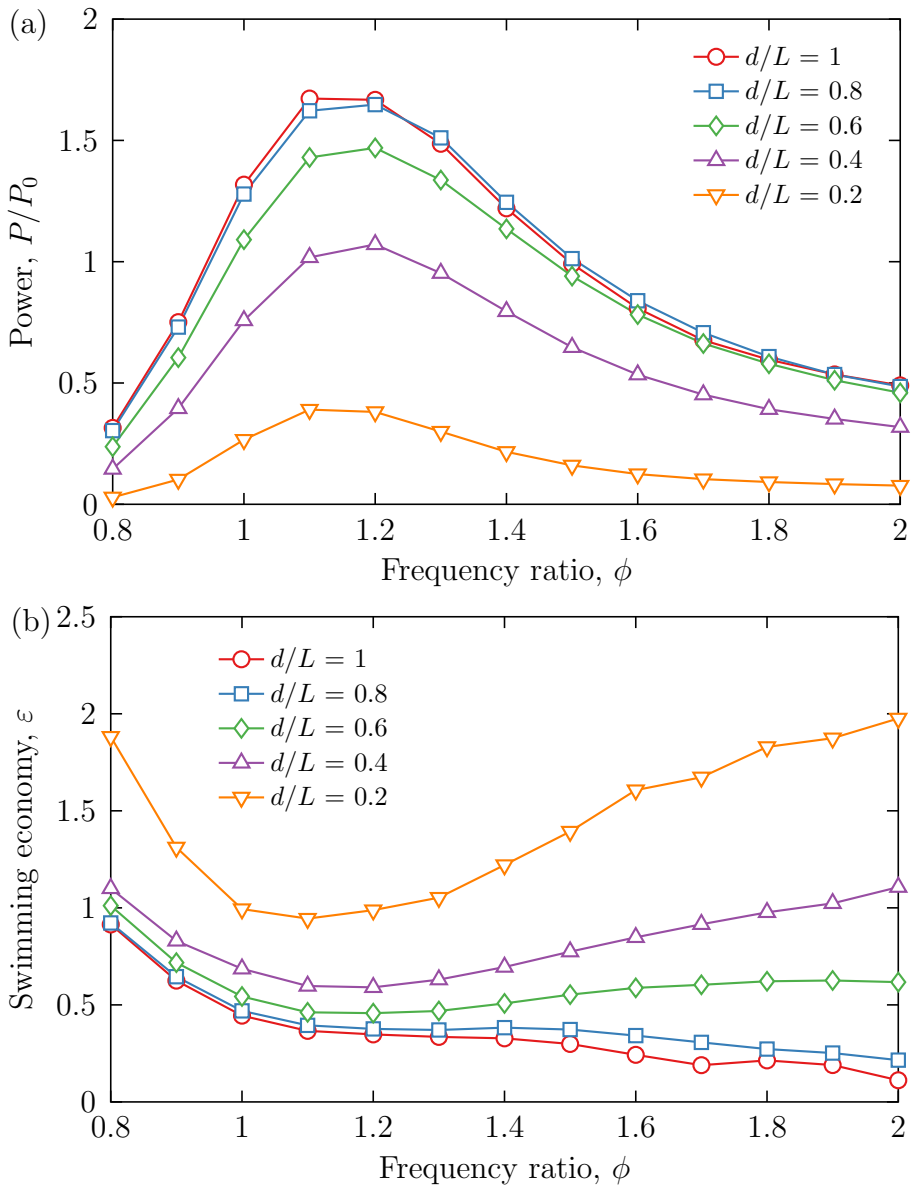

Figure 45: (a) Power and (b) swimming economy as a function of frequency ratio. With decreasing d/L, power decreases while swimming economy increases. Plates with passive flaps exhibit better swimming economy as well as faster velocity.

In Figure 45b, we plot the swimming economy ε as a function of frequency ratio and find that the swimming economy decreases with increasing d/L. Thus, the swimming economy is the best with the smallest active section, but in this case the swimming velocity is slower. To swim fast at a wide range of frequencies, the swimmer should have an active section equal to about a half of its full length, in which

case the swimming is more economical than the fully-active plate. Thus, an addition of the passive flap is advantageous for both swimming speed and economy.

We have previously shown (see Chapter2) for a plunging passive swimmer that a higher swimming economy is correlated with smaller center of mass displacement. Large vertical deflections in the bending pattern lead to strong side vortices and contribute to vortex induced drag, hindering the swimming efficiency [123]. Here, we plot the swimming economy of internally actuated swimmers as a function of the center of mass deflection in Figure 46 and find a general trend in which a smaller center of mass displacement leads to higher swimming economy.

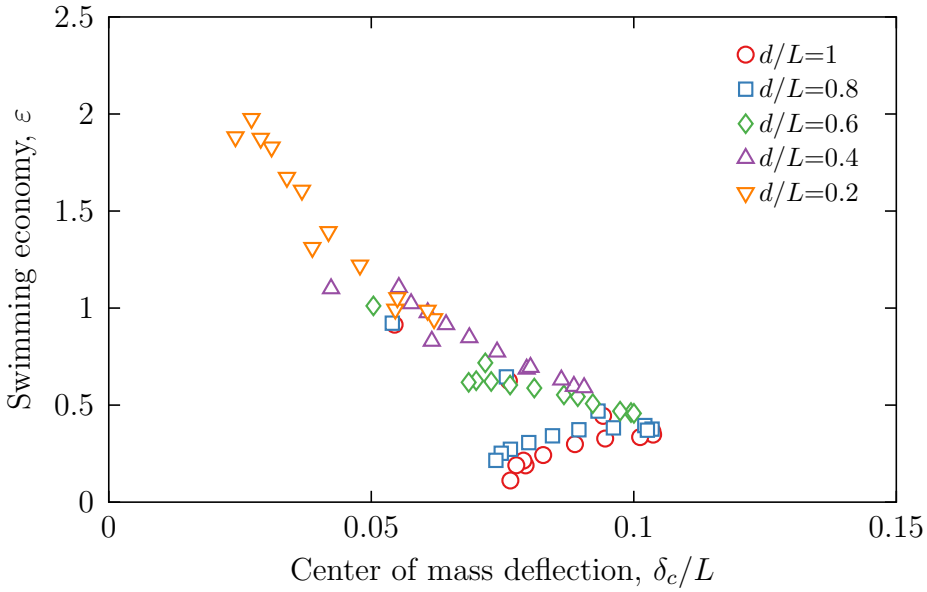

Figure 46: Swimming economy as a function of center of mass deflection of internally-actuated swimmers. Swimming economy generally decreases with increasing center of mass deflection with the exception of the poorer cases corresponding $d/L = 1$ and $d/L = 0.8$ at high frequencies.

Interestingly, we find for the cases showing poor economy at higher frequencies corresponding to $d/L = 1$ and $d/L = 0.8$ that the economy slightly increases with increasing center of mass deflection. This is likely due to the fact that the detrimental trailing edge angle dominates the swimming performance, whereas the increased viscous losses due to a greater center of mass displacement have a secondary effect.

In this case, a reduction of the trailing edge angle can lead to slightly better economy even for an increased center of mass displacement.

6.3 Summary

MFC bimorphs and other active materials are attractive oscillating propulsor alternatives to traditional cumbersome motor-based actuators [20–24] and have been used recently in untethered aquatic devices [130]. Our study demonstrates that the addition of passive flaps enhances the swimming speed and efficiency of moment actuated flexible fin propulsors. This conclusion agrees well with recent experimental observations that the addition of a passive flap to active fins leads to increased swimmer thrust and propulsion speed [132].

Specifically, we used three dimensional fully-coupled computer simulations to investigate free underwater locomotion of an internally-actuated elastic plate with a passive elastic attachment. The internal sinusoidal moment applied to the swimmer modeled piezoelectric actuation of an MFC bimorph. We isolated the hydrodynamics of the plate representing a swimmer fin and tested the swimming performance with different active to passive section size ratios. This allowed us to determine the effect of a passive attachment while holding the total length of the plate constant.

Our results indicated that the addition of a passive elastic flap improved both swimming speed and swimming efficiency. By probing the trailing edge kinematics and deflection curves, we determined that if the active and passive sections are of similar size, the overall performance is optimal. A large passive attachment was found to hinder overall swimmer deflection leading to slow swimming velocity. When the active section was too large, the internal moment actuation led to swimmer profiles that are not conducive to generating thrust at higher (post-resonance) frequency ratios. Specifically, the internal moment changed the angle of the trailing edge so that it is out of phase with the deflection.

We characterized efficiency using the swimming economy, and found that the economy increases with the size of the passive attachment. The plate with the largest passive section was the most economical, but also the slowest. For active section sizes in the range $d/L = 0.4$ and $d/L = 0.6$ (i.e. the active and passive sections are similar sized), the swimming velocity was overall the fastest and efficiency was better compared to fully active swimmers. In other words, we showed that by simply adding a passive attachment of similar material properties to the smart plate actuator better swimming performance can be achieved. We correlated this effect with the changes in the swimmer bending pattern.

CHAPTER VII

TURNING STRATEGIES FOR OSCILLATING FLEXIBLE PLATE SWIMMERS

7.1 Introduction and Computational Setup

Live fish use a combination of their multiple fins to achieve a steady turning mode or to accelerate quickly in a different direction to perform an escape maneuver [9, 133]. Motivated by the agile performance of real fish, a variety of turning designs have been implemented in robotic fish prototypes [134–137]. Some actuate the tail fin with a bias angle [138] or with an asymmetric stroke [130]. In a simple biomimetic swimmer which uses only a flexible plate for propulsion, it is desired to understand available turning mechanisms without having to use additional fins. In this chapter we use numerical simulations to investigate turning strategies for our flexible plate propulsor and quantify the turning performance as a function of actuation parameters.

We consider two strategies: 1) asymmetric passive plunging, which leads to a change of direction in the xz–plane, and 2) passive plunging with rotation, which leads to a change of direction in the xy–plane (see coordinate system in Figure 47). For strategy 1, we introduce the asymmetry in the plunging pattern by performing the upstroke and downstroke with different velocities. We find that the net lift force near the trailing edge (which creates a turning moment) increases with the ratio between upstroke and downstroke velocities, as expected. For strategy 2, we find that the lateral force and turning moment depends on the phase between plunging and rotation, and explain how lateral force and moment is maximized at a specific range of phase values.

When a rigid plate plunges in the vertical direction sinusoidally, the drag force

on the upstroke cancels with the drag force on the downstroke. In order to create a net force normal to the plate, the actuation pattern must be asymmetric between the upstroke and the downstroke.[1] Because the drag force is a function of velocity normal to plate, a simple mechanism to create a net drag is to actuate the upstroke and downstroke at different velocities.

Following this principle for a flexible plate, we actuate the leading edge with the following asymmetric plunging pattern:

$$A(t) = \begin{cases} A_0 \cos[\pi/\tau_1(t - n\tau)] & n\tau \leq t \leq n\tau + \tau_1 \\ -A_0 \cos[\pi/\tau_2(t - \tau_1 - n\tau)] & n\tau + \tau_1 \leq t \leq (n+1)\tau \end{cases} \tag{47}$$

This parametric equation represents motion in two parts. The downstroke motion is a half-cosine wave with amplitude A_0 and half-period τ_1. The upstroke motion is also a half-cosine wave with the same amplitude, but a different half-period τ_2. The total stroke period is $\tau = \tau_1 + \tau_2$, and $n = \lfloor t/\tau \rfloor$ is the current period number. The maximum speed on the downstroke is $v_1 = A_0\pi/\tau_1$ and upstroke is $v_2 = A_0\pi/\tau_2$. We consider values of velocity ratios, v_1/v_2 ranging from 2 to 10, so that the downstroke is always faster than the upstroke. This particular actuation pattern is suitable because the motion has continuity in both displacement and velocity, avoiding singularities in acceleration. Figure 47c illustrates the asymmetric plunging stroke during one period for different values of velocity ratio.

We expect that the asymmetric plunging pattern on the leading edge would result in an asymmetric plunging response on the remainder of the flexible plate, thereby creating a net force in the direction of plunging. The plate is actuated such that the total stroke period τ corresponds to the first natural frequency, and the deformation response would be amplified near the trailing edge. In this way the net hydrodynamic force is acting at a location off-center and closer to the trailing edge, which creates

[1] Note that this would not work if the drag force were exactly proportional to velocity, as in Stokes flow. In our regime, inertia is important, so an asymmetric plunging pattern will indeed create a net drag.

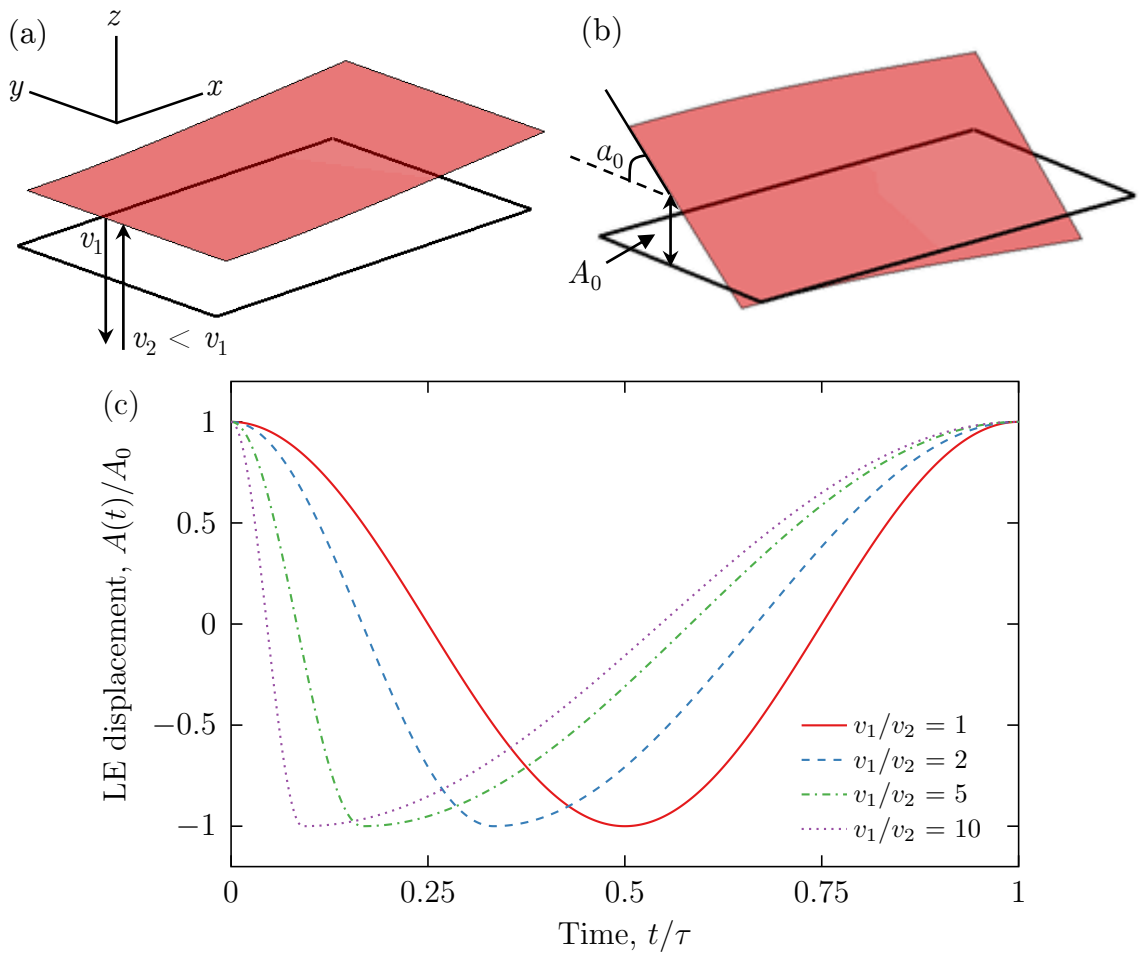

Figure 47: Schematics of (a) asymmetric plunging actuation and (b) combined plunging and rotation as turning strategies for biomimetic flexible plate swimmer. (c) Plots of the leading edge displacement for different values of velocity ratio v_1/v_2 as asymmetric plunging strategy.

the necessary pitching moment in order to change direction within the xz–plane.

Our second strategy to create a turning motion is to combine sinusoidal plunging with a sinusoidal rotation. This actuation pattern is similar to simplified models of insect hovering flight, although in this case the application is for generating a net lateral force perpendicular to the swimming direction in the xy–plane. We apply this combined plunging-rotation actuation pattern on the leading edge of the passive flexible swimmer. As shown in Figure 47b, the center of the leading edge is prescribed with sinusoidal plunging $A(t) = A_0 \cos(\omega t)$, where A_0 is the plunging amplitude. The

leading edge also undergoes a sinusoidal rotation with a tunable phase, given by $\alpha(t) = \alpha_0 \cos(\omega t + \psi)$, where α_0 is the rotation amplitude and ψ represents the phase difference between rotation and plunging.

We expect that the resulting kinematics and deformation response of the plate would lead to a motion that is asymmetric in y–direction, thus creating a net lateral force and yawing moment. The lateral force and turning moment is expected to be a function of the phase ψ and rotational amplitude α_0. We set the actuation frequency to the swimmer's first natural frequency and measure the forces and moments as functions of ψ and α_0. We use the same uniformly thick swimmer LSM model from Chapter 2, but constrain the leading edge to no horizontal movement.

7.2 Results and Discussion

7.2.1 Asymmetric Plunging

We first assess the turning performance of asymmetric plunging swimmers with a fixed plunging amplitude of $A_0 = 0.1L$ and velocity ratios ranging from 1 to 10. In Figure 48, we plot the net thrust (x–direction) and lift force (z–direction) as a function of velocity ratio, normalized by $F_0 = 0.5\rho U_0^2 wL$, where $U_0 = \omega A_0$. We expect the net lift to act near the trailing edge, where the acceleration of the plate is greatest. Because the net lift creates a turning moment, and we use the net lift to quantify the turning performance. We find that the lift force increases monotonically with increasing velocity ratio, which is unsurprising. The higher the velocity ratio, the larger the asymmetry exists between the upstroke and downstroke, leading to the larger net lift force. It is interesting that the thrust fluctuates to a shallow local minimum at $v_1/v_2 = 4$, but slowly increases with increasing velocity ratio. Despite the addition of asymmetry, the dominant force direction is still the thrust. At the largest velocity ratio, the thrust is about 3 times larger than the lift force.

To further understand the response of the asymmetric plunging, we use $v_1/v_2 = 5$

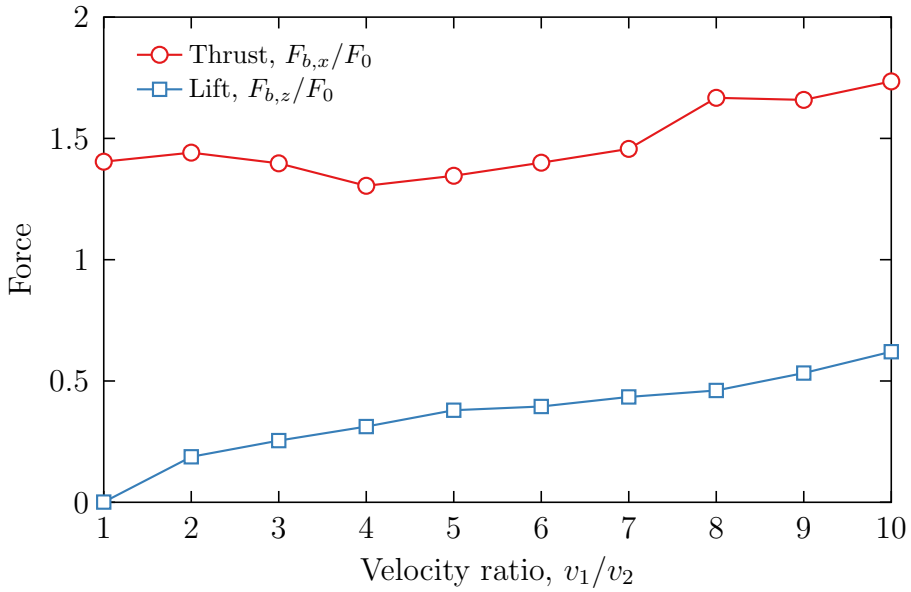

Figure 48: Thrust and lift on asymmetric plunging swimmer. Lift and therefore turning moment increases monotonically with velocity ratio.

as a representative case and plot in Figure 49a the time history of the leading and trailing edge displacements for one period. Interestingly, we find that the trailing edge displacement does not behave like a single sinusoid, but rather moves with a combination of the stroke frequency (the swimmer is actuated at the natural frequency) and higher frequency oscillations. A closer examination shows that one of the more pronounced higher frequencies is simply the frequency of the downstroke. The response with multiple frequencies is expected because an asymmetrical input actuation does not contain a single frequency. The higher frequency oscillations of displacement also imply that the trailing edge velocity and fluid force also oscillate with higher frequencies.

Snapshots of the bending pattern are plotted in Figure 49b at the representative times as indicated on Figure 49a with dashed lines. Point A ($t/\tau = 0$), shows the bending pattern of the plate at the start of the downstroke just before the swimmer accelerates downward. At this time, the trailing edge is located at approximately 80% of its peak amplitude. At point B (t/τ=0.16), the plate has finished the downstroke.

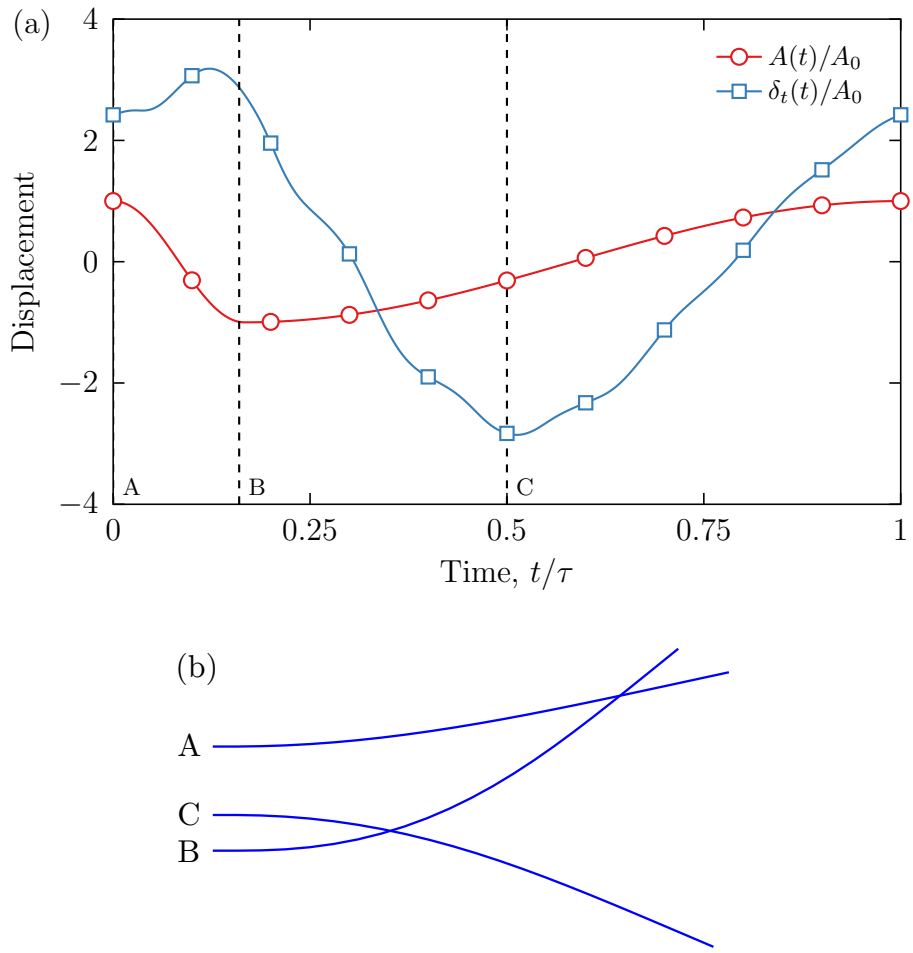

Figure 49: (a) Displacement time history and (b) bending profile at times A, B, and C, corresponding to times $t/\tau = 0$, 0.16, and 0.5, respectively. The asymmetry in the bending pattern is mainly caused by the quick movement from A to B.

Because of the high velocity, the trailing edge does not have time to respond and still stays near its peak amplitude. Near point B, the relative deflection is maximized. After point B, the trailing edge moves down at approximately the speed governed by its natural frequency, while the leading edge moves slowly upwards. At point C ($t/\tau = 0.5$), the trailing edge is located at its minimum position, after which it begins its upstroke until it reaches the original position at the start of the period. From these bending patterns we observe that the trailing edge response is nearly symmetric about the equilibrium position, but the motion of the leading edge governs the asymmetry

in the kinematics, particularly through the motion between A and B.

7.2.2 Combined Plunging and Rotation

In this section we assess the turning performance of the combined plunging and rotation of the leading edge. We actuate the plate at the first natural frequency and compute the net forces and moments during a stroke period. In Figures 50a and 50b, we plot the propulsive and lateral forces as a function of phase, ψ. The different lines represent the different values of rotational amplitude, α_0. Note that the values of $\psi > \pi$ lead to redundant results because $F_{b,x}(\psi) = F_{b,x}(\psi - \pi)$ and $F_{b,y}(\psi) = -F_{b,y}(\psi - \pi)$ from the symmetry of the problem.

We find that the propulsion decreases with increasing α_0, but it does not depend strongly on the phase ψ. This is due to the fact that the projected area decreases with increasing α_0. When the swimmer moves vertically, it also rotates, decreasing the projected area in the plunging direction. As a result, less fluid is deflected backwards so the resulting thrust is smaller. The thrust curves also imply that the net propulsion can be tuned by increasing or decreasing the rotational amplitude.

In contrast, the lateral force is a strong function of both α_0 and ψ. When comparing at the maximum lateral force for each value of α_0, we observe that the optimal rotational amplitude is $\alpha_0 = \pi/4$. For this rotational amplitude, we find that the optimal phase to generate the largest lateral force is $\psi = \pi/6$, but this optimum is shallow. When considering the "high-performing" amplitude values of $\pi/6$, $\pi/4$, and $\pi/3$, high lateral force is found in the range between $\psi = -\pi/12$ and $\psi = 5\pi/12$. Similarly, there is also a region between $\psi = 7\pi/12$ and $\psi = 3\pi/4$ that leads to poor lateral force.

A net lateral force itself does not necessarily result in a change in direction. To demonstrate the capability to change direction, we compute the net moment due to the fluid, $M_{b,z}$, about the z–axis through the plate's centroid at equilibrium position.

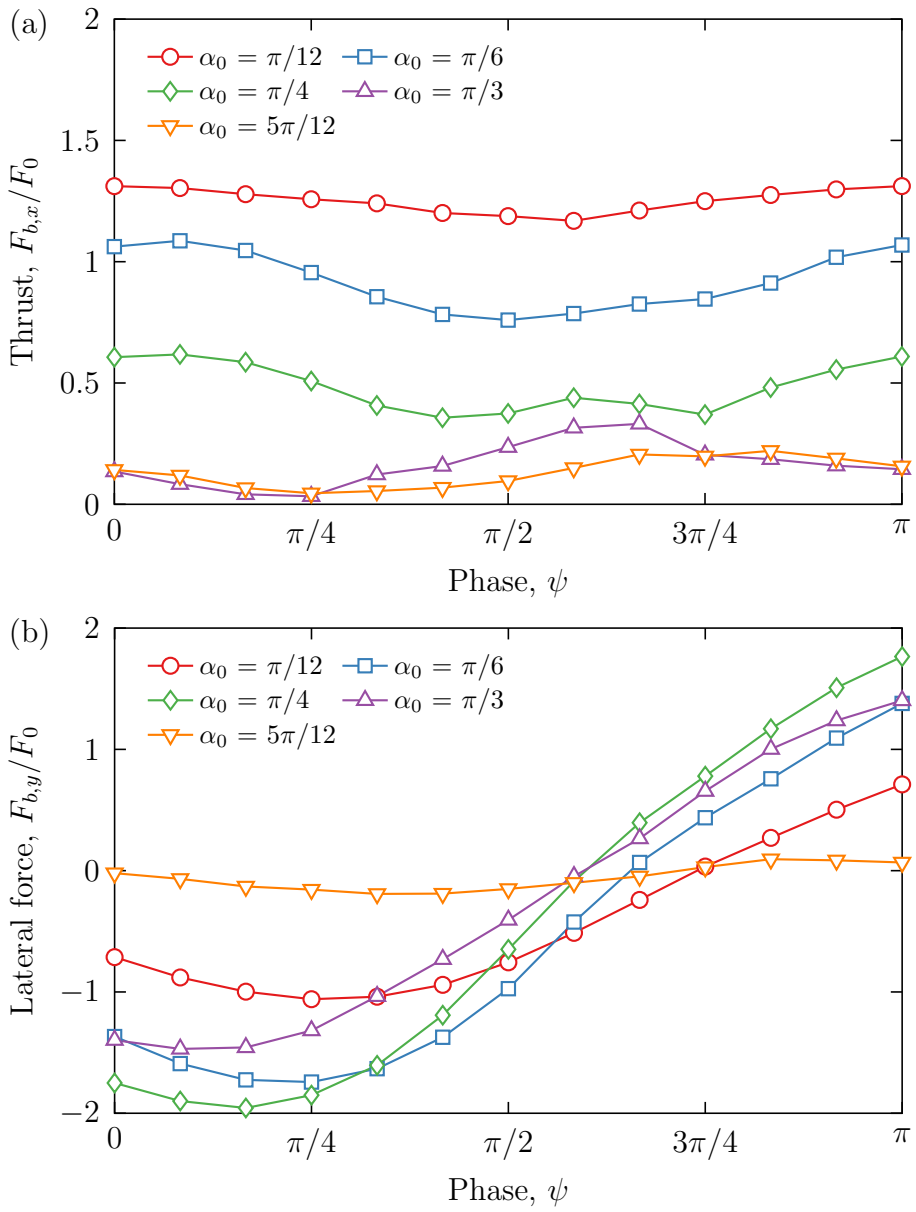

Figure 50: (a) Propulsive and (b) lateral forces for combined plunging and rotating swimmer. Propulsive forces decrease with increasing α_0, which is related to the smaller projected areas for increasing α_0. Lateral force is maximized in a range of phase values $\psi = -\pi/12$ and $\psi = 5\pi/12$.

The net moment leads to a change in the yaw angle about the z–axis and is normalized by $M_0 = 2I^m_{zz}/\tau^2$. Here, I^m_{zz} is the z–axis mass moment of inertia, and the non-dimensional moment $M_{b,z}/M_0$ approximates the yaw angle change per stroke period (with no fluid resistance). In Figure 50 we plot the moment as a function of ψ and

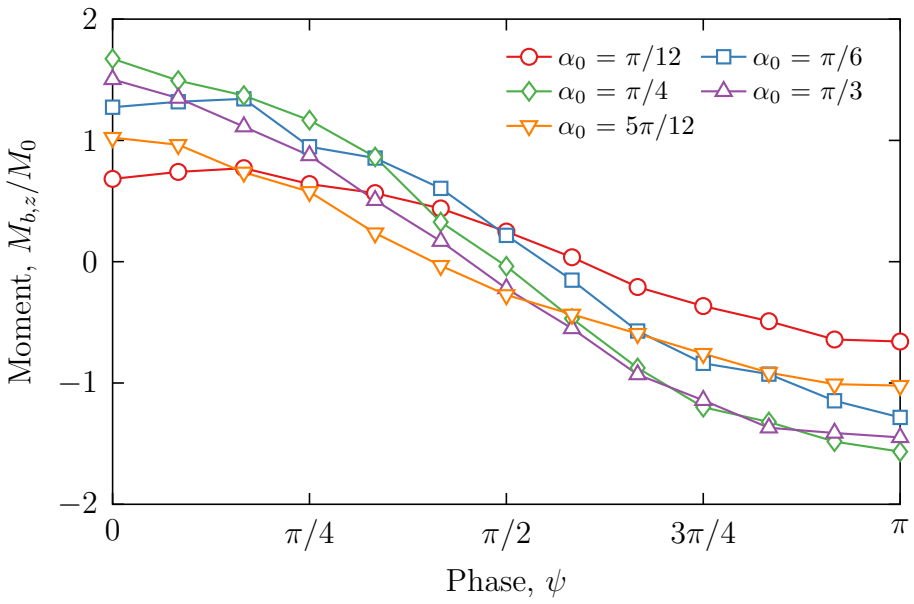

Figure 51: Turning moment for combined plunging and rotating swimmer. The moment follows similar trends to lateral force.

α_0. The trends for moment correlate with the trends for the lateral force, suggesting that the net lateral force is indeed responsible for the yawing moment. Interestingly, we find that for $\alpha_0 = 5\pi/12$, the lateral force is small, but the moment is non-zero. This suggests that a net lateral couple is applied on this particular swimmer, so it can turn without drifting.

In order to understand the mechanism that leads to high lateral force production, we first seek to understand the kinematics of the swimmer response. In Figure 52a we consider a rotating coordinate system (shown in red), denoted by the $(xyz)'$ axes, that is attached to the leading edge so that the z'–axis is always normal to the leading edge. Figure 52b gives the perspective of the swimmer relative to the $(xyz)'$ axes. Denote the position vectors of the maximum extent of the trailing edge corners by $\mathbf{r}_{y+}$ and $\mathbf{r}_{y-}$. The absolute displacement for the trailing edge corner points are denoted by $\delta_{y,\pm}$ as labeled in Figure 52a. The displacements of these corner points relative to the surface normal is given by $\delta_{\text{rel},y\pm} = \mathbf{r}_{y\pm} \cdot \hat{\mathbf{z}}'$ as labeled in Figure 52b.

In Figure 52c, we plot $\delta_{y\pm}$ and $\delta_{\text{rel},y\pm}$ as functions of ψ for the case $\alpha_0 = \pi/4$.

We observe that at low phase angles $\psi < \pi/4$, where lateral force is maximized, the absolute displacements are also maximized, suggesting that the larger displacements yield larger lateral forces. What is interesting though is that the relative displacements of the two trailing edge corner points nearly coincide, showing that the plate undergoes a negligible amount of twisting during the swimming stroke. Therefore, the plate plunges vertically relative to the surface normal, but the surface normal is also continuously changing direction based on $\alpha(t)$.

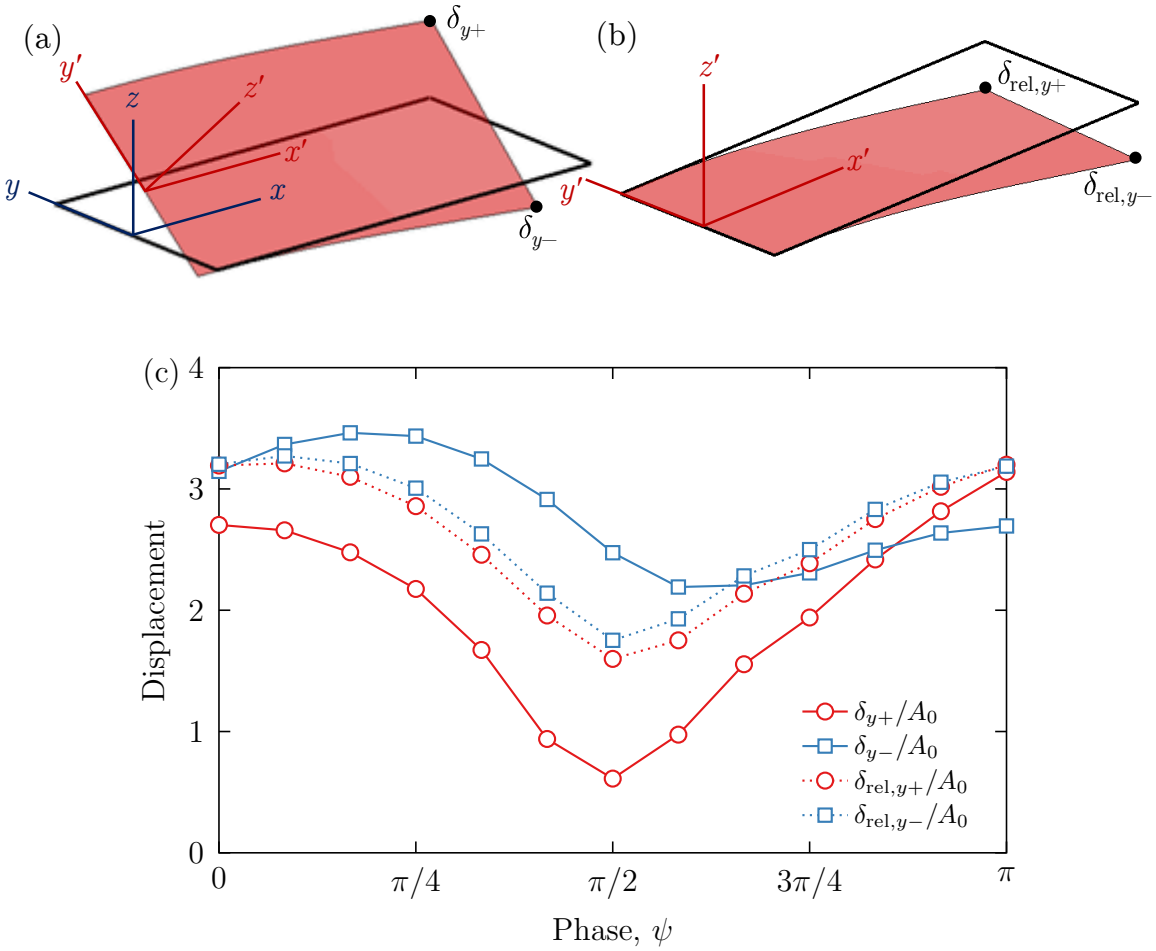

Figure 52: (a) Schematic showing rotating $(xyz)'$ axes relative to the fixed (xyz) axes. (b) Perspective of swimmer in $(xyz)'$ axes. (c) Absolute and relative deflections of the trailing edge corner points. The relative deflection of the corner points nearly coincide, showing that the swimmer has negligible twist motion.

Another step to understanding the physics behind the lateral force production is

to understand the symmetric vertical force production of a plunging plate undergoing no rotation. Figure 53 shows the time histories of the relative trailing edge velocity $v_{TE,r}(t) = \frac{d}{dt}[\delta_t(t) - A(t)]$ and the vertical force. We observe that the maximum (most negative) trailing edge relative velocity has a phase delay of approximately 0.29π rad to the maximum vertical force, as indicated by the dotted lines. We would expect that the vertical force and velocity would be correlated because the faster a plate moves normal to its surface, the larger drag force it experiences.

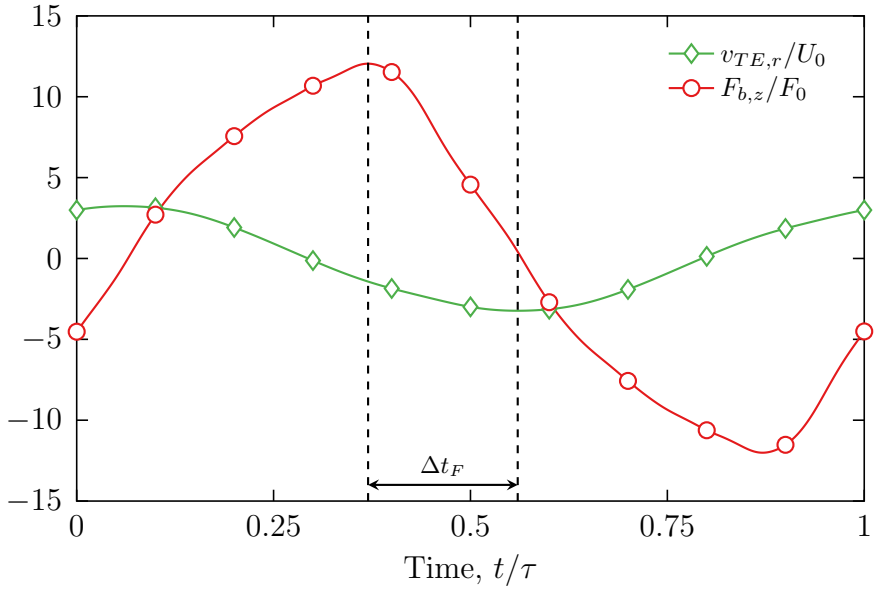

Figure 53: Time histories of relative trailing edge velocity for a plunging plate with no rotation showing the time of maximum vertical force production relative to the maximum trailing edge velocity.

Finally, we examine the time histories of the rotation angle, α, lateral force $F_{b,y}$, moment $M_{b,z}$, and relative trailing edge velocity in the $(xyz)'$ reference frame, $v_{TE,r} = \frac{d}{dt}\left[0.5(\delta_{\text{rel},y+}(t) + \delta_{\text{rel},y-}(t))\right]$. The time histories for $\alpha_0 = \pi/4$ and $\psi = \pi/6$, the case which exhibits the largest net lateral force (Figure 50b), are plotted in Figure 54 and provide insight into the lateral force production.

We observe first that the maximum moment, lateral force, and rotation angle all coincide. This shows that for this case, the largest lateral force production occurs at the maximum rotation angle. As Figure 52 had suggested, the plate is simply plunging

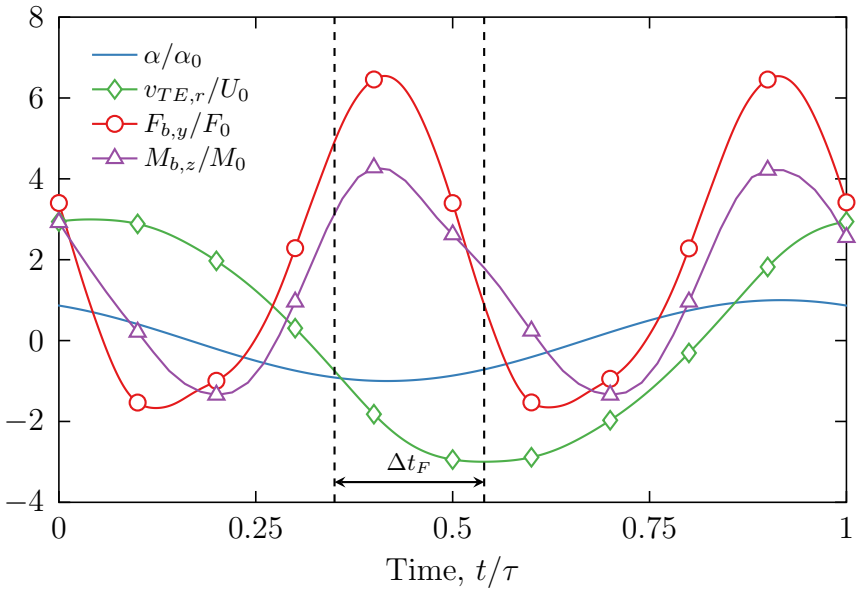

Figure 54: Time histories for multiple quantities for $\alpha_0 = \pi/4$ and $\psi = \pi/6$. Large lateral force and turning moment are produced because the time of maximum force production based on the relative TE velocity is tuned to the maximum of α.

up and down, while changing its surface normal. Force production should therefore be primarily normal to the surface. The time history of $v_{TE,r}$ is also shown, and the dotted line represents the time of maximum force production based on the phase difference computed for a plunging swimmer in Figure 53. The time of maximum force production coincides closely with $\alpha(t)$ and the other quantities. The large lateral force production is now understood. The phase difference ψ must be tuned so that the maximum rotation occurs at the same time of maximum force production based on the correlation with $v_{TE,r}$. This way, the largest amount of force produced, which is in the direction normal to the plate surface, can be directed laterally during the stroke.

We can also observe that the first peaks of lateral force and moment correspond to a trailing edge downstroke relative to the surface normal based on the negative value of $v_{TE,r}$. At this point, α is negative, which means that in the inertial frame, the downstroke has a $-\hat{\mathbf{y}}$–component, generating a lateral force in $+\hat{\mathbf{y}}$–direction and moment in the $+\hat{\mathbf{z}}$–direction. The second peak corresponds to an upstroke, but now

α is positive, so the upstroke has a $-\hat{\mathbf{y}}$–component, generating a force again in the $+\hat{\mathbf{y}}$–direction and a moment again in the $+\hat{\mathbf{z}}$–direction. At the valleys of $F_{b,y}$, the force production is small based on the velocity–relative deflection phase difference and α is small, so force is directed mostly parallel to the $\hat{\mathbf{z}}$–direction. Evidently, tuning ψ to match the force production has also the benefit of reducing unwanted lateral force in the opposite direction.

This principle also explains the poor lateral force and moment production at other values of ψ. In Figure 55, we plot the time histories of the same quantities for $\alpha_0 = \pi/4$ and $\psi = 7\pi/12$. We find that the maximum force production is aligned with α when $\alpha \approx 0$, so the maximum force is directed in the $\hat{\mathbf{z}}$–direction. Furthermore, when α is largest, the time of maximum force production is near zero, and thus the lateral force produced is correspondingly near zero. At the peaks of lateral force and moment, the α value and force production are suboptimal, and the peaks and valleys also cancel each other. Thus, the force production and α are not synchronized, which causes little to no turning moment or lateral force produced.

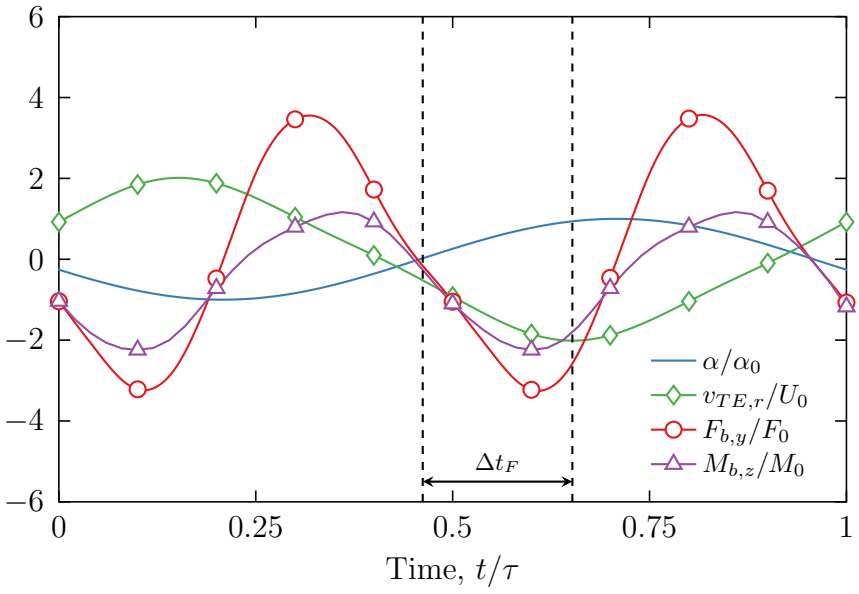

Figure 55: Time histories for multiple quantities for $\alpha_0 = \pi/4$ and $\psi = 7\pi/12$. Little lateral force and moment production is due to the time of maximum force production occuring when $\alpha \approx 0$, so force is directed vertically, not laterally.

7.3 Summary

In this chapter, we studied two strategies for changing direction for an oscillating flexible plate swimmer by changing actuation patterns. The first strategy was to impose a plunging motion with a faster velocity on the downstroke compared to the upstroke. This created a pitching moment. We found that the asymmetric plunging stroke created a net lift force on the trailing edge during each stroke period, which contributed to a turning moment. The magnitude of the lift force increased monotonically with increasing velocity ratio, and the asymmetry in the bending pattern was mainly caused by the fast downstroke in which the trailing edge did not have time to respond.

The second strategy was to combine sinusoidal plunging with sinusoidal rotation, which resulted in a yawing moment. We investigated the lateral force production as a function of the rotation amplitude and phase difference between plunging and rotation. We found a range of optimal phase angles in which lateral force and moment production is best. Furthermore, we observed the resulting kinematics and found that the bending is primarily normal to the surface with no twisting motion. We examined the time history between relative trailing edge velocity and force production, and showed that in order to optimize turning moment and lateral force, the phase must be tuned so that the time of maximum rotation corresponds with the time of maximum force production.

CHAPTER VIII

CONCLUDING REMARKS AND OUTLOOK

In this dissertation we have studied the hydrodynamics and bending patterns of a simplified biomimetic propulsor that represents an abstraction of fish locomotion. The biomimetic propulsor is modeled as an oscillating flexible plate submerged in a viscous fluid. These studies were conducted using fully coupled three-dimensional numerical simulations in order to capture both the elastic deformation and fluid flow. We have investigated the swimming performance when the plate is driven near the first natural frequency, and probed how performance changes with bending pattern, mass, shape, non-uniform thickness, and actuation patterns. We have also quantified two possible strategies to change direction in three dimensions.

We first established an understanding of the physics behind the free swimming of a plunging flexible plate with $AR = 2.5$ actuated near the first natural frequency. We identified two vastly different free swimming modes leading to either fast or efficient swimming by simply altering the actuation frequency. Fast swimming is achieved by actuating near the first natural frequency to take advantage of resonance oscillations. We found that heavier fins swim faster and there is a nearly linear relationship between free swimming velocity and trailing edge displacement, indicating that swimming at higher speeds requires a larger displacement of the trailing edge. Fast swimming comes with the cost of a higher power required to drive the swimmer, and economical swimming is found at post-resonance frequencies. In this regime, the elastic swimmer exhibits a bending pattern in which its center of mass has a minimum displacement normal to the swimming direction. This swimming pattern minimizes the magnitude of external force required to sustain the motion, which in turn reduces the input

power and enhances swimming economy.

The fast and efficient regimes were also found for rectangular and trapezoidal swimmers with different aspect ratios. Surprisingly, we found that the lowest aspect ratio swimmers moved the fastest due to a lower net drag per unit width. This drag is induced by the side edge vortices (SEV), whose size depends on the trailing edge displacement. For lower aspect ratio (wider) swimmers, the SEV size to width ratio is smaller than for higher aspect ratio swimmers. Thus, wider swimmers can swim faster. Trapezoidal swimmers with the same area but different width ratios showed little performance change between them. The differences in the bending responses and geometries for the different trapezoidal swimmers led to competing changes in thrust generation that ultimately balanced out, causing velocity and swimming economy to be similar.

Swimmers with tapered thickness showed wideband high economical performance at post-resonance frequencies. This was due to the lower power and sustained swimming velocity at higher frequency ratios. The lower power occurred for the same reasons as a uniformly thick swimmer — power is correlated with external force amplitude, and at those higher frequencies the external force amplitude is minimized. The sustained higher velocity was due to the larger curvature near the trailing edge as a result of the cubically varying bending rigidity. Similar results held for tapered trapezoidal swimmers as it was found that the tapered thickness dominated the bending rigidity distribution.

The swimming performance of an internally actuated biomimetic plate oscillating with a passive fin attachment was also studied. Results indicated that the addition of a passive elastic flap improved both swimming speed and swimming efficiency. Overall performance is optimal if the active and passive sections were of similar size. A large passive attachment was found to hinder overall swimmer deflection leading to slow swimming velocity. When the active section was too large, the internal moment

actuation led to swimmer profiles that are not conducive to generating thrust at higher (post-resonance) frequency ratios. Specifically, the internal moment changed the angle of the trailing edge so that it is out of phase with the deflection. Compared to fully active swimmers, the swimming economy improved with the size of the passive fin. Thus, by simply adding a passive attachment of similar material properties to the smart plate actuator better swimming performance can be achieved.

Finally, we investigated two strategies for changing direction for an oscillating flexible plate swimmer by changing actuation patterns. The first strategy was to create a pitching moment by imposing a plunging motion with a faster velocity on the downstroke compared to the upstroke. The lift force (and turning moment, by implication), increased monotonically with increasing velocity ratio. The second strategy was to create a yawing moment by combining sinusoidal plunging with sinusoidal rotation. A range of optimal phase angles with high lateral force and turning moment production was found. This optimal range was linked to the time of the maximum force production during a plunging stroke matching the time when the swimmer undergoes maximum rotation.

The results of this research are useful for designing a small scale fish-like propulsor using a thin flexible strip and driven near the first natural frequency. In particular, we showed that the flexible strip should have a low aspect ratio and be tapered on its length to improve speed and efficiency. The tapering also mitigates the performance sensitivity to bending pattern. If a smart material is used for actuation, then an addition of a passive fin improves performance even if the length is unchanged. Turning while swimming could be accomplished using the strategies discussed in Chapter 7, although there are many other possibilities to achieve turning. In order to fully design a robust biomimetic swimmer that can swim in three dimensions, a more complete investigation into steady turning must be performed, such as measuring the radius of curvature under different actuation parameters. Furthermore, other swimming modes

must be considered, particularly straight-line acceleration, deceleration, and rapid directional change (such as by mimicking the C-shape sharp turn exhibited by live fish [134, 137]). The transient, unsteady flow physics that govern these quick maneuvers remain to be fully understood for mature use in robotic fish technology. Furthermore, in an actual robotic fish, the oscillating plate is attached to a body housing, and the effects of the body housing on the flow need also be considered. Understanding performance in other swimming environments such as swimming near walls and swarming is also important for robotic fish design. While our results are primarily applicable for the design of simple biomimetic propulsors, they perhaps shed light on why many fish have tapered, low aspect ratio caudal fins. A complete understanding of fish swimming mechanics remains to be seen.

APPENDIX A

MODE SHAPES OF TAPERED EULER-BERNOULLI CANTILEVER BEAM

Given an Euler-Bernoulli cantilever beam with thickness b_l at the fixed end linearly tapering to thickness b_t at the free end, the mode shapes, $\phi(x)$, follow the governing equation

$$\frac{d^2}{dx^2}\left[EI(x)\frac{d^2\phi}{dx^2}\right] = \rho_s w b(x)\omega^2\phi. \tag{48}$$

where $EI(x)$ and $b(x)$ are given in equations (30) and (28), respectively, and ω is the frequency of free vibration. For a uniform beam, the solution is well-known [139] and the nth mode shape is given by

$$\phi_n(x) = A\cos(\lambda_n x/L) + B\cosh(\lambda_n x/L) + C\sin(\lambda_n x/L) + D\sinh(\lambda_n x/L). \tag{49}$$

For a tapered beam, the derivation follows the work of Mabie and Rogers [140], and the nth mode shape is given by

$$\phi_n(\xi) = \frac{1}{\sqrt{\xi}}\left[AJ_1(2k_n\sqrt{\xi}) + BY_1(2k_n\sqrt{\xi}) + CI_1(2k_n\sqrt{\xi}) + DK_1(2k_n\sqrt{\xi})\right]. \tag{50}$$

where J_1, Y_1, I_1, K_1 are first-order Bessel functions and modified Bessel functions of the first and second kinds, and $\xi = b_l + (b_t - b_l)x/L$.

The coefficients A, B, C, D and eigenvalues λ_n and k_n are determined by satisfying the boundary conditions

$$\phi_n(x=0) = 0, \quad \phi_n'(x=0) = 0, \quad \phi_n''(x=L) = 0, \quad \phi_n'''(x=L) = 0. \tag{51}$$

Substitution of the mode shapes into the boundary conditions yields an eigenvalue problem for λ_n or k_n and A, B, C, D as non-trivial solutions to the resulting linear

system of equations. Both the eigenvalue problem and linear system are numerically solved. As the coefficients are valid to a multiplicative constant when solving this eigenvalue problem (3 of the 4 coefficients are found), the mode shapes may be mass-normalized to follow the condition

$$\int_0^L \phi_m(x)\rho_s wb(x)\phi_n(x)dx = \delta_{mn}. \tag{52}$$

Using this condition when $n = m$, the final coefficient is found, so the mass-normalized mode shapes are uniquely determined. Finally, the natural frequencies are related to the eigenvalues as such:

$$\omega_n = \lambda_n^2 \frac{b}{L^2}\sqrt{\frac{E}{12\rho_s}}, \quad \text{Uniform} \tag{53}$$

$$\omega_n = k_n^2 \frac{(b_t - b_l)^2}{L^2}\sqrt{\frac{E}{12\rho_s}}, \quad \text{Tapered} \tag{54}$$

REFERENCES

[1] Flammang, B. E. and Lauder, G. V., "Caudal fin shape modulation and control during acceleration, braking and backing maneuvers in bluegill sunfish, Lepomis macrochirus," *Journal of Experimental Biology*, vol. 212, no. 2, pp. 277–286, 2009.

[2] Flammang, B. E. and Lauder, G. V., "Speed-dependent intrinsic caudal fin muscle recruitment during steady swimming in bluegill sunfish, Lepomis macrochirus," *Journal of Experimental Biology*, vol. 211, no. 4, pp. 587–598, 2008.

[3] Esposito, C. J., Tangorra, J. L., Flammang, B. E., and Lauder, G. V., "A robotic fish caudal fin: Effects of stiffness and motor program on locomotor performance," *Journal of Experimental Biology*, vol. 215, no. 1, pp. 56–67, 2012.

[4] Griffiths, G., *Technology and applications of autonomous underwater vehicles*. CRC Press, 2002.

[5] Leonard, N. E. and Graver, J. G., "Model-based feedback control of autonomous underwater gliders," *IEEE Journal of Oceanic Engineering*, vol. 26, no. 4, pp. 633–645, 2001.

[6] Deng, X. and Avadhanula, S., "Biomimetic micro underwater vehicle with oscillating fin propulsion: System design and force measurement," in *Proceedings of the 2005 IEEE International Conference on Robotics and Automation*, pp. 3312–3317, IEEE, 2005.

[7] Tan, X., Kim, D., Usher, N., Laboy, D., Jackson, J., Kapetanovic, A., Rapai, J., Sabadus, B., and Zhou, X., "An autonomous robotic fish for mobile sensing," in *Proceedings of the 2006 IEEE/RSJ International Conference on Intelligent Robots and Systems*, pp. 5424–5429, IEEE, 2006.

[8] Fukuda, T., Kawamoto, A., Arai, F., and Matsuura, H., "Steering mechanism of underwater micro mobile robot," in *Proceedings of the 1995 IEEE International Conference on Robotics and Automation*, vol. 3, pp. 363–368, IEEE, 1995.

[9] Sfakiotakis, M., Lane, D. M., and Davies, J. B. C., "Review of fish swimming modes for aquatic locomotion," *IEEE Journal of Oceanic Engineering*, vol. 24, no. 2, pp. 237–252, 1999.

[10] Du, R., Li, Z., Youcef-Toumi, K., and y Alvarado, P. V., *Robot fish*. Springer, 2015.

[11] Videler, J. J., *Fish swimming*. Springer Science & Business Media, 1993.

[12] Drucker, E. G. and Lauder, G. V., "A hydrodynamic analysis of fish swimming speed: Wake structure and locomotor force in slow and fast labriform swimmers," *Journal of Experimental Biology*, vol. 203, no. 16, pp. 2379–2393, 2000.

[13] Drucker, E. G. and Lauder, G. V., "Locomotor function of the dorsal fin in teleost fishes: Experimental analysis of wake forces in sunfish," *Journal of Experimental Biology*, vol. 204, no. 17, pp. 2943–2958, 2001.

[14] Standen, E. M. and Lauder, G. V., "Hydrodynamic function of dorsal and anal fins in brook trout (Salvelinus fontinalis)," *Journal of Experimental Biology*, vol. 210, no. 2, pp. 325–339, 2007.

[15] Barrett, D. S., *Propulsive efficiency of Robotuna*. PhD thesis, Massachusetts Institute of Technology, 1988.

[16] Drucker, E. G. and Lauder, G. V., "Locomotor forces on a swimming fish: Three-dimensional vortex wake dynamics quantified using digital particle image velocimetry," *Journal of Experimental Biology*, vol. 202, no. 18, pp. 2393–2412, 1999.

[17] Gibb, A., Jayne, B., and Lauder, G., "Kinematics of pectoral fin locomotion in the bluegill sunfish Lepomis macrochirus," *Journal of Experimental Biology*, vol. 189, no. 1, pp. 133–161, 1994.

[18] Lauder, G. V., Madden, P. G. A., Mittal, R., Dong, H., and Bozkurttas, M., "Locomotion with flexible propulsors: I. Experimental analysis of pectoral fin swimming in sunfish," *Bioinspiration & Biomimetics*, vol. 1, no. 4, pp. S25–S34, 2006.

[19] Standen, E. M. and Lauder, G. V., "Dorsal and anal fin function in bluegill sunfish Lepomis macrochirus: Three-dimensional kinematics during propulsion and maneuvering," *Journal of Experimental Biology*, vol. 208, no. 14, pp. 2753–2763, 2005.

[20] Anderson, J. M. and Chhabra, N. K., "Maneuvering and stability performance of a robotic tuna," *Integrative and Comparative Biology*, vol. 42, no. 1, pp. 118–126, 2002.

[21] Hirata, K., "Development of experimental fish robot," in *Proceedings of the Sixth International Symposium on Marine Engineering (ISME 2000)*, pp. 23–27, 2000.

[22] Ding, R., Yu, J., Yang, Q., Tan, M., and Zhang, J., "CPG-based dynamics modeling and simulation for a biomimetic amphibious robot," in *Proceedings of the 2009 IEEE International Conference on Robotics and Biomimetics*, pp. 1657–1662, IEEE, 2009.

[23] Liu, F., Lee, K.-M., and Yang, C.-J., "Hydrodynamics of an undulating fin for a wave-like locomotion system design," *IEEE/ASME Transactions on Mechatronics*, vol. 17, no. 3, pp. 554–562, 2012.

[24] Kopman, V., Laut, J., Acquaviva, F., Rizzo, A., and Porfiri, M., "Dynamic modeling of a robotic fish propelled by a compliant tail," *IEEE Journal of Oceanic Engineering*, vol. 40, no. 1, pp. 209–221, 2015.

[25] Lauder, G. V., Anderson, E. J., Tangorra, J., and Madden, P. G. A., "Fish biorobotics: Kinematics and hydrodynamics of self-propulsion," *Journal of Experimental Biology*, vol. 210, no. 16, pp. 2767–2780, 2007.

[26] Lauder, G. V., Flammang, B., and Alben, S., "Passive robotic models of propulsion by the bodies and caudal fins of fish," *Integrative and Comparative Biology*, pp. 1–12, 2012.

[27] Quinn, D. B., Moored, K. W., Dewey, P. A., and Smits, A. J., "Unsteady propulsion near a solid boundary," *Journal of Fluid Mechanics*, vol. 742, pp. 152–170, 2014.

[28] Shahinpoor, M., "Conceptual design, kinematics and dynamics of swimming robotic structures using ionic polymeric gel muscles," *Smart Materials and Structures*, vol. 1, no. 1, pp. 91–94, 1992.

[29] Mojarrad, M. and Shahinpoor, M., "Noiseless propulsion for swimming robotic structures using polyelectrolyte ion-exchange membrane," in *Proceedings of SPIE 2716, Smart Structures and Materials 1996: Smart Materials Technologies and Biomimetics*, pp. 183–192, SPIE, 1996.

[30] Chen, Z., Um, T. I., Zhu, J., and Bart-Smith, H., "Bio-inspired robotic cownose ray propelled by electroactive polymer pectoral fin," in *Proceedings of the ASME 2011 International Mechanical Engineering Congress and Exposition*, pp. 817–824, ASME, 2011.

[31] Chen, Z., Um, T. I., and Bart-Smith, H., "Ionic polymer-metal composite enabled robotic manta ray," in *Proceedings of SPIE 7976, Electroactive Polymer Actuators and Devices (EAPAD) 2011*, 797637, SPIE, 2011.

[32] Chen, Z., Shatara, S., and Tan, X., "Modeling of biomimetic robotic fish propelled by an ionic polymer–metal composite caudal fin," *IEEE/ASME Transactions on Mechatronics*, vol. 15, no. 3, pp. 448–459, 2010.

[33] Shen, Q., Wang, T., and Kim, K. J., "A biomimetic underwater vehicle actuated by waves with ionic polymer–metal composite soft sensors," *Bioinspiration & Biomimetics*, vol. 10, no. 5, 055007, 2015.

[34] Aureli, M., Kopman, V., and Porfiri, M., "Free-locomotion of underwater vehicles actuated by ionic polymer metal composites," *IEEE/ASME Transactions on Mechatronics*, vol. 15, no. 4, pp. 603–614, 2010.

[35] Wang, Z., Hang, G., Li, J., Wang, Y., and Xiao, K., "A micro-robot fish with embedded SMA wire actuated flexible biomimetic fin," *Sensors and Actuators A: Physical*, vol. 144, no. 2, pp. 354–360, 2008.

[36] Cho, K.-J., Hawkes, E., Quinn, C., and Wood, R. J., "Design, fabrication and analysis of a body-caudal fin propulsion system for a microrobotic fish," in *Proceedings of the 2008 IEEE International Conference on Robotics and Automation*, pp. 706–711, IEEE, 2008.

[37] Shinjo, N. and Swain, G. W., "Use of a shape memory alloy for the design of an oscillatory propulsion system," *IEEE Journal of Oceanic Engineering*, vol. 29, no. 3, pp. 750–755, 2004.

[38] Wang, Z., Hang, G., Wang, Y., Li, J., and Du, W., "Embedded SMA wire actuated biomimetic fin: A module for biomimetic underwater propulsion," *Smart Materials and Structures*, vol. 17, no. 2, 025039, 2008.

[39] Rossi, C., Colorado, J., Coral, W., and Barrientos, A., "Bending continuous structures with SMAs: A novel robotic fish design," *Bioinspiration & Biomimetics*, vol. 6, no. 4, 045005, 2011.

[40] Rossi, C., Coral, W., Colorado, J., and Barrientos, A., "A motor-less and gear-less bio-mimetic robotic fish design," in *Proceedings of the 2011 IEEE International Conference on Robotics and Automation*, pp. 3646–3651, IEEE, 2011.

[41] Zhang, Y. and Liu, G., "Wireless micro biomimetic swimming robot based on giant magnetostrictive films," in *Proceedings of the 2005 IEEE International Conference on Robotics and Biomimetics*, pp. 195–200, IEEE, 2005.

[42] Zhang, Y. and Liu, G., "Wireless swimming microrobot: design, analysis, and experiments," *Journal of Dynamic Systems, Measurement, and Control*, vol. 131, no. 1, 011004, 2009.

[43] Zhang, Y. and Liu, G., "Design, analysis and experiments of a wireless swimming micro robot," in *Proceedings of the 2005 IEEE International Conference on Mechatronics and Automation*, vol. 2, pp. 946–951, IEEE, 2005.

[44] Zhang, Z., Philen, M., and Neu, W., "A biologically inspired artificial fish using flexible matrix composite actuators: Analysis and experiment," *Smart Materials and Structures*, vol. 19, no. 9, 094017, 2010.

[45] Zhang, Z. G., Gondo, M., Yamashita, N., Yamamoto, A., and Higuchi, T., "Design and control of a fish-like robot using an electrostatic motor," in *Proceedings of the 2007 IEEE International Conference on Robotics and Automation*, pp. 974–979, IEEE, 2007.

[46] Philen, M. and Neu, W., "Hydrodynamic analysis, performance assessment, and actuator design of a flexible tail propulsor in an artificial alligator," *Smart Materials and Structures*, vol. 20, no. 9, 094015, 2011.

[47] Erturk, A. and Inman, D. J., *Piezoelectric energy harvesting*. John Wiley & Sons, 2011.

[48] Ming, A., Park, S., Nagata, Y., and Shimojo, M., "Development of underwater robots using piezoelectric fiber composite," in *Proceedings of the 2009 IEEE International Conference on Robotics and Automation*, pp. 3821–3826, IEEE, 2009.

[49] Heo, S., Wiguna, T., Park, H. C., and Goo, N. S., "Effect of an artificial caudal fin on the performance of a biomimetic fish robot propelled by piezoelectric actuators," *Journal of Bionic Engineering*, vol. 4, no. 3, pp. 151–158, 2007.

[50] Wiguna, T., Heo, S., Park, H. C., and Goo, N. S., "Design and experimental parameteric study of a fish robot actuated by piezoelectric actuators," *Journal of Intelligent Material Systems and Structures*, vol. 20, no. 6, pp. 751–758, 2009.

[51] Fukuda, T., Kawamoto, A., Arai, F., and Matsuura, H., "Steering mechanism and swimming experiment of micro mobile robot in water," in *Proceedings of IEEE Micro Electro Mechanical Systems, 1995*, pp. 300–305, IEEE, 1995.

[52] Wagner, H., "Concerning the dynamic ascending force formation of aerofoils," *Zeitschrift für Angewandte Mathematik und Mechanik*, vol. 5, pp. 17–35, 1925.

[53] Theodorsen, T., "General theory of aerodynamic instability and the mechanism of flutter," *NACA Technical Report*, no. 496, 1949.

[54] Garrick, I. E., "Propulsion of a flapping and oscillating airfoil," *NACA Technical Report*, no. 567, 1937.

[55] Wu, T. Y.-T., "Hydromechanics of swimming propulsion. Part 1. Swimming of a two-dimensional flexible plate at variable forward speeds in an inviscid fluid," *Journal of Fluid Mechanics*, vol. 46, no. 2, pp. 337–355, 1971.

[56] Wu, T. Y.-T., "Hydromechanics of swimming propulsion. Part 2. Some optimum shape problems," *Journal of Fluid Mechanics*, vol. 46, no. 3, pp. 521–544, 1971.

[57] Wu, T. Y.-T., "Hydromechanics of swimming propulsion. Part 3. Swimming and optimum movements of slender fish with side fins," *Journal of Fluid Mechanics*, vol. 46, no. 4, pp. 545–568, 1971.

[58] Taylor, G., "Analysis of the swimming of long and narrow animals," *Proceedings of the Royal Society of London A: Mathematical, Physical and Engineering Sciences*, vol. 214, no. 1117, pp. 158–183, 1952.

[59] Lighthill, M. J., "Note on the swimming of slender fish," *Journal of Fluid Mechanics*, vol. 9, no. 2, pp. 305–317, 1960.

[60] Lighthill, M. J., "Aquatic animal propulsion of high hydromechanical efficiency," *Journal of Fluid Mechanics*, vol. 44, no. 2, pp. 265–301, 1970.

[61] Lighthill, M. J., "Large-amplitude elongated-body theory of fish locomotion," *Proceedings of the Royal Society of London B: Biological Sciences*, vol. 179, no. 1055, pp. 125–138, 1971.

[62] Lighthill, M. J., "Hydromechanics of aquatic animal propulsion," *Annual Review of Fluid Mechanics*, vol. 1, no. 1, pp. 413–446, 1969.

[63] Candelier, F., Boyer, F., and Leroyer, A., "Three-dimensional extension of Lighthill's large-amplitude elongated-body theory of fish locomotion," *Journal of Fluid Mechanics*, vol. 674, pp. 196–226, 2011.

[64] Triantafyllou, M. S., Triantafyllou, G. S., and Yue, D. K. P., "Hydrodynamics of fishlike swimming," *Annual Review of Fluid Mechanics*, vol. 32, no. 1, pp. 33–53, 2000.

[65] Bandyopadhyay, P. R., "Swimming and flying in nature—The route toward applications: The Freeman Scholar Lecture," *Journal of Fluids Engineering*, vol. 131, no. 3, 031801, 2009.

[66] Wu, T. Y., "Fish swimming and bird/insect flight," *Annual Review of Fluid Mechanics*, vol. 43, pp. 25–58, 2011.

[67] Buchholz, J. H. J. and Smits, A. J., "The wake structure and thrust performance of a rigid low-aspect-ratio pitching panel," *Journal of Fluid Mechanics*, vol. 603, pp. 331–365, 2008.

[68] Buchholz, J. H. J. and Smits, A. J., "On the evolution of the wake structure produced by a low-aspect-ratio pitching panel," *Journal of Fluid Mechanics*, vol. 546, pp. 433–443, 2006.

[69] Facci, A. L. and Porfiri, M., "Nonlinear hydrodynamic damping of sharp-edged cantilevers in viscous fluids undergoing multi-harmonic base excitation," *Journal of Applied Physics*, vol. 112, no. 12, 124908, 2012.

[70] Facci, A. L. and Porfiri, M., "Analysis of three-dimensional effects in oscillating cantilevers immersed in viscous fluids," *Journal of Fluids and Structures*, vol. 38, pp. 205–222, 2013.

[71] Ramananarivo, S., Godoy-Diana, R., and Thiria, B., "Passive elastic mechanism to mimic fish-muscle action in anguilliform swimming," *Journal of The Royal Society Interface*, vol. 10, no. 88, 20130667, 2013.

[72] Alben, S., Witt, C., Baker, T. V., Anderson, E., and Lauder, G. V., "Dynamics of freely swimming flexible foils," *Physics of Fluids*, vol. 24, no. 5, 051901, 2012.

[73] Taylor, G. K., Nudds, R. L., and Thomas, A. L. R., "Flying and swimming animals cruise at a Strouhal number tuned for high power efficiency," *Nature*, vol. 425, no. 6959, pp. 707–711, 2003.

[74] Triantafyllou, M. S. and Triantafyllou, G. S., "An efficient swimming machine," *Scientific American*, vol. 272, no. 3, pp. 64–71, 1995.

[75] Triantafyllou, G. S., Triantafyllou, M. S., and Grosenbaugh, M. A., "Optimal thrust development in oscillating foils with application to fish propulsion," *Journal of Fluids and Structures*, vol. 7, no. 2, pp. 205–224, 1993.

[76] Anderson, J. M., Streitlien, K., Barrett, D. S., and Triantafyllou, M. S., "Oscillating foils of high propulsive efficiency," *Journal of Fluid Mechanics*, vol. 360, pp. 41–72, 1998.

[77] Dai, H., Luo, H., de Sousa, P. J. F., and Doyle, J. F., "Thrust performance of a flexible low-aspect-ratio pitching plate," *Physics of Fluids*, vol. 24, no. 10, 101903, 2012.

[78] Dewey, P. A., Boschitsch, B. M., Moored, K. W., Stone, H. A., and Smits, A. J., "Scaling laws for the thrust production of flexible pitching panels," *Journal of Fluid Mechanics*, vol. 732, pp. 29–46, 2013.

[79] Eloy, C., "Optimal Strouhal number for swimming animals," *Journal of Fluids and Structures*, vol. 30, pp. 205–218, 2012.

[80] Gazzola, M., Argentina, M., and Mahadevan, L., "Scaling macroscopic aquatic locomotion," *Nature Physics*, vol. 10, no. 10, pp. 758–761, 2014.

[81] Dewey, P. A., Carriou, A., and Smits, A. J., "On the relationship between efficiency and wake structure of a batoid-inspired oscillating fin," *Journal of Fluid Mechanics*, vol. 691, pp. 245–266, 2012.

[82] Moored, K. W., Dewey, P. A., Smits, A. J., and Haj-Hariri, H., "Hydrodynamic wake resonance as an underlying principle of efficient unsteady propulsion," *Journal of Fluid Mechanics*, vol. 708, pp. 329–348, 2012.

[83] Kang, C.-K., Aono, H., Cesnik, C. E. S., and Shyy, W., "Effects of flexibility on the aerodynamic performance of flapping wings," *Journal of Fluid Mechanics*, vol. 689, pp. 32–74, 2011.

[84] Masoud, H. and Alexeev, A., "Resonance of flexible flapping wings at low Reynolds number," *Physical Review E*, vol. 81, no. 5, 056304, 2010.

[85] Ramananarivo, S., Godoy-Diana, R., and Thiria, B., "Rather than resonance, flapping wing flyers may play on aerodynamics to improve performance," *Proceedings of the National Academy of Sciences*, vol. 108, no. 15, pp. 5964–5969, 2011.

[86] Vanella, M., Fitzgerald, T., Preidikman, S., Balaras, E., and Balachandran, B., "Influence of flexibility on the aerodynamic performance of a hovering wing," *Journal of Experimental Biology*, vol. 212, no. 1, pp. 95–105, 2009.

[87] Li, G.-Y., ZHU, L., and LU, X.-Y., "Numerical studies on locomotion perfromance of fish-like tail fins," *Journal of Hydrodynamics, Ser. B*, vol. 24, no. 4, pp. 488–495, 2012.

[88] Eloy, C., "On the best design for undulatory swimming," *Journal of Fluid Mechanics*, vol. 717, pp. 48–89, 2013.

[89] Tokić, G. and Yue, D. K. P., "Optimal shape and motion of undulatory swimming organisms," *Proceedings of the Royal Society of London B: Biological Sciences*, vol. 279, no. 1740, pp. 3065–3074, 2012.

[90] van Rees, W. M., Gazzola, M., and Koumoutsakos, P., "Optimal shapes for anguilliform swimmers at intermediate Reynolds numbers," *Journal of Fluid Mechanics*, vol. 722, R3, 2013.

[91] van Eysden, C. A. and Sader, J. E., "Frequency response of cantilever beams immersed in viscous fluids with applications to the atomic force microscope: Arbitrary mode order," *Journal of Applied Physics*, vol. 101, no. 4, 044908, 2007.

[92] Webb, P. W., "Simple physical principles and vertebrate aquatic locomotion," *American Zoologist*, vol. 28, no. 2, pp. 709–725, 1988.

[93] Ladd, A. J. C. and Verberg, R., "Lattice-Boltzmann simulations of particle-fluid suspensions," *Journal of Statistical Physics*, vol. 104, no. 5–6, pp. 1191–1251, 2001.

[94] Aidun, C. K., Lu, Y., and Ding, E.-J., "Direct analysis of particulate suspensions with inertia using the discrete Boltzmann equation," *Journal of Fluid Mechanics*, vol. 373, no. 1, pp. 287–311, 1998.

[95] Aidun, C. K. and Clausen, J. R., "Lattice-Boltzmann method for complex flows," *Annual Review of Fluid Mechanics*, vol. 42, pp. 439–472, 2010.

[96] Succi, S., *The lattice Boltzmann equation: For fluid dynamics and beyond*. Oxford University Press, 2001.

[97] Buxton, G. A., Care, C. M., and Cleaver, D. J., "A lattice spring model of heterogeneous materials with plasticity," *Modelling and Simulation in Materials Science and Engineering*, vol. 9, no. 6, pp. 485–497, 2001.

[98] Ostoja-Starzewski, M., "Lattice models in micromechanics," *Applied Mechanics Reviews*, vol. 55, no. 1, pp. 35–60, 2002.

[99] Monette, L. and Anderson, M. P., "Elastic and fracture properties of the two-dimensional triangular and square lattices," *Modelling and Simulation in Materials Science and Engineering*, vol. 2, no. 1, pp. 53–66, 1994.

[100] Alexeev, A., Verberg, R., and Balazs, A. C., "Modeling the motion of microcapsules on compliant polymeric surfaces," *Macromolecules*, vol. 38, no. 24, pp. 10244–10260, 2005.

[101] Mao, W., *Modeling particle suspensions using lattice Boltzmann method*. PhD thesis, Georgia Institute of Technology, 2013.

[102] Verlet, L., "Computer "experiments" on classical fluids. I. Thermodynamical properties of Lennard-Jones molecules," *Physical Review*, vol. 159, no. 1, pp. 98–103, 1967.

[103] Verlet, L., "Computer "experiments" on classical fluids. II. Equilibrium correlation functions," *Physical Review*, vol. 165, no. 1, pp. 201–214, 1968.

[104] Zhao, G.-F., Fang, J., and Zhao, J., "A 3D distinct lattice spring model for elasticity and dynamic failure," *International Journal for Numerical and Analytical Methods in Geomechanics*, vol. 35, no. 8, pp. 859–885, 2011.

[105] Chen, H., Filippova, O., Hoch, J., Molvig, K., Shock, R., Teixeira, C., and Zhang, R., "Grid refinement in lattice Boltzmann methods based on volumetric formulation," *Physica A: Statistical Mechanics and its Applications*, vol. 362, no. 1, pp. 158–167, 2006.

[106] Alexeev, A., Verberg, R., and Balazs, A. C., "Modeling the interactions between deformable capsules rolling on a compliant surface," *Soft Matter*, vol. 2, no. 6, pp. 499–509, 2006.

[107] Ballard, M., Mills, Z. G., Beckworth, S., and Alexeev, A., "Enhancing nanoparticle deposition using actuated synthetic cilia," *Microfluidics and Nanofluidics*, vol. 17, no. 2, pp. 317–324, 2014.

[108] Kilimnik, A., Mao, W., and Alexeev, A., "Inertial migration of deformable capsules in channel flow," *Physics of Fluids*, vol. 23, no. 12, 123302, 2011.

[109] Alexeev, A. and Balazs, A. C., "Designing smart systems to selectively entrap and burst microcapsules," *Soft Matter*, vol. 3, no. 12, pp. 1500–1505, 2007.

[110] Mills, Z. G., Aziz, B., and Alexeev, A., "Beating synthetic cilia enhance heat transport in microfluidic channels," *Soft Matter*, vol. 8, no. 45, pp. 11508–11513, 2012.

[111] Masoud, H., Bingham, B. I., and Alexeev, A., "Designing maneuverable micro-swimmers actuated by responsive gel," *Soft Matter*, vol. 8, no. 34, pp. 8944–8951, 2012.

[112] Arata, J. P. and Alexeev, A., "Designing microfluidic channel that separates elastic particles upon stiffness," *Soft Matter*, vol. 5, no. 14, pp. 2721–2724, 2009.

[113] Mao, W. and Alexeev, A., "Motion of spheroid particles in shear flow with inertia," *Journal of Fluid Mechanics*, vol. 749, pp. 145–166, 2014.

[114] Owen, D., Ballard, M., Alexeev, A., and Hesketh, P. J., "Rapid microfluidic mixing via rotating magnetic microbeads," *Sensors and Actuators A: Physical*, 2016.

[115] Ballard, M., Owen, D., Mills, Z. G., Hesketh, P. J., and Alexeev, A., "Orbiting magnetic microbeads enable rapid microfluidic mixing," *Microfluidics and Nanofluidics*, vol. 20, no. 6, pp. 1–13, 2016.

[116] Bouzidi, M., Firdaouss, M., and Lallemand, P., "Momentum transfer of a Boltzmann-lattice fluid with boundaries," *Physics of Fluids*, vol. 13, no. 11, pp. 3452–3459, 2001.

[117] Wang, Z. J., Birch, J. M., and Dickinson, M. H., "Unsteady forces and flows in low Reynolds number hovering flight: Two-dimensional computations vs robotic wing experiments," *Journal of Experimental Biology*, vol. 207, no. 3, pp. 449–460, 2004.

[118] Bisshopp, K. E. and Drucker, D. C., "Large deflection of cantilever beams," *Quarterly of Applied Mathematics*, vol. 3, no. 3, pp. 272–275, 1945.

[119] Kierzenka, J. and Shampine, L. F., "A BVP solver based on residual control and the Maltab PSE," *ACM Transactions on Mathematical Software*, vol. 27, no. 3, pp. 299–316, 2001.

[120] Ginsberg, J. H., *Mechanical and structural vibrations: Theory and applications*. John Wiley & Sons, 2001.

[121] Chatard, J. C., Lavoie, J. M., and Lacourl, J. R., "Analysis of determinants of swimming economy in front crawl," *European Journal of Applied Physiology and Occupational Physiology*, vol. 61, no. 1–2, pp. 88–92, 1990.

[122] Schmidt-Nielsen, K., "Locomotion: Energy cost of swimming, flying, and running," *Science*, vol. 177, no. 4045, pp. 222–228, 1972.

[123] Raspa, V., Ramananarivo, S., Thiria, B., and Godoy-Diana, R., "Vortex-induced drag and the role of aspect ratio in undulatory swimmers," *Physics of Fluids*, vol. 26, no. 4, 041701, 2014.

[124] Dong, H., Mittal, R., and Najjar, F. M., "Wake topology and hydrodynamic performance of low-aspect-ratio flapping foils," *Journal of Fluid Mechanics*, vol. 566, pp. 309–343, 2006.

[125] Alben, S., Madden, P. G., and Lauder, G. V., "The mechanics of active fin-shape control in ray-finned fishes," *Journal of The Royal Society Interface*, vol. 4, no. 13, pp. 243–256, 2007.

[126] Tangorra, J. L., Lauder, G. V., Hunter, I. W., Mittal, R., Madden, P. G. A., and Bozkurttas, M., "The effect of fin ray flexural rigidity on the propulsive forces generated by a biorobotic fish pectoral fin," *Journal of Experimental Biology*, vol. 213, no. 23, pp. 4043–4054, 2010.

[127] Wilkie, W. K., Bryant, R. G., High, J. W., Fox, R. L., Hellbaum, R. F., Jalink Jr, A., Little, B. D., and Mirick, P. H., "Low-cost piezocomposite actuator for structural control applications," in *Proceedings of SPIE 3991, Smart Structures and Materials 2000: Industrial and Commercial Applications of Smart Structures Technologies*, pp. 323–334, SPIE, 2000.

[128] High, J. W. and Wilkie, W. K., "Method of fabricating NASA-standard macro-fiber composite piezoelectric actuators," *NASA Technical Report*, 2003.

[129] Bryant, R. G., "Overview of NASA Langley's piezoelectric ceramic packaging technology and applications," *NASA Technical Report*, 2007.

[130] Cen, L. and Erturk, A., "Bio-inspired aquatic robotics by untethered piezohydroelastic actuation," *Bioinspiration & Biomimetics*, vol. 8, no. 1, 016006, 2013.

[131] Erturk, A. and Inman, D. J., "An experimentally validated bimorph cantilever model for piezoelectric energy harvesting from base excitations," *Smart Materials and Structures*, vol. 18, no. 2, 025009, 2009.

[132] Erturk, A. and Delporte, G., "Underwater thrust and power generation using flexible piezoelectric composites: An experimental investigation toward self-powered swimmer-sensor platforms," *Smart Materials and Structures*, vol. 20, no. 12, 125013, 2011.

[133] Weihs, D., "A hydrodynamical analysis of fish turning manoeuvres," *Proceedings of the Royal Society of London B: Biological Sciences*, vol. 182, no. 1066, pp. 59–72, 1972.

[134] Hu, H., Liu, J., Dukes, I., and Francis, G., "Design of 3D swim patterns for autonomous robotic fish," in *Proceedings of the 2006 IEEE/RSJ International Conference on Intelligent Robots and Systems*, pp. 2406–2411, IEEE, 2006.

[135] Su, Z., Yu, J., Tan, M., and Zhang, J., "Implementing flexible and fast turning maneuvers of a multijoint robotic fish," *IEEE/ASME Transactions on Mechatronics*, vol. 19, no. 1, pp. 329–338, 2014.

[136] Yu, J., Tan, M., Wang, S., and Chen, E., "Development of a biomimetic robotic fish and its control algorithm," *IEEE Transactions on Systems, Man, and Cybernetics, Part B (Cybernetics)*, vol. 34, no. 4, pp. 1798–1810, 2004.

[137] Liu, J. and Hu, H., "Mimicry of sharp turning behaviours in a robotic fish," in *Proceedings of the 2005 IEEE International Conference on Robotics and Automation*, pp. 3318–3323, IEEE, 2005.

[138] Tan, X., Carpenter, M., Thon, J., and Alequin-Ramos, F., "Analytical modeling and experimental studies of robotic fish turning," in *Proceedings of the 2010 IEEE International Conference on Robotics and Automation*, pp. 102–108, IEEE, 2010.

[139] Meirovitch, L., *Fundamentals of vibrations*. Waveland Press, 2010.

[140] Mabie, H. H. and Rogers, C. B., "Transverse vibrations of tapered cantilever beams with end support," *The Journal of the Acoustical Society of America*, vol. 44, no. 6, pp. 1739–1741, 1968.

VITA

Peter Derek Yeh was born and raised in Monmouth County, New Jersey. He received his B.S. in Engineering Physics with a minor in Mechanical Engineering from Cornell University in 2011, and then received his M.S. in Mechanical Engineering in 2013 from Georgia Tech, where he continued with his Ph.D. studies. Peter has worked with the Complex Fluids Modeling and Simulation Group under the direction of Dr. Alexander Alexeev since 2011, and also has worked with Sandia National Laboratories as a graduate intern since 2015. Peter's research interests are in all aspects of computational mechanics from numerical algorithms, software development, and data analysis to study interdisciplinary problems in engineering and physics.